THE INFLUENCE OF URBAN HEAT ISLAND EFFECT AND ITS RELATIONSHIP WITH LAND COVER, SCALE, AND SEASONALITY IN A LOW-DENSITY URBAN CENTER

by

Michael Burnett

A thesis submitted to the Department of Geography and Planning

In conformity with the requirements for

the degree of Master of Science

Queen's University

Kingston, Ontario, Canada

(May, 2021)

Abstract

Land surface temperature (LST) and air temperature (T_{air}) are the primary metrics applied to measure and analyze urban heat island (UHI) effects, a thermal phenomenon caused by urbanization. This thesis aims to study the UHI effect of a rapidly expanding low-density urban center using two satellite based LST products. Milton, Ontario, Canada was selected as the study site due to its rapid urban development from 2000 to 2019. Two LST products extracted from Landsat 7 Enhanced Thematic Mapper (ETM+) through Google Earth Engine at 30 m resolution and Moderate Resolution Imaging Spectroradiometer (MODIS) at 1 km resolution were compared. The influence of the spatial resolution, land cover, vegetated surfaces and seasonality on the relationship between LST and in situ T_{air} were examined. UHI footprint (UHIFP) and the surface UHI (SUHI) models were compared to measure the local UHI impact on rural vegetation based on the time series LST data from Landsat 7. The UHI impact on surrounding land in the suburban and rural environment from 2000 to 2019 was analyzed.

Results show that MODIS LST from Terra had stronger relationships with Landsat 7 LST than those from Aqua. T_{air} demonstrated weaker correlations with Landsat LST than with MODIS LST in sparsely vegetated and urban areas during the summer. Due to the winter's ability to smooth heterogenous surfaces, both LST and T_{air} showed stronger relationships in winter than summer over every land cover, except with coarse spatial resolutions on forested surfaces. The UHI footprint of the studied low-density suburban center is about 1.4 times larger than the urban center. All vegetated land covers experienced their maximum cooling effects well before reaching the UHIFP perimeter while urban surfaces only begin to diverge from the SUHI Gaussian model outside of the UHIFP. The similar results from both methods indicate a strong urban cover influence overpowering the dominantly distributed agricultural surfaces throughout the growing season. Moisture index was shown as the dominant variable, above vegetation health, correlating with the UHI residuals within every land cover throughout the growing season. This research has helped us better understand the UHI effects of small communities with varied vegetation

phonology based on the distribution of built-up pervious and impervious surfaces within the neighborhood structure.

Co-Authorship

Chapter 2 “The Impact of Seasonality and Land Cover Distribution on the Consistency of LST Derived from Landsat 7 and MODIS at a Local Scale : A Case Study in Southern Ontario” is co-authored by M. Burnett and D. Chen.

Chapter 3 “Surface Urban Heat Island Footprint Effects on Bio-Productive Rural Land Covers Surrounding a Low Density Urban Center” is co-authored by M. Burnett and D. Chen.

I am the primary author responsible for the analysis and writing of all manuscripts, data analysis, and figure creation. D. Chen provided comments and feedback for all chapters and offered guidance throughout the process of analysis and writing.

Acknowledgements

I would like to thank my supervisor, Dr. Dongmei Chen, for all of the support and guidance throughout my research and writing stages. I have learned a lot in my two years here at Queens University, and much of it is due to the assistance you have provided me with. I would also like to thank everyone in the LAGISA lab for all the help and direction you have provided me with.

I am also grateful for Dr. Stefania Bonafoni and Roberta Anniballe's contribution of the MATLAB script for determining the SUHI Gaussian planar fit model based on their previous research. Their script was instrumental with my research presented in Chapter 3.

This research was supported by a National Science and Engineering Research Council (NSERC) Discovery Grant and Queen's Graduate Scholarship.

Table of Contents

List of Figures

List of Tables

List of Abbreviations

ASTER	Advanced Spaceborne Thermal Emission and Reflection Radiometer Global Emissivity Data Set
AVHRR	Advanced Very High Resolution Radiometer
C	Celsius
CBD	Central Business District
ETM+	Enhanced Thematic Mapper
EVI	Enhanced Vegetation Index
GIS	Geographic Information System
K	Kelvin
km	Kilometer
LST	Land Surface Temperature
m	Meter
MODIS	Moderate Resolution Imaging Spectroradiometer
NDMI	Normalized Difference Moisture Index
NDVI	Normalized Difference Vegetation Index
NIR	Near Infrared
RMSE	Root Mean Square Error
SE	Surface Emissivity
SLC	Scan Line Corrector
SMW	Statistical Mono-Window
SOLRIS	Southern Ontario Land Resource Information System
SR	Surface Reflectance
SUHI	Surface Urban Heat Island

SWA	Split-Window Algorithm
T_{air}	Air Temperature
TIR	Thermal Infrared
UHI	Urban Heat Island
UHIFP	Urban Heat Island Footprint

Chapter 1

Introduction and Literature Review

This chapter provides context for the research presented and amalgamated in Chapters 2 and 3 of this thesis. The central focus of this research is to understand the relationship between land surface temperature (LST) and different bio-productive land covers in a rapidly urbanizing Canadian environment. LST data plays an important role in examining urban heat islands (UHI) around the world. Its relationship with air temperature (T_{air}) relative to local land covers helps determine the temperature variability depending on surface characteristics, especially in an urban environment. Heat absorption from different types of urban surfaces, along with anthropogenic activities from urbanization, contribute to UHI effects from rising LST and T_{air}.

This introduction and literature review examines the global development of urban expansion with emphasis on the Canadian domain. Next, the concept of UHI is examined. The applications and progress accomplished with LST through remote sensing are also discussed. Finally, the local study site is introduced.

1.1 Urban Development

Throughout the 20th Century, a global transition occurred from prominently agrarian nations to urban dwellers. By 1900, around 13% of the Earth's population resided in urban places of 5,000 people or more; an urban size which in 2007, over half the world's population would call home (Brunn et al., 2020). This rapid migration has introduced a plethora of land use/land cover patterns along with new human and environmental challenges to overcome.

Urban forms and patterns have evolved based on purpose and technology. Urban spatial processes were originally developed following an agricultural surplus based on concentration of power and decision making, flow and location of economic activities, diffusion of innovation, and migration (King & Golledge, 1978). Their locations would be advantageous based on the

surrounding topography and proximity to valuable resources. As population accumulated and technological innovations developed, a city's urban land-use patterns changed with the needs of the time. Commercial activities were arranged in a centralized hierarchy with the Central Business District (CBD) at the apex. Industrial space became increasingly decentralized with transportation innovations and environmental considerations (King & Golledge, 1978). Residential remained the largest occupier of space with preference for low-density. Alternatively, conditions with high-density urban life often manifested in mental, physical, and social pathologies resulting in varied levels of sensory overload and social disorganization based on culture (Porteous, 1977).

Due to the complexities of designing urban structures for optimal living spaces, three generalized patterns of land uses were naturally produced. The concentric zone hypothesis places the CBD (where major commercial, political, and social activities are centered in its highest forms of density) as the core with further decentralized residential on the outside (King & Golledge, 1978). The wedge and sector hypothesis determines residential patterns based on physical features such as rivers, lakes, railways, and major highways (King & Golledge, 1978). Finally, the multiple nuclei pattern applies both ideas and dictates land-use patterns around several centers (King & Golledge, 1978). Examples of each form are present around the world, especially within Canada where all three may be exhibited within one region.

The perseverance of small cities is complex as their role is either diminishing or changing. In the latter half of the 20th Century, there was concern about the continuing viability of small urban places as efficient transportation networks improve travel times to larger urban centers and only "convenient" shopping needs are met in smaller towns (King & Golledge, 1978). Although those concerns have not disappeared and the state of small communities is in constant flux, urban centers of a similar size adjacent to major cities, known as suburbs, have become the desired location for present migration. With a large portion of the increasing human population

housed within suburbs, they exist within the background of large cities around the world as newer and low-density communities (Forsyth, 2014). Despite their individual importance in the structure and distribution of a local population, suburbs are often excluded from urban analyses or incorporated with the major metropolitan CBD.

The environmental consequences to all forms of urbanization and anthropogenic activities have become an increasingly prevalent concern around the world. These include disturbances to vegetation (such as deforestation), fauna (expansion and retraction of animal populations), soil (such as salinity or erosion), waters (such as river flow and pollution), geomorphology (such as landforms produced from excavation or construction), and atmosphere (Goudie, 1994). A major subject matter throughout this thesis is centered around the urban heat island (UHI) effect, which is a cause of many disturbances. It will be discussed more extensively in Section 1.2; however, it is important to recognize that it is not the sole consequential product of urbanization.

1.1.1 Urban Development within Canada

Over the past several decades, the urban form of Canadian cities has dramatically changed its character away from the concentric model designed around an urban core. This has resulted in the decentralization of population and employment from monocentric cities with highly important CBD to a suburban polycentric model with automobile dependency and continuous infrastructure project investments (H. Maoh & Kanaroglou, 2007). The new multinucleated urban form presents population and employment patterns distributed to a variety of foci (Cuthbert & Anderson, 2002). Additionally, the increased necessity for urban design structured on automobile dependence has changed the attitudes of the population and land use planning design to accommodate for urban sprawl. People desire housing situated further from the CBD to enjoy increasingly spacious private residences with reasonable commuting distances (Ash, 2017). The consequence to such changing attitudes is a population's rapid horizontal expansion in the form of low-density

developments as distance increases from the CBD (H. F. Maoh et al., 2010). Outer-city urbanization often takes three main forms abundantly used throughout North America: satellite cities, suburban towns, and exurban communities.

There is often disagreement regarding its definition; however, a general consensus states that satellite cities are independent political jurisdictions with civic and industrial autonomy outside of the major city (Goldfield, 2007). These cities thrive with its own supply of job opportunities and public facilities by retaining a distance from the major city while remaining closely related in terms of administration, economy, culture, and life (Shao, 2015). This contrasts the conventional approach to describing suburban communities with their reliance upon major cities.

The term ‘suburban’ can hold a variety of implications depending upon the country in which it is being used. Prior to the second world war, suburbs were communities where the metropolitan elite could escape the congestion, stress, and epidemics of the metropolis through rail and streetcar connections to middle class homes with grand villas, gardens, and horses (Hanson, 2017). Rapid suburban expansion soon became possible with the increasing demand for housing, reductions in construction costs, government building programs, mass production of automobiles, and greater emphasis on low-density single-family housing architecture (Caves, 2005). The main separation they have with satellite cities relates to their reliance on the central metropolis for employment, entertainment, specialized retail, and commercial services (Goldfield, 2007). Local commercial and industrial activity continues to exist; however, these communities would fail to thrive in the absence of the main urban center.

The differentiation between the major metropolitan cities, satellite cities, and suburbs is paramount in dissecting the residential distribution throughout Canada. Gordon & Janzen (2013) described how 80% of Canada’s metropolitan population (and 66% of all of Canada’s population) are suburban residents (his suburban demographics is inclusive of satellite city residents). As a

result, understanding the environmental impact of suburban development is necessary as it represents where the majority of Canadian urban expansion occurs.

A third suburban category is described as an alternative classification to the use of the word “rural”, which is often associated with agricultural practices. Exurban refers to any census tract with a very low gross population density and heavy reliance upon automobiles where over half of the labour force commutes to central cities for employment (Gordon & Janzen, 2013; Gordon et al., 2018). This thesis will use the term ‘rural’ in continuity with previous research on UHI while the area is actually exurban in function.

1.2 Urban Heat Island

The well-studied consequence of urbanization, the urban heat island (UHI) effect, was initially discovered by Luke Howard while studying meteorological patterns in London, UK (Howard, 1818). Despite limited resources and methodology, Howard was capable of accurately describing the UHI through four main discoveries which continue to be applicable today.

First, he discovered through the available records in London that the denser parts of the metropolis experience warmer temperature, especially during the winter, when compared to the less dense suburban areas (Mills, 2008). Population density and urban patterns have proven to have instrumental roles in regards to temperature variation. Ramírez-Aguilar & Lucas Souza (2019) reported that population densities above 14,500 inhabitants/km2 have potential for causing air temperature variations greater than 1˚C, increased obstructions in the sky, and reduced vegetation phenology. As a result, the urban form and population density can dictate the magnitude of a local UHI.

Howard also discovered the effects that the urban canopy layer has upon local temperature. He noted an increasing UHI trend towards the core of a settlement where building density is maximized, pockets of cooler air are localized, and the natural features remain, such as lakes, rivers, and parks (Mills, 2008). As an example, being one of the most densely populated

cities in the world, Hong Kong experiences some of the most dramatic UHI effects globally. Its compact highly urbanized form results in temperature changes as high as 4˚C (Tan et al., 2016). The locality of urban parks and natural features within the metropolis delivers relief from UHI effects. A study in Hong Kong (Lin et al., 2017) identified 10 pocket parks (urban green spaces surrounded by high-rise buildings/high density built up areas) which help alleviate UHI intensity at a micro scale during day and night. These reports indicate significant cooling properties within an otherwise highly urban area. The understanding of varied temperatures throughout urban centers is fundamental in determining why and how it differs from lower density and rural land covers outside of the metropolis.

Anthropogenic gases have also long been identified as being a contributor to UHI. Howard noticed how the heat produced from our bodies, animals, and industries plays a major role in creating warmer environments in an urban setting which was even more noticeable in the winter due to chimney exhaust from residential heating (Mills, 2008). Since Howard's death, anthropogenic pollution in the form of greenhouse gases have become a dominant factor affecting the radiation budget within urban centers. Increasing quantities of aerosols exhausted into the atmosphere results in scattering incoming solar radiation, a reduction of radiation absorbed and reflected on the surface, and the atmospheric absorption of emitted longwave radiation from the surface (Li et al., 2018). The absorbed atmospheric infrared radiation can then be emitted back to the surface, thus increasing heat stored in urban environments. In effect, increased concentrations of pollution impacts the UHI intensity.

The detection of moisture for evaporation was the fourth main discovery Howard found. The vertical structures in London reflects and acquires solar radiation and then impedes the passage of light summer winds, allowing for faster evaporation compared to its countryside counterpart (Mills, 2008). Water bodies have the advantage in reducing UHI impacts. With ventilation services available, in conjunction with shortwave solar radiation, water has a

prominent cooling ability in its evaporation (Xu et al., 2019). Compared with impervious surfaces, the thermal capacity of water is much slower at contributing to rising temperature levels (Yu et al., 2020). The effects of UHI can be reduced when properly incorporating water bodies and vegetated spaces within larger metropolises.

1.3 Land Surface Temperature, Remote Sensing, and Urban Heat Island (UHI) Effect

New methods to calculate UHI effects have evolved from studying the relationship between urban environments and temperature. Oke (1973) introduced methods of modelling the difference between background rural and the highest urban temperatures with city size (as measured by population). In situ LST and T_{air} stations measuring the seasonal UHI effects for a variety of cities were implemented to study variations caused by natural and anthropogenic forces (Dettwiller, 1970; Katsoulis & Theoharatos, 1985). Technological advancements with satellite data allowed for a more widespread global exploration of its effects with a variety of scales and methods for assessment.

The acquisition of LST is distinctively different from near surface T_{air} based on methods of measurement and the variables in effect. T_{air} is measured at elevated platforms with ventilated sensors offering protection from solar radiation (Mildrexler et al., 2011). Vegetation distribution, canopy coverage, wind, humidity, and additional atmospheric properties surrounding each climate station present variables which can greatly affect the local T_{air} (Stewart & Oke, 2012). LST, alternatively, differs from T_{air} due to its physical meaning, magnitude, and measurement techniques through its estimation of thermal radiance from the surface (Mildrexler et al., 2011). Despite their differences, T_{air} can be successfully estimated through interpolation using LST data (Kloog et al., 2014) and estimated with greater degrees of success with snow coverage (Shamir & Georgakakos, 2014). Both metrics represent temperatures involving differing properties and variables which influence the atmospheric environment they involve.

Satellite derived LST is dependent upon thermal infrared (TIR) imagery acquired from different sensors. Derived from thermal, radiance, and moisture properties, LST is an important variable for modeling energy fluxes on the surface environment, the retrieval of spatially continuous air temperature, and the quantification of the surface UHI effect (Fu & Weng, 2016). Its data is derived from sensible and latent heat with emphasis on albedo, evapotranspiration, and surface roughness influences among other factors (He et al., 2018). It's application with Geographical Information Systems (GIS) provides global coverage and scope, varied levels of resolution, plethora of selectable options, and accessibility to data that would otherwise be unattainable (Tomlinson et al., 2011). With its availability, the assessment of its relationship with land covers at different scales and UHI impacts is feasible.

Following the introduction of high-resolution monitoring satellites, it is now possible to perform remote UHI analyses with any global location. The earliest examples of understanding the scientific processes using remote sensing technology dates back to the 1970s (Matson et al., 1978; Price, 1979); however, the techniques employed were primitive compared to modern developments. Gallo et al. (1993) first discovered a positive correlation between the normalized difference vegetation index (NDVI) and both LST and T_{air} in urban and rural environments using imagery acquired from the NOAA Advanced Very High Resolution Radiometer (AVHRR). The adoption of satellite-derived data accelerated the advancements made studying UHI. A two-dimensional Gaussian surface modelling the UHI effects of the urban-rural differences introduced methods of displaying the distribution and quantification of the spatial breadth of the UHI (D. R. Streutker, 2002; David R Streutker, 2003). The planar fit model, known as the surface UHI (SUHI) model, has since become widely used to study the magnitude, orientation, spatial extent, and temporal change.

In the past two decades, a plethora of advancements have been made for analyzing and understanding the UHI effects with a variety of variables and methods. With the majority of the

research focusing on its effects within the urban environment (Oke, 1973; Rajasekar & Weng, 2009; Santamouris et al., 2007; David R Streutker, 2003), gaps have remained with studies focused on the rural surface effects from the UHI footprint. Research on the consequences to vegetation phenology using satellite imagery began with focus on its influence on the growing season (White et al., 2002) and the phenological responses to spatial variability (Zhang et al., 2004). Zhou et al. (2015) expanded on the methodology and applied it to estimate the spatiotemporal variability of the UHI footprint along urban-rural gradients. Studies have expanded upon the impact on vegetation phenology based on proximity (Krehbiel et al., 2016; Qiao et al., 2019), comparisons with various vegetation indices (Krehbiel et al., 2016; Yao, Wang, Gui, et al., 2017; Yao, Wang, Huang, et al., 2017), and the change caused to background, or rural, temperatures (Shi et al., 2019; Yao, Wang, Huang, et al., 2017). With the continuous focus on large metropolitan urban centers, there exists gaps concerning implications with a small, localized, suburban center and the role each bio-productive surface has with its UHI.

1.4 Selection of Study Site

The process to determine an appropriate study site relies upon the selection of a municipality that is representative of Canadian urban expansion and addresses gaps in existing research. Considering how most UHI related research is focused upon large urban metropolises (Anniballe & Bonafoni, 2015; Huang et al., 2019; Martin et al., 2015; Meng & Liu, 2013; Qiao et al., 2019; D. R. Streutker, 2002; David R Streutker, 2003; Zhou et al., 2015), the selection of an urban center on the periphery of a major city is helpful in addressing the research gaps on the effects from a local suburban town's UHI. Since the majority of the Canadian metropolitan population resides within low-density residential neighborhoods (H. Maoh & Kanaroglou, 2007), it is important to research the UHI effects from smaller developing communities for comparison purposes. This research will be helpful for developing effective planning techniques since expansion will continue to increase in these types of urban centers.

The selected location for this research is Milton, in the province of Ontario. This town is amongst the most rapidly urbanizing communities nationwide. With a population increase of 30.5% between 2011 and 2016 to 110,128 people, Milton is the fastest-growing community in Ontario, and the sixth overall throughout Canada (Hennessey, 2017). It is the only town within the list developed by Naraghi (2019) describing the "fastest-growing communities in Canada" with a population in excess of 100,000. Its local CBD has been marked to achieve a population and employment density of 200 per hectare by 2031 (Government of Ontario, 2017). It poses a unique opportunity to explore a significantly large site experiencing rapid low-density urban expansion throughout the first two decades of the 21st Century. This establishes it as an ideal choice due to its size being small enough to be 'suburban' and large enough to present serious environmental impacts upon its surrounding rural environment.

1.5 Research Objectives

The research presented in this thesis aims to address gaps in the scientific literature concerning UHI and how it has affected LST within and near urban environments. Specifically, this research aims to determine the role it plays with T_{air} and under the influence of the UHI effect of a low-density Canadian suburban center with different categories of bio-productive land covers. More specifically, the following questions are addressed in order to achieve the research objective :

1) What is the difference between LST data derived from MODIS at 1 km resolution and Landsat 7 ETM+ at 30 m resolution?

2) How does the seasonality, land cover, and spatial resolution impact the relationship between satellite-derived LST and T_{air}?

3) What is the extent of thermal disturbance of UHI on the LST of each bio-productive surface in the spatially proximate rural areas and how does it change from 2000 to 2019?

4) How consistent are the methods for determining the spatial footprint of the UHI effect?

5) What are the factors influencing the spatiotemporal pattern that low-density anthropogenic urban activities have upon each land cover with varying degrees of distance from the urban center perimeter?

This thesis consists of two manuscripts, Chapter 2, which addresses the first two questions listed, and Chapter 3, which addresses the last three questions. Chapter 2 compares surface and near-surface temperatures acquired at different scales based on land cover distributions and seasonality. Chapter 3 examines the footprint of a suburban UHI and the variables influencing it. Chapter 4 summarizes the findings that have emerged from this research and makes recommendations for future research. The manuscripts help explain how the relationship LST has with bio-productive land covers differs based on scale, its variability with T_{air}, and its spatiotemporal pattern influenced from an expanding suburban UHI.

1.6 References

Anniballe, R., & Bonafoni, S. (2015). A Stable Gaussian Fitting Procedure for the Parameterization of Remote Sensed Thermal Images. Algorithms, 8(2), 82–91. https://doi.org/10.3390/a8020082

Ash, L. J. (2017). Excess Commuting and its Relation to Urban Form in Ontario, Canada [M.A.Sc., University of Windsor (Canada)]. http://search.proquest.com/docview/1987971961/abstract/52ED7E29DA704490PQ/1

Brunn, S. D., Zeigler, D. J., Hays-Mitchell, M., & Graybill, J. K. (Eds.). (2020). Cities of the World: Regional Patterns and Urban Environments (7th ed.). Rowman & Littlefield Publishers.

Caves, R. W. (2005). Encyclopedia of the City. Taylor & Francis Group. http://ebookcentral.proquest.com/lib/queen-ebooks/detail.action?docID=182222

Cuthbert, A. L., & Anderson, W. P. (2002). Using Spatial Statistics to Examine the Pattern of Urban Land Development in Halifax–Dartmouth. The Professional Geographer, 54(4), 521–532. https://doi.org/10.1111/0033-0124.00347

Dettwiller, J. (1970). Deep Soil Temperature Trends and Urban Effects at Paris. Journal of Applied Meteorology (1962-1982), 9(1), 178–180.

Forsyth, A. (2014). Global suburbia and the transition century: Physical suburbs in the long term. URBAN DESIGN International, 19(4), 259–273. https://doi.org/10.1057/udi.2013.23

Fu, P., & Weng, Q. (2016). Consistent land surface temperature data generation from irregularly spaced Landsat imagery. Remote Sensing of Environment, 184, 175–187. https://doi.org/10.1016/j.rse.2016.06.019

Gallo, K. P., McNab, A. L., Karl, T. R., Brown, J. F., Hood, J. J., & Tarpley, J. D. (1993). The Use of NOAA AVHRR Data for Assessment of the Urban Heat Island Effect. Journal of Applied Meteorology and Climatology, 32(5), 899–908. https://doi.org/10.1175/1520-0450(1993)032<0899:TUONAD>2.0.CO;2

Goldfield, D. (2007). Encyclopedia of American Urban History. SAGE. https://books.google.ca/books?id=yWA5DQAAQBAJ&pg=PT815&redir_esc=y#v=onepage&q&f=false

Gordon, D. L. A., Hindrichs, L., & Willms, C. (2018). Still Suburban? Growth in Canadian Suburbs, 2006-2016 (Working Paper #2; p. 91). Queen's University. http://www.canadiansuburbs.ca/files/Still_Suburban_Monograph_2016.pdf

Gordon, D. L. A., & Janzen, M. (2013). Suburban Nation? Estimating the size of Canada's Suburban Population. Journal of Architectural and Planning Research, 30(3), pp. 197-220.

Goudie, A. (1994). The Human Impact on the Natural Environment (4th ed.). The MIT Press, pp. 315-337.

Government of Ontario. (2017). Growth Plan for the Greater Golden Horseshoe. Queen's Printer for Ontario. https://www.halton.ca/Repository/Growth-Plan-for-the-Greater-Golden-Horseshoe,-2017

Hanson, R. (2017). Suburb. Cornell University Press, pp. 7-20.

He, G., Zhao, Y., Wang, J., Wang, Q., & Zhu, Y. (2018). Impact of large-scale vegetation restoration project on summer land surface temperature on the Loess Plateau, China. Journal of Arid Land, 10(6), 892–904. https://doi.org/10.1007/s40333-018-0105-z

Hennessey, M. (2017, February 8). Census: Milton remains in top 10 fastest-growing Canadian communities. Inside Halton. https://www.insidehalton.com/news-story/7110264-census-milton-remains-in-top-10-fastest-growing-canadian-communities/

Howard, L. (1818). The Climate of London: Deduced from Meteorological Observations, Made at Different Places in the Neighbourhood of the Metropolis. W. Phillips, George Yard, Lombard Street, sold also by J. and A. Arch, Cornhill; Baldwin, Cradock, and Joy, and W. Bent, Paternoster Row; and J. Hatchard, Picadilly.

Huang, Q., Huang, J., Yang, X., Fang, C., & Liang, Y. (2019). Quantifying the seasonal contribution of coupling urban land use types on Urban Heat Island using Land Contribution Index: A case study in Wuhan, China. Sustainable Cities and Society, 44, 666–675. https://doi.org/10.1016/j.scs.2018.10.016

Katsoulis, B. D., & Theoharatos, G. A. (1985). Indications of the Urban Heat Island in Athens, Greece. Journal of Climate and Applied Meteorology, 24(12), 1296–1302.

King, L. J., & Golledge, R. G. (1978). Cities, Space, and Behavior: The Elements of Urban Geography. Prentice-Hall, Inc., (pp. 14-52, 181-211, 257-277).

Kloog, I., Nordio, F., Coull, B. A., & Schwartz, J. (2014). Predicting spatiotemporal mean air temperature using MODIS satellite surface temperature measurements across the Northeastern USA. Remote Sensing of Environment, 150, 132–139. https://doi.org/10.1016/j.rse.2014.04.024

Krehbiel, C. P., Jackson, T., & Henebry, G. M. (2016). Web-Enabled Landsat Data Time Series for Monitoring Urban Heat Island Impacts on Land Surface Phenology. IEEE Journal of Selected Topics in Applied Earth Observations and Remote Sensing, 9(5), 2043–2050. https://doi.org/10.1109/JSTARS.2015.2496951

Li, H., Meier, F., Lee, X., Chakraborty, T., Liu, J., Schaap, M., & Sodoudi, S. (2018). Interaction between urban heat island and urban pollution island during summer in Berlin. Science of The Total Environment, 636, 818–828. https://doi.org/10.1016/j.scitotenv.2018.04.254

Lin, P., Siu, S., Qin, H., & Gou, Z. (2017). Effects of urban planning indicators on urban heat island: A case study of pocket parks in high-rise high-density environment. Landscape and Urban Planning, 168, 48–60. https://doi.org/10.1016/j.landurbplan.2017.09.024

Maoh, H. F., Koronios, M., & Kanaroglou, P. S. (2010). Exploring the land development process and its impact on urban form in Hamilton, Ontario. The Canadian Geographer / Le Géographe Canadien, 54(1), 68–86. https://doi.org/10.1111/j.1541-0064.2009.00303.x

Maoh, H., & Kanaroglou, P. (2007). Geographic clustering of firms and urban form: A multivariate analysis. Journal of Geographical Systems, 9(1), 29–52. http://dx.doi.org.proxy.queensu.ca/10.1007/s10109-006-0029-6

Martin, P., Baudouin, Y., & Gachon, P. (2015). An alternative method to characterize the surface urban heat island. International Journal of Biometeorology, 59(7), 849–861. https://doi.org/10.1007/s00484-014-0902-9

Matson, M., Mcclain, E. P., McGinnis, D. F., & Pritchard, J. A. (1978). Satellite Detection of Urban Heat Islands. Monthly Weather Review, 106(12), 1725–1734. https://doi.org/10.1175/1520-0493(1978)106<1725:SDOUHI>2.0.CO;2

Meng, F., & Liu, M. (2013). Remote-sensing image-based analysis of the patterns of urban heat islands in rapidly urbanizing Jinan, China. International Journal of Remote Sensing, 34(24), 8838–8853. https://doi.org/10.1080/01431161.2013.853895

Mildrexler, D. J., Zhao, M., & Running, S. W. (2011). A global comparison between station air temperatures and MODIS land surface temperatures reveals the cooling role of forests. Journal of Geophysical Research: Biogeosciences, 116(G3). https://doi.org/10.1029/2010JG001486

Mills, G. (2008). Luke Howard and The Climate of London. Weather, 63(6), 153–157. https://doi.org/10.1002/wea.195

Naraghi, A. (2019, August 8). Fastest-growing communities in Canada 2019. Maclean's. https://www.macleans.ca/economy/fastest-growing-communities-in-canada-2019/

Oke, T. R. (1973). City size and the urban heat island. Atmospheric Environment (1967), 7(8), 769–779. https://doi.org/10.1016/0004-6981(73)90140-6

Porteous, J. D. (1977). Environment & Behavior: Planning and Everyday Urban Life. Addison-Wesley Publishing Company, Inc., pp. 149-179.

Price, J. C. (1979). Assessment of the Urban Heat Island Effect Through the Use of Satellite Data. Monthly Weather Review, 107(11), 1554–1557. https://doi.org/10.1175/1520-0493(1979)107<1554:AOTUHI>2.0.CO;2

Qiao, Z., Wu, C., Zhao, D., Xu, X., Yang, J., Feng, L., Sun, Z., & Liu, L. (2019). Determining the Boundary and Probability of Surface Urban Heat Island Footprint Based on a Logistic Model. Remote Sensing, 11(11), 1368. https://doi.org/10.3390/rs11111368

Rajasekar, U., & Weng, Q. (2009). Spatio-temporal modelling and analysis of urban heat islands by using Landsat TM and ETM+ imagery. International Journal of Remote Sensing, 30(13), 3531–3548. https://doi.org/10.1080/01431160802562289

Ramírez-Aguilar, E. A., & Lucas Souza, L. C. (2019). Urban form and population density: Influences on Urban Heat Island intensities in Bogotá, Colombia. Urban Climate, 29, 100497. https://doi.org/10.1016/j.uclim.2019.100497

Santamouris, M., Paraponiaris, K., & Mihalakakou, G. (2007). Estimating the ecological footprint of the heat island effect over Athens, Greece. Climatic Change, 80(3), 265–276. https://doi.org/10.1007/s10584-006-9128-0

Shamir, E., & Georgakakos, K. P. (2014). MODIS Land Surface Temperature as an index of surface air temperature for operational snowpack estimation. Remote Sensing of Environment, 152, 83–98. https://doi.org/10.1016/j.rse.2014.06.001

Shao, Z. (2015). The New Urban Area Development: A Case Study in China. Springer. https://books.google.ca/books?id=eq1nCgAAQBAJ&pg=PA25&redir_esc=y#v=onepage&q&f=false

Shi, Z., Jia, G., Hu, Y., & Zhou, Y. (2019). The contribution of intensified urbanization effects on surface warming trends in China. Theoretical and Applied Climatology, 138(1–2), 1125–1138. https://doi.org/10.1007/s00704-019-02892-y

Stewart, I. D., & Oke, T. R. (2012). Local Climate Zones for Urban Temperature Studies. Bulletin of the American Meteorological Society, 93(12), 1879–1900. https://doi.org/10.1175/BAMS-D-11-00019.1

Streutker, D. R. (2002). A remote sensing study of the urban heat island of Houston, Texas. International Journal of Remote Sensing, 23(13), 2595–2608. https://doi.org/10.1080/01431160110115023

Streutker, David R. (2003). Satellite-measured growth of the urban heat island of Houston, Texas. Remote Sensing of Environment, 85(3), 282–289. https://doi.org/10.1016/S0034-4257(03)00007-5

Tan, Z., Lau, K. K.-L., & Ng, E. (2016). Urban tree design approaches for mitigating daytime urban heat island effects in a high-density urban environment. Energy and Buildings, 114, 265–274. https://doi.org/10.1016/j.enbuild.2015.06.031

Tomlinson, C. J., Chapman, L., Thornes, J. E., & Baker, C. (2011). Remote sensing land surface temperature for meteorology and climatology: A review. Meteorological Applications, 18(3), 296–306. https://doi.org/10.1002/met.287

White, M. A., Nemani, R. R., Thornton, P. E., & Running, S. W. (2002). Satellite Evidence of Phenological Differences Between Urbanized and Rural Areas of the Eastern United States Deciduous Broadleaf Forest. Ecosystems, 5(3), 260–273. https://doi.org/10.1007/s10021-001-0070-8

Xu, X., Liu, S., Sun, S., Zhang, W., Liu, Y., Lao, Z., Guo, G., Smith, K., Cui, Y., Liu, W., Higueras García, E., & Zhu, J. (2019). Evaluation of energy saving potential of an urban green space and its water bodies. Energy and Buildings, 188–189, 58–70. https://doi.org/10.1016/j.enbuild.2019.02.003

Yao, R., Wang, L., Gui, X., Zheng, Y., Zhang, H., & Huang, X. (2017). Urbanization Effects on Vegetation and Surface Urban Heat Islands in China's Yangtze River Basin. Remote Sensing, 9(6), 540. https://doi.org/10.3390/rs9060540

Yao, R., Wang, L., Huang, X., Guo, X., Niu, Z., & Liu, H. (2017). Investigation of Urbanization Effects on Land Surface Phenology in Northeast China during 2001–2015. Remote Sensing, 9(1), 66. https://doi.org/10.3390/rs9010066

Yu, K., Chen, Y., Liang, L., Gong, A., & Li, J. (2020). Quantitative analysis of the interannual variation in the seasonal water cooling island (WCI) effect for urban areas. Science of The Total Environment, 727, 138750. https://doi.org/10.1016/j.scitotenv.2020.138750

Zhang, X., Friedl, M. A., Schaaf, C. B., Strahler, A. H., & Schneider, A. (2004). The footprint of urban climates on vegetation phenology. Geophysical Research Letters, 31(12). https://doi.org/10.1029/2004GL020137

Zhou, D., Zhao, S., Zhang, L., Sun, G., & Liu, Y. (2015). The footprint of urban heat island effect in China. Scientific Reports, 5(1), 1–11. https://doi.org/10.1038/srep11160

Chapter 2

The Impact of Seasonality and Land Cover Distribution on the Consistency of LST Derived from Landsat 7 and MODIS at a Local Scale: A Case Study in Southern Ontario

2.1 Abstract

Land surface temperature (LST) and air temperature (T_{air}) have been commonly used to analyze urban heat island (UHI) effects throughout the world with noted variations based on vegetation distribution. This research has compared time series LST data acquired from the Moderate Resolution Imaging Spectroradiometer (MODIS) platforms and Landsat 7 Enhanced Thematic Mapper (ETM+) to study UHI effects in the Southern Ontario Area. The time series LST data are also compared with local T_{air} weather stations' data based on surrounding land cover and seasonality. The objective is to identify spatial and seasonal differences and the causes for variations amongst these products with differing spatial resolutions at a localized scale. T_{air} and Landsat 7 LST showed weaker correlations than MODIS LST in sparsely vegetated and urban areas during the summer. Winter's ability to smooth heterogenous surfaces presented stronger relationships with both LST and T_{air} over every land cover, except with coarse spatial resolutions on forested surfaces. Additionally, LST from Landsat 7 showed stronger relationships with LST products from MODIS Terra than Aqua.

2.2 Introduction

Land Surface Temperature (LST) and air temperature (T_{air}) are useful for assessing and mapping earth surface and near-surface thermal conditions using information related to sensible and latent

heat fluxes (Ermida et al., 2020). In urban environments, increased impervious surfaces, reduced vegetated areas with canopy cover, and atmospheric pollution affect the local LST and T_{air} (de Affonseca et al., 2002). As a result, heat absorption from numerous types of urban surfaces and anthropogenic activities lead to urban heat island (UHI) effects with rising LST and T_{air} (Chen et al., 2017). Therefore, examining the temporal and spatial changes of LST and T_{air} is commonly used to study the impact and footprint of UHI caused by urbanization (Streutker, 2003; Q. Yang et al., 2019; D. Zhou et al., 2015).

Satellite-based LST provides comprehensive earth surface temperature data at different spatial resolutions with different temporal resolutions. For example, the most commonly used Moderate Resolution Imaging Spectroradiometer (MODIS) LST data often have a coarse spatial resolution of 1 km with daily overpass frequency which would reveal intra-annual dynamics and overall patterns throughout large areas (Kuenzer et al., 2015). However, its coarse spatial resolution often results in mixed pixels, containing more than one land cover in heterogenous landscapes (Muad & Foody, 2012; Walker et al., 2015). Alternatively, finer spatial resolution sensors, such as with Landsat 7 Enhanced Thematic Mapper (ETM+), have the ability to resolve complex land cover patterns, improve mixed pixels, add detail, and validate coarser maps (Kempeneers et al., 2011). Although many satellite-based LST products are available, there seems to be few direct comparisons at local regional levels.

T_{air} is often measured through weather stations. Much like LST, canopy cover, wind, humidity, and other atmospheric properties affect the local T_{air} experienced at each station (Stewart & Oke, 2012). Vegetated land cover distributions influence T_{air} with its microclimatic effects along with rapid cool and warm air advections (P. Zhang et al., 2014). Its application in assessing UHI is dependent upon its location and the surrounding surface characteristics. For example, measuring T_{air} at airport locations found no evidence of correlation with population accumulation (Almazroui et al., 2013) while using in situ stations located within urban centers

provides contrasting results (Y.-J. Yang et al., 2013). Comparing T_{air} with the LST products provides an additional dimension for understanding the temperature variability in an urban setting.

This study is intended to compare LST products derived from Landsat 7 and MODIS and examine the impact of seasonality and land cover on the relationship between LST and T_{air} at a local scale. As a result of the recent publication using Google Earth Engine (GEE) to simplify methods of obtaining LST from Landsat imagery, an extensive LST comparison acquired at different scales is now easily accessible. This analysis has two main goals; (1) understand the impact of seasonality with different bio-productive surfaces between LST (acquired through both MODIS platforms and Landsat 7 ETM+) and T_{air} and (2) determine the optimal LST scale, platform, and method of derivation based on surface land cover distributions.

2.3 Study Area and Datasets

2.3.1 Study Area

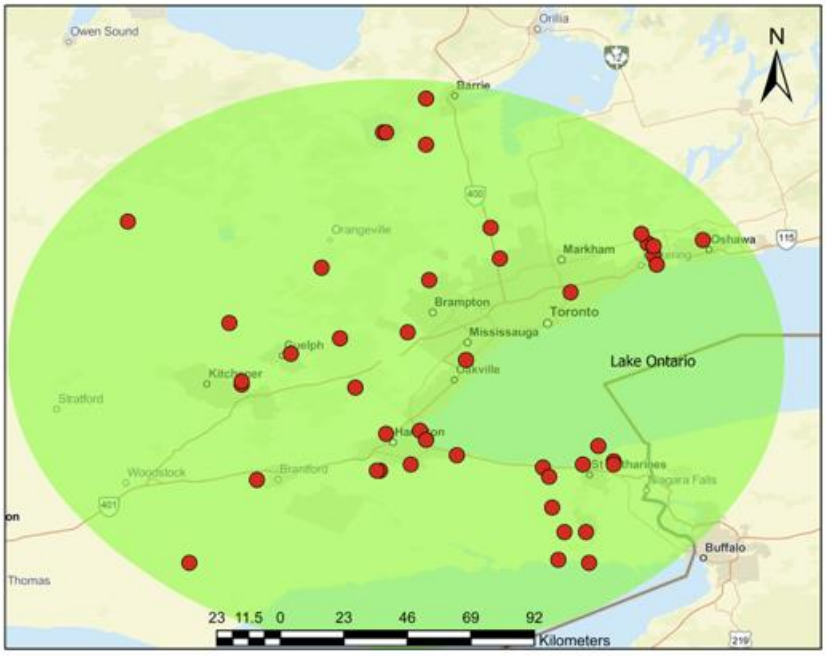

Figure 2.1: The locations (in red) of all weather stations included in this report. The area in green represents the 100 km buffer around Milton encompassing the populated southern Ontario region.

Using the rapidly urbanizing region of Milton, Ontario, Canada as the central point, a 100 km buffer around its urban core was used as the study area in Figure 2.1. It represents the most populated area of Canada and has a variety of different land covers.

2.3.2 In Situ Meteorological Data

Hourly T_{air} data was acquired from the Climate Services department of the Government of Canada's Ministry of Environment and Climate Change. The metadata for each weather station, such as the geographical coordinates, instrument parameters, and station ID were also obtained. In order to maximize the database, all stations within the study area, including the ones which were only temporarily operational and contain data gaps, are included.

For use in a daytime comparison with LST products, the data collected at the nearest hour to the time of acquisition for all products from each satellite platform was used. The LST data derived from Landsat 7 ETM+ products within the area were all obtained within twenty minutes of 16:00. The fluctuations with the overpass time of each of the MODIS platforms results in far more complex comparisons. Both satellites capture daily data throughout a 2.5 hours overpass window over the Milton area. In order to present data at the nearest hour to the overpass time of each satellite, the MODIS Terra data is compared with the 10:00, 11:00, and 12:00 T_{air} measurements while the Aqua data is compared to the 12:00, 13:00, and 14:00 data. In addition, due to the processing employed to derive the level 2 MODIS LST data, both platforms are also compared with the daily average and maximum T_{air} data.

2.3.3 Land Cover Data

Raster and vector land cover maps were provided by Southern Ontario Land Resource Information System (SOLRIS). An accuracy assessment conducted in the same area as this analysis has an overall accuracy of 93% captured by fuzzy error assessment results (Sampson,

2007). The version 3.0 SOLRIS package includes a raster dataset (with all of the land cover designations), a vector land cover changes dataset, and a land cover class corrections dataset (including class updates, accuracy assessment results, and transformations) with a 15 m spatial resolution (Science and Research Branch of the Ministry of Natural Resources and Forestry, 2019).

Simplified land cover classifications are used to reduce the quantity of different land covers to five categories (Forested, Wetland, Lakeside, Agricultural, and Urban). 'Wetland' refers to any surface where the water table is either seasonally or permanently at, near, or above the substrate surface (Science and Research Branch of the Ministry of Natural Resources and Forestry, 2019). Any weather station adjacent to a large water body is classified as "lakeside".

2.3.4 Remote Sensing Data

Imagery was collected from sensors with different spatial and temporal resolutions, obtainable product levels, and processing requirements. Both remote sensing products use similar variables related to T_{air} such as albedo, LST, and normalized difference vegetation index (NDVI) (Cristobal et al., 2008).

2.3.4.1 MODIS LST

Selection of MODIS as coarse resolution sensors for the comparison is based on data availability, product accuracy, and an established foundation of land cover analysis reports. Consisting of two platforms launched in a similar time period as Landsat 7 ETM+ (although the Aqua platform was released in 2002), MODIS products can successfully provide LST data with spatial representativeness being a limiting factor (Bosilovich, 2006). A T-based validation analysis over rice farming and densely forested regions provided highly accurate LST error results with small biases (Coll et al., 2009). When compared against T_{air} stations, a report in Egypt found MODIS LST can be overestimated by as much as 5˚C (El Kenawy et al., 2019) and stronger relationships

were found in non-forested cover types compared to areas with dense canopy coverage (Mildrexler et al., 2011).

MOD11A1 and MYD11A1 are level 3 LST products from the MODIS Terra and Aqua platforms on a 1200 x 1200 pixel grid with an exact spatial resolution of 0.928 km x 0.928 km in the Sinusoidal projection (Zhengming Wan, 2013). LST pixel values are generated using the split-window algorithm (SWA) with clear-sky conditions and are averaged in areas with overlapping pixels with overlapping areas of weight (Zhengming Wan, 2013). Its advertised one-day temporal resolution is optimistic based on the availability of clear sky distribution. Because the thermal infrared (TIR) bands on the MODIS sensors are unable to penetrate clouds, any pixel experiencing cloudy interference must be skipped (Z. Wan et al., 2004).

Both satellite platforms operate on a sun-synchronous orbit (Urban et al., 2013). Based on the estimates provided by the NASA LaRC Satellite Overpass Predictor (https://cloudsway2.larc.nasa.gov/cgi-bin/predict/predict.cgi), the overpass times at the selected location for the Terra platform ranges between 10:00 and 12:30 and 12:00 to 14:30 for Aqua in the local Eastern Standard Time.

2.3.4.2 Landsat 7 Derived LST

Landsat 7 ETM+ was the ideal choice for finer resolution LST data. It is a major leap forward from its predecessors with multispectral spatial resolutions ranging from its 15 meters panchromatic band to the 60 meters TIR band (L. Yang et al., 2003). Ermida et al. (2020) presents an innovative method using the Statistical Mono-Window Algorithm (SMW) in Google Earth Engine to simplify the calculations needed to derive LST by reducing the amplitude of data required for time series analyses. Access to the algorithm is simply introduced through the use of the JavaScript function “require(…)”, thus eliminating the necessity to download bulk quantities of data.

To access LST, the surface reflectance is calculated from the radiative transfer for atmospheric data using the Landsat Ecosystem Disturbance Adaptive Processing System Algorithm (Ermida et al., 2020). A cloud mask is applied to eliminate interference. Data from the Advanced Spaceborne Thermal Emission and Reflection Radiometer Global Emissivity Data Set (ASTER) is spectrally adjusted and modified accounting for phenology and snow coverage using shortwave infrared Landsat data (Malakar et al., 2018). The SMW algorithm used within the Ermida et al. (2020) code presents two options for achieving LST, the direct application of instantaneous ASTER emissivity corrected values or the inclusion of NDVI-based corrections. With the latter option, the coarser TIR band can be resampled with an enhanced spatial resolution from NDVI and surface emissivity to generate LST (Rodriguez-Galiano et al., 2012). For the purposes of understanding the influence which NDVI has upon LST, both methods are implemented.

2.4 Methodology

The first step involves the data extraction from all meteorological stations collecting hourly data within the study area from January 1, 2000 to December 31, 2019. Figure 2.1 displays the locations of all 46 weather stations used in the analysis. From each station, all 16:00 data was used for comparison with the Landsat 7 ETM+ derived LST data. Since the time of the data acquired from both MODIS platforms ranges from 10:00 to 14:30, the daily mean and maximum temperature recordings are used along with every hour within the range, relative to its corresponding satellite. Linear regression analyses are conducted using geographical variables such as location and land cover type and performed through R. All remote sensing data is acquired from Google Earth Engine.

A 100 m buffer is implemented surrounding each weather station to determine the dominant land cover classification from SOLRIS data. Table 2.1 displays how the classifications

are simplified into five main categories. All stations classified under each surface type are grouped together.

Table 2.1: The reclassification of all land covers into five manageable categories. Any station located in proximity to an open water land cover is reclassified as a lakeside station regardless of the dominant land cover within 100 m.

Agricultural	Urban	Lakeside	Forested	Wetlands
Plantations - Tree Cultivated	Transportation	Open Water	Forest	Treed Swamp
Hedge Rows	Built-Up Area - Pervious		Coniferous Forest	Thicket Swamp
Tilled	Built-Up Area - Impervious		Mixed Forest	Marsh
Undifferentiated (orchards, vineyards, perennial crops, and idle land)	Extraction		Deciduous Forest	

Based on the provided longitude and latitude data from each weather station, all MODIS (Terra and Aqua) and Landsat 7 LST data are extracted for the time series analysis. Each year is divided into two parts representing the changing land surface distribution amongst seasons (summer and winter). Rather than utilizing the four traditional seasons, each year only uses two to describe the changing land surface characteristics. The warmer portion of the year, referred to as "summer" (days 100-290), ranges from mid-spring (April 9/10) to mid-autumn (October 16/17) and the colder portion (named "winter" in reference to days 1-99 and 291-366) indicates the rest of the year. The summer content is largely unaffected by snow or ice coverage and is representative of vegetation growth and increased solar radiation as opposed to the winter.

Once all the T_{air} and LST data is extracted for analysis, only the data that exists when in situ measurements and remote sensing data was simultaneously collected is utilized. A comparison is detailed based on time of year and land covers using R^2 values, root-mean square error (RMSE), bias, and the number of observations.

An additional comparison between satellites excludes T_{air} measurements. Several large areas with land covers consistently within each category are selected and aggregated. Within each land cover designation, 70 points are randomly selected accessing the mean temperature within a 50 m homogenous buffer. The mean LST measurements from each category and platform are compared to determine the quantity and quality of the variations of data.

2.5 Results

As a result of the vastly different temporal resolutions amongst the remote sensing platforms, there is far less T_{air} data to compare with the Landsat 7 LST. The validity of all analyses are based on p-values and the R^2 values which measures the quantity of variance in the dependent variable explained through the independent variable (Y. Zhang et al., 2012). All regression results from these analyses produced statistically significant p-values with a few exceptions (all of which are related to the small quantity of LST data to compare with wetlands T_{air} measurements due to the limited quantity of stations on or near wetlands). In addition, the RMSE and bias were included to further understand the distribution of residuals and real values (Cristobal et al., 2008). The bias refers to subtracting the LST by T_{air}, or in the Landsat 7/MODIS comparison, MODIS LST minus Landsat 7 LST.

2.5.1 Impact of Seasonality

Winter results provide a stronger relationship compared with the summer. LST from Terra with T_{air} recorded at 12:00 provides the strongest overall relationship with either of the MODIS missions with an R^2 value of 0.79 in Table 2.2. The Landsat 7 NDVI-derived LST's relationship with T_{air} is a marginal improvement with RMSE of 4.16 and an R^2 value of 0.81, slightly higher than ASTER-derived data. In contrast, the summer data in Table 2.3 correlations are far less robust. Comparisons with MODIS data have R^2 values as high as 0.45 while the Landsat 7 LST overall data comparison is slightly weaker with R^2 values of 0.35.

Amongst the two Landsat 7 LST datasets, the results are very similar. NDVI corrections produce marginally improved R^2 and RMSE values; however, the bias is weaker.

Table 2.2: The results from regression analyses for all three satellites for days 1-99 and 291-366 of every year between 2000 and 2019. The T_{air} relationships with the best R^2 results are included. All p-values are < 0.001.

LST Variables	R-Squared Value	RMSE	Bias	Optimal T_{air} measurement
Aqua MODIS	0.75	4.57	2.22	14:00
Terra MODIS	0.79	4.27	1.74	12:00
Landsat 7 ASTER with NDVI	0.81	4.16	2.48	16:00
Landsat 7 ASTER	0.78	4.50	1.68	16:00

Table 2.3: The results from regression analyses for all three satellites for days 100-290 of every year between 2000 and 2019. The T_{air} relationships with the best R^2 results are included. All p-values are < 0.001.

Regression Variables	R-Squared Value	RMSE	Bias	Optimal T_{air} measurement
Aqua MODIS	0.41	5.16	9.68	DAILY MEAN
Terra MODIS	0.45	4.64	2.73	DAILY MAX
Landsat 7 ASTER with NDVI	0.35	6.11	5.28	16:00
Landsat 7 ASTER	0.35	6.34	4.59	16:00

2.5.2 Impact of Land Cover at Meteorological Stations

The summer and winter analyses developed differing conclusions regarding the land cover in which strongest relationships between LST and T_{air} exist. In the summer (Table 2.4), the wetland surfaces had the most robust correlations with MODIS at R^2 values as high as 0.69 (Terra and the daily maximum T_{air}) and the smallest RMSE. Meanwhile, both Landsat 7 LST measurements failed to collect enough data from stations located near wetlands. With the other land covers, R^2 and RMSE results between fine resolution LST data and T_{air} were only slightly weaker than

MODIS relationships with forested and lakeside stations compared to larger deviations with agriculture and urban.

With the winter comparisons (Table 2.5), Landsat 7 results are stronger than MODIS; however, only marginally better in agricultural and urban areas. Forested weather stations' data during the cold season exhibit the largest deviation in variance explained through Landsat 7 LST (R^2 values of 0.67 without NDVI) over the highest MODIS R^2 values of 0.50. All other land covers yield similar comparisons with slight improvements when NDVI corrections are applied to calculate LST.

The number of observations with Landsat 7 is a continuous issue throughout the analysis. Wetlands results with Landsat 7 are insufficient throughout both seasons. Although conclusions can be drawn with forested land covers, the quantity of winter observations limits the validity.

A visual analysis of the plots for individual weather stations was necessary to ensure that the temperature variations and patterns throughout each season in each year are followed closely. Although some stations have far more data than others, certain parameters are required to complete a thorough visual examination. T_{air} station dates which contain data recorded from both remote sensing platforms are used for the analysis. Figure 2.2 displays patterns that Landsat 7 (with NDVI corrections) LST data has with MODIS Aqua LST and the daily mean T_{air} recordings during the summer and Figure 2.3 has a similar comparison except with MODIS Terra LST during the winter. Although the satellite produced LST data differs from the ground T_{air} data, winter patterns appear more aligned.

Table 2.4: The results from regression analyses for all three satellites for days 1-99 and 291-366 of every year between 2000 and 2019 based on the land cover which each in situ meteorological station was located on. Results include the best R^2 results with the associated T_{air} measurement for MODIS sensors in brackets along with the number of observations (Obs.). All p-values are < 0.001 with the exceptions of the Landsat 7 NDVI wetlands study (p-value = NA) and Landsat 7 ASTER wetlands study (p-value = 0.001).

LST Variables	Agricultural		Urban		Lakeside		Forested		Wetland	
	R^2	Obs.	R^2	Obs.	R^2	Obs.	R^2	Obs.	R^2	Obs.
Aqua MODIS	0.80 (14:00)	2744	0.80 (14:00)	5036	0.68 (12:00)	1964	0.49 (12:00)	883	0.89 (14:00)	459
Terra MODIS	0.83 (12:00)	3446	0.82 (12:00)	5952	0.73 (12:00)	2477	0.50 (12:00)	980	0.91 (11:00)	620
Landsat 7 ASTER with NDVI	0.86	96	0.84	188	0.75	90	0.60	23	NA	2
Landsat 7 ASTER	0.83	130	0.81	277	0.74	130	0.67	34	0.97	5

Table 2.5: The results from regression analyses for all three satellites for days 100-290 of every year between 2000 and 2019 based on the land cover which each in situ meteorological station was located on. Results include the best R2 results with the associated T_{air} measurement for MODIS sensors in brackets along with the number of observations (Obs.). All p-values are < 0.001 with the exceptions of both Landsat 7 wetlands studies which produce a p-value of NA.

LST Variables	Agricultural		Urban		Lakeside		Forested		Wetland	
	R^2	Obs.	R^2	Obs.	R^2	Obs.	R^2	Obs.	R^2	Obs.
Aqua MODIS	0.47 (Mean)	6782	0.55 (Mean)	11982	0.40 (Max)	4831	0.53 (12:00)	1695	0.65 (Max)	1046
Terra MODIS	0.52 (Mean)	7713	0.58 (11:00)	13058	0.45 (10:00)	5511	0.53 (10:00)	1903	0.69 (Max)	1225
Landsat 7 ASTER with NDVI	0.37	193	0.46	469	0.32	204	0.47	74	NA	1
Landsat 7 ASTER	0.36	232	0.44	569	0.37	256	0.38	85	NA	1

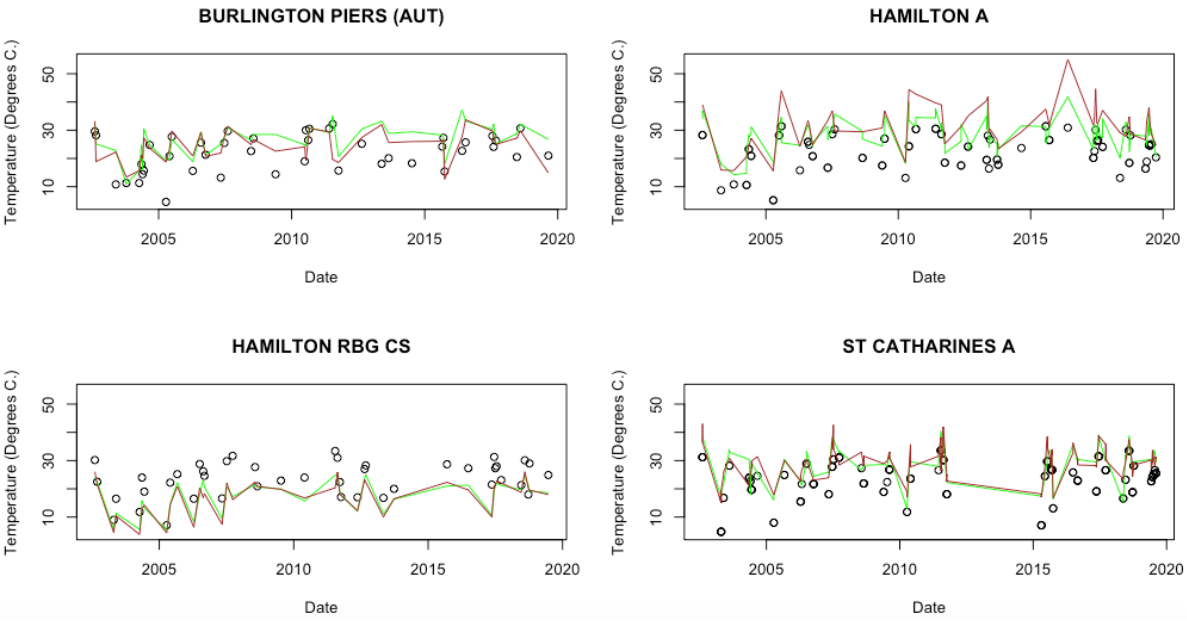

Figure 2.2: The charts comparing the Landsat 7 NDVI-derived LST and MODIS Aqua LST along with average air temperature at the stations with the most data points during the summer. The green line represents MODIS LST, the brown line represents Landsat 7 LST and the black points represent average air temperature observations.

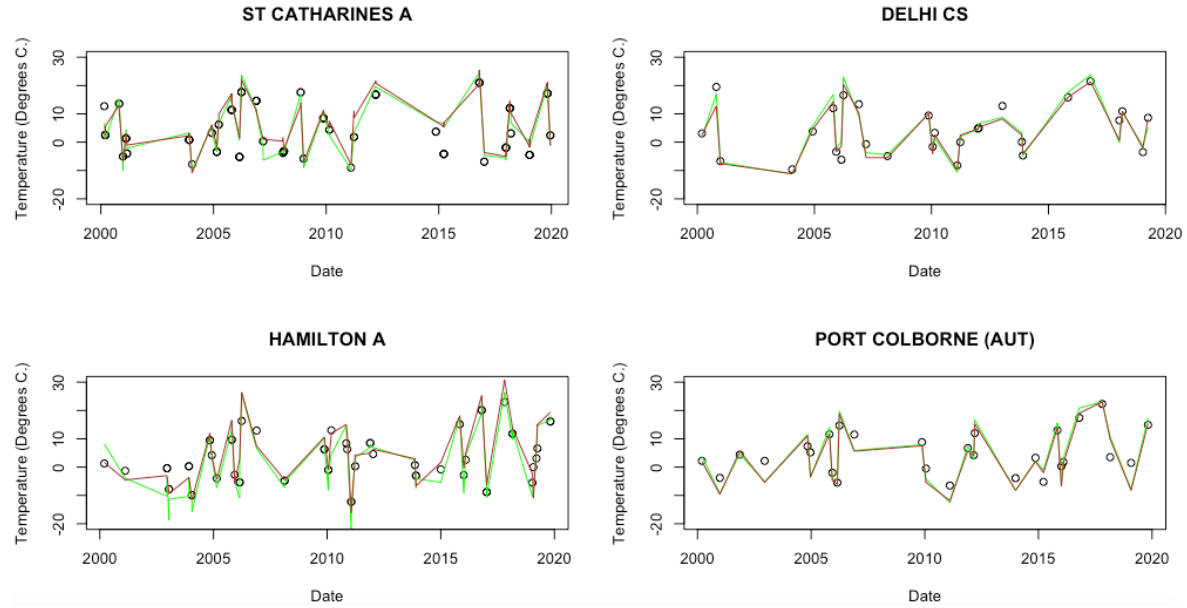

Figure 2.3: The charts comparing the Landsat 7 NDVI-derived LST and MODIS Terra LST along with average air temperature at the stations with the most data points during the winter. The green line represents MODIS LST, the brown line represents Landsat 7 LST and the black points represent average air temperature observations.

2.5.3 Land Cover LST Comparison

With the scaled LST analysis excluding T_{air}, the relationships are marginally stronger with the MODIS Terra platform and Landsat 7 with NDVI across both seasons and every land cover. Much like the T_{air} comparisons, the winter has significantly stronger correlations with the only exception being open water land covers.

Winter results in Table 2.6 determined fine resolution LST with NDVI corrections and coarse resolution data from MODIS Terra have the strongest relationship based on every conducted measurement. For summer results in Table 2.7, Landsat 7 LST using NDVI has an improved relationship with R^2 values ranging from 0.74 to 0.91 with Terra. Relationships over water bodies provided the strongest summer R^2 and RMSE (0.91 and 1.98 respectfully) results between Landsat 7 and the Terra sensor.

Table 2.6: The comparison analysis using the mean values from 70 randomly selected points within each land cover category during the winter. Both methods of acquiring LST from Landsat 7 have a superior relationship to MODIS Terra. All p-values are < 0.001.

ASTER (Landsat 7) & Terra (MODIS) during Winter

Land Cover	R^2	RMSE	Bias
Agricultural	0.88	3.27	0.24
Urban	0.90	2.86	0.38
Water	0.80	2.24	2.15
Forested	0.91	2.50	0.77
Wetland	0.90	2.70	0.67

ASTER (Landsat 7) & Aqua (MODIS) during Winter

Land Cover	R^2	RMSE	Bias
Agricultural	0.89	3.14	1.51
Urban	0.86	3.51	1.38
Water	0.78	2.33	2.22
Forested	0.88	3.22	1.74
Wetland	0.86	3.16	1.84

NDVI (Landsat 7) & Terra (MODIS) during Winter

Land Cover	R^2	RMSE	Bias
Agricultural	0.89	3.18	-0.18
Urban	0.92	2.73	-0.26
Water	0.83	2.05	1.47
Forested	0.93	2.44	0.04
Wetland	0.91	2.49	-0.47

NDVI (Landsat 7) & Aqua (MODIS) during Winter

Land Cover	R^2	RMSE	Bias
Agricultural	0.89	3.31	1.01
Urban	0.88	3.27	0.77
Water	0.79	2.29	1.46
Forested	0.88	3.27	1.10
Wetland	0.89	2.90	0.76

Table 2.7: Similar comparison analysis to Table 2.6 except in the summer. Once again, the relationship Landsat 7 LST has with MODIS Terra is a significant improvement when compared with Aqua. All p-values are < 0.001.

ASTER (Landsat 7) & Terra (MODIS) during Summer

Land Cover	R^2	RMSE	Bias
Agricultural	0.75	3.28	1.10
Urban	0.75	3.54	-0.36
Water	0.74	3.62	1.32
Forested	0.77	3.31	0.62
Wetland	0.71	3.14	3.47

ASTER (Landsat 7) & Aqua (MODIS) during Summer

Land Cover	R^2	RMSE	Bias
Agricultural	0.69	3.42	1.46
Urban	0.68	3.84	0.27
Water	0.69	4.04	1.47
Forested	0.69	3.64	1.27
Wetland	0.69	3.11	3.59

NDVI (Landsat 7) & Terra (MODIS) during Summer

Land Cover	R^2	RMSE	Bias
Agricultural	0.76	2.96	0.57
Urban	0.76	3.16	-1.36
Water	0.91	1.98	0.81
Forested	0.80	2.80	-0.30
Wetland	0.74	2.69	2.95

NDVI (Landsat 7) & Aqua (MODIS) during Summer

Land Cover	R^2	RMSE	Bias
Agricultural	0.69	3.13	0.99
Urban	0.69	3.50	-0.65
Water	0.87	2.34	0.90
Forested	0.74	3.09	0.34
Wetland	0.68	2.80	3.10

2.6 Discussion

A major obstacle confronted in this analysis relates to the vastly different quantities of imagery available from each satellite platform. The 16 days revisit cycle for the Landsat 7 satellite limits the availability of data to compare and analyze with MODIS and T_{air}. Both MODIS platforms calculate the LST based on clear-sky pixel coverage masking clouds with the cloudmask algorithm (Zhengming Wan, 2013), maximizing the quantity of available imagery. With Landsat 7 derived LST, only 479 observations are possible (provided every overpass occurs during a clear sky) at each location throughout the provided time frame compared to the near daily results optimistically attainable from MODIS.

The results based on time of year remain consistent with previous research comparing MODIS results with T_{air}. P. Zhang et al. (2014) noted the much stronger relationship that MODIS LST has in the winter (daytime and nighttime) when compared with the summer daytime (the nighttime results were stronger due to a lacking solar radiation variable) with fluctuations based on ecological context. Similar conclusions are made with the analysis in the Milton region with both scales due to the change that occurs in winter. Surface conditions, changes to the soil moisture content, and heterogeneity of the surrounding land covers can play a major role in determining the variations between seasons.

2.6.1 Impact of Seasonality

Winter seasonal energy exchanges heavily affect the comparisons in this study. The albedo consistency varies based on low temperature snow coverage over agriculture, grassland, near-surface shrubbery, and diversified canopy cover with heterogenous types of forest life (Essery, 2013). The impact is limited to the spatial resolution each sensor possesses and the ecosystems surrounding the study site. In addition, due to the time frame of the winter analysis (mid-October to mid-April), discrepancies can occur due to the varying degrees of snow coverage throughout the time interval. A temperature bias happens as the year progresses from the winter solstice resulting in stronger solar radiation (X. Zhou et al., 2014). The necessity to encompass the entire period of each year where snow cover is possible enhances the ability to identify the true relationship LST has with T_{air}, regardless of circumstances.

Overall, the finer scale LST products with NDVI corrections retained the strongest relationships with T_{air}. With an R^2 value of 0.81 (slightly higher than with coarse sensors) and RMSE of 4.16 (slightly lower than with coarse sensors), the winter's ability to homogenize the surrounding environment increases the reliability of surface temperature to determine near-surface temperatures. The relationship difference between coarse and fine resolution sensors is

minor with the exception of in situ stations surrounded by forested surfaces. Finer resolution LST and T_{air} have R^2 values between 0.60 and 0.67 compared to 0.50 with coarse resolution LST.

The summer comparisons lead to alternative results with each land cover and scale. Surface temperatures are high with non-evaporating surfaces and lower with water bodies due to the radiant reflection. The reflected solar radiation on the impervious pixels can impact the LST strongly, especially at a finer scale. Vegetated covers also have low radiant temperature as a result of a reduction in heat stored in the soil from transpiration (Sahana et al., 2016). Overall, coarse resolution LST data possesses the strongest R^2 and RMSE results, especially with the MODIS Terra platform. Agricultural and urban stations have the largest difference in relationship between coarse and fine resolutions while lakeside an forested stations displayed minor improvements.

The diversity of temperatures across each land cover poses strong catalysts for how the remote sensing derived LST relates to T_{air}, depending on scale. Each biome maintains its own unique set of physical, climatological, botanical, and animal habitat characteristics which cause variances that are not expressed through simple temperature observations and predictions (P. Zhang et al., 2014). The diversity of variables within dense and sparse vegetation during the growing season affect the temperature on the ground and in the air above it. Comparing the coarse spatial resolution of MODIS to the much finer Landsat 7 data, the additional environmental factors can cause fluctuations, especially with agriculture and urban surfaces.

2.6.2 Land Cover Impact

Variations dependent on land cover type imply discrepancies based on vegetation cover, impervious surface distribution, and soil type. Areas with a lower surface albedo are more likely to result in a greater overestimation of daytime temperature than higher surface albedo (El Kenawy et al., 2019). This is reflected with the weaker relationship at lakeside stations with

larger RMSE results. The phenology of a land cover can also have a major impact upon the temperature variations. For example, summer results in vegetated areas with increased canopy coverage provided stronger results with Landsat 7.

MODIS has advantages over finer spatial resolution sensors as it subsumes the detail throughout heterogenous urban and vegetated areas across broad geographical extents (Walker et al., 2015). The precision useful with Landsat 7 LST analyses in the summer serves as a disadvantage when compared with in situ observations due to the increased likelihood of variables affecting T_{air} outside of the 30 m resolution pixels. For example, the RMSE values in Table 2.3 and the Figure 2.2 patterns display how MODIS sensors have improved abilities for determining LST more closely aligned T_{air}. Opposing results occur throughout the homogenously transformed surfaces during the winter season with finer spatial resolutions yielding superior results expressed through R^2 and RMSE values.

Defining an exact location within pixels of either 1 km or 30 m spatial resolutions challenges the ability to acquire specified temperatures for that location. Although this issue exists with each land cover classification, the lakeside stations are the most problematic. Its issues are reduced in the winter with snow cover affecting the spectral reflectance over water in a similar manner to land; however, complications are exposed in the summer time frame. In addition to the provided coordinates for each station not being detailed enough to have their locations precisely georeferenced, the proximity to the large Lake Ontario water body and proportion of land surfaces incorporated into the pixels affects the classification with MODIS calculations more than Landsat 7. The open space over water bodies may also increase humidity and wind related elements, which affect T_{air} observations.

The forested in situ station's T_{air} relationship with coarse resolution LST revealed the only instance where summer produced a stronger seasonal relationship. Due to the dense flora, the Canadian winter is unable to completely homogenize the forest environment. The canopy

density produces low R^2 values in the winter which finer resolutions can marginally improve upon. Considering the strong results in the LST regression analysis based on scale, forested land covers inhabit variables, relevant to vegetation density and height, affecting air which snow coverage fails to smooth at coarse resolutions.

The linear regression analyses between LST scales produced robust results, especially over forested and wetlands pixels (compared with the T_{air} analyses which lacked sufficient data). In contrast to the limited number of observations at each weather station for comparisons with Landsat, Terra data produced far more results with superior variance and reliability in each regression analysis. The application of 70 randomly selected points for scaled LST comparisons allowed for more complete representations with land covers where in situ stations were seldomly placed. The summer comparison between Landsat 7 (with NDVI) and Terra delivered the strongest R^2 and RMSE results, especially over water (due to its homogeneity) and forests.

In the winter, the factors which affect the variance in summer LST such as solar radiation, vegetation growth, surface roughness, and albedo are reduced. Water is the land cover with the most variation and highest bias amongst the two platforms with vastly different spatial resolutions (which contrasts summer results). The stronger relationship within water pixels in the summer is due to homogeneity with both fine and coarse spatial resolutions. Winter provides more variance with LST at a coarser scale.

2.6.3 ASTER derived emissivity values VS. NDVI corrected values

The minor differentiation amongst the two methods of deriving LST from Landsat 7 imagery is definitive for this region. The only category which NDVI corrected values are not superior is around Lakeside and Forested in situ stations. NDVI LST data has a significantly stronger relationship with forested T_{air} in the summer. In contrast, ASTER LST values had an R^2 improvement of 0.0732 in the winter. The only other instance is with lakeside stations during the

summer. Otherwise, NDVI corrected LST maintains a dominance. NDVI plays a stronger role with summer data due to the influx of vegetation across each land cover. In the winter, even with snow coverage and a major reduction of vegetation life, the results continue to reveal the necessity for NDVI corrections on the ASTER emissivity values.

2.7 Conclusion

When compared to T_{air} measurements from calendar days 100 to 290, success with coarse resolution products is reflective of previous research. MODIS imagery maintained overall R^2 values between 0.41 and 0.45 while Landsat 7 results were 0.35 with a weaker RMSE. For the remainder of the year, Landsat 7 is more highly correlated with overall R^2 value as high as 0.81 while MODIS data is between 0.71 and 0.79 with similar RMSE.

Individual land covers produce much more varied results based on phenology, albedo, and moisture content on the heterogenous land surfaces during the summer. As a result, the summer conditions for a finer resolution satellite does not account for the greater variety of variables present in heterogenous surfaces. The differences in variances explained through coarse and fine resolution satellite imagery with T_{air} over lakeside and forested stations are marginally smaller (R^2 difference within 0.08) compared to agriculture and urban surfaces. In addition, coarse resolution LST explains more variance in T_{air} at forested locations during summer due to the winter's inability to homogenize the landscape due to dense flora content.

When comparisons based on the surrounding land covers for each in situ observation are conducted, Landsat 7 derived LST concluded with R^2 values between 0.03 and 0.15 lower than MODIS in summer. Results with agricultural and urban in situ stations provided the most variations between air measurements and different LST scales. This emphasizes the disadvantage for using satellites with a finer spatial resolution during the summer due to a greater availability of heterogenous factors over sparse vegetation and low-density impervious spaces. Further

assessment is needed on the atmospheric variability in a variety of environments based on the radiation, atmospheric contents, and surface biomass factors.

The availability of weather stations in or near wetlands was a limitation in the LST comparisons made with T_{air}. For Landsat 7 data, 1 to 5 observations are entirely insufficient to make a distinction on its accuracy. Future exploration of the relationship with T_{air} stations may provide greater insight in the correlation with fine resolution LST located at wetlands.

2.8 References

Almazroui, M., Islam, M. N., & Jones, P. D. (2013). Urbanization effects on the air temperature rise in Saudi Arabia. Climatic Change, 120(1), 109–122. https://doi.org/10.1007/s10584-013-0796-2

Bosilovich, M. G. (2006). A comparison of MODIS land surface temperature with in situ observations—Bosilovich—2006—Geophysical Research Letters—Wiley Online Library. Geophysical Research Letters, 33(L20112). https://doi.org/10.1029/2006GL027519

Chen, Y.-C., Chiu, H.-W., Su, Y.-F., Wu, Y.-C., & Cheng, K.-S. (2017). Does urbanization increase diurnal land surface temperature variation? Evidence and implications. Landscape and Urban Planning, 157, 247–258. https://doi.org/10.1016/j.landurbplan.2016.06.014

Coll, C., Wan, Z., & Galve, J. M. (2009). Temperature-based and radiance-based validations of the V5 MODIS land surface temperature product. Journal of Geophysical Research: Atmospheres, 114(D20). https://doi.org/10.1029/2009JD012038

Cristobal, J., Ninyerola, M., & Pons, X. (2008). Modeling air temperature through a combination of remote sensing and GIS data. Journal of Geophysical Research, 113(D13106). https://doi.org/10.1029/2007JD009318

de Affonseca, M. S., Alves, R. N., Junior, J. T., & de Almeida, C. E. (2002). The influence of urbanization on natural radiation levels in anomalous areas. Journal of Environmental Radioactivity, 63(1), 65–75. https://doi.org/10.1016/S0265-931X(02)00016-4

El Kenawy, A. M., Hereher, M. E., & Robaa, S. M. (2019). An Assessment of the Accuracy of MODIS Land Surface Temperature over Egypt Using Ground-Based Measurements. Journal of Remote Sensing, 11. https://doi.org/10.3390/rs11202369

Ermida, S. L., Soares, P., Mantas, V., Gottsche, F.-M., & Trigo, I. F. (2020). Google Earth Engine Open-Source Code for Land Surface Temperature Estimation from the Landsat Series. Journal of Remote Sensing, 12(9). https://doi.org/10.3390/rs12091471

Essery, R. (2013). Large-scale simulations of snow albedo masking by forests. Geophysical Research Letters, 40(20), 5521–5525. https://doi.org/10.1002/grl.51008

Kempeneers, P., Sedano, F., Seebach, L., Strobl, P., & San-Miguel-Ayanz, J. (2011). Data Fusion of Different Spatial Resolution Remote Sensing Images Applied to Forest-Type Mapping. IEEE Transactions on Geoscience and Remote Sensing, 49(12), 4977–4986. https://doi.org/10.1109/TGRS.2011.2158548

Kuenzer, C., Klein, I., Ullmann, T., Georgiou, E. F., Baumhauer, R., & Dech, S. (2015). Remote Sensing of River Delta Inundation: Exploiting the Potential of Coarse Spatial Resolution, Temporally-Dense MODIS Time Series. Remote Sensing, 7(7), 8516–8542. https://doi.org/10.3390/rs70708516

Malakar, N. K., Hulley, G. C., Hook, S. J., Laraby, K., Cook, M., & Schott, J. R. (2018). An Operational Land Surface Temperature Product for Landsat Thermal Data: Methodology and Validation. IEEE Transactions on Geoscience and Remote Sensing, 56(10), 5717–5735. https://doi.org/10.1109/TGRS.2018.2824828

Mildrexler, D. J., Zhao, M., & Running, S. W. (2011). A global comparison between station air temperatures and MODIS land surface temperatures reveals the cooling role of forests. Journal of Geophysical Research: Biogeosciences, 116(G3). https://doi.org/10.1029/2010JG001486

Muad, A. M., & Foody, G. M. (2012). Super-resolution mapping of lakes from imagery with a coarse spatial and fine temporal resolution. International Journal of Applied Earth Observation and Geoinformation, 15, 79–91. https://doi.org/10.1016/j.jag.2011.06.002

Rodriguez-Galiano, V., Pardo-Iguzquiza, E., Sanchez-Castillo, M., Chica-Olmo, M., & Chica-Rivas, M. (2012). Downscaling Landsat 7 ETM+ thermal imagery using land surface temperature and NDVI images. International Journal of Applied Earth Observation and Geoinformation, 18, 515–527. https://doi.org/10.1016/j.jag.2011.10.002

Sahana, M., Ahmed, R., & Sajjad, H. (2016). Analyzing land surface temperature distribution in response to land use/land cover change using split window algorithm and spectral radiance model in Sundarban Biosphere Reserve, India. Modeling Earth Systems and Environment, 2(2), 81. https://doi.org/10.1007/s40808-016-0135-5

Sampson, P. (2007). SOLRIS Accuracy Assessment Report 1: Golden Horseshoe Area (SOLRIS study area A) (Accuracy Assessment 1 (Version 2.0); p. 53). Ministry of Natural Resources.

Science and Research Branch of the Ministry of Natural Resources and Forestry. (2019). Southern Ontario Land Resource Information System (SOLRIS) Version 3.0: Data Specifications. Ministry of Natural Resources.

Stewart, I. D., & Oke, T. R. (2012). Local Climate Zones for Urban Temperature Studies. Bulletin of the American Meteorological Society, 93(12), 1879–1900. https://doi.org/10.1175/BAMS-D-11-00019.1

Streutker, D. R. (2003). Satellite-measured growth of the urban heat island of Houston, Texas. Remote Sensing of Environment, 85(3), 282–289. https://doi.org/10.1016/S0034-4257(03)00007-5

Urban, M., Eberle, J., Hüttich, C., Schmullius, C., & Herold, M. (2013). Comparison of Satellite-Derived Land Surface Temperature and Air Temperature from Meteorological Stations on the Pan-Arctic Scale. Remote Sensing, 5(5), 2348–2367. https://doi.org/10.3390/rs5052348

Walker, J. J., de Beurs, K. M., & Henebry, G. M. (2015). Land surface phenology along urban to rural gradients in the U.S. Great Plains. Remote Sensing of Environment, 165, 42–52. https://doi.org/10.1016/j.rse.2015.04.019

Wan, Z., Zhang, Y., Zhang, Q., & Li, Z.-L. (2004). Quality assessment and validation of the MODIS global land surface temperature. International Journal of Remote Sensing, 25(1), 261–274. https://doi.org/10.1080/0143116031000116417

Wan, Zhengming. (2004). Land Surface Temperature Measurements from EOS MODIS Data (No. NAS5-31370). University of California. https://modis.gsfc.nasa.gov/MODIS/LAND/REPORTS/wan.2003.finalReport.pdf

Wan, Zhengming. (2013). Collection-6 MODIS Land Surface Temperature Products Users' Guide. University of California. https://lpdaac.usgs.gov/documents/118/MOD11_User_Guide_V6.pdf

Yang, L., Huang, C., Homer, C. G., Wylie, B. K., & Coan, M. J. (2003). An approach for mapping large-area impervious surfaces: Synergistic use of Landsat-7 ETM+ and high spatial resolution imagery. Canadian Journal of Remote Sensing, 29(2), 230–240. https://doi.org/10.5589/m02-098

Yang, Q., Huang, X., & Tang, Q. (2019). The footprint of urban heat island effect in 302 Chinese cities: Temporal trends and associated factors. Science of The Total Environment, 655, 652–662. https://doi.org/10.1016/j.scitotenv.2018.11.171

Yang, Y.-J., Wu, B.-W., Shi, C., Zhang, J.-H., Li, Y.-B., Tang, W.-A., Wen, H.-Y., Zhang, H.-Q., & Shi, T. (2013). Impacts of Urbanization and Station-relocation on Surface Air Temperature Series in Anhui Province, China. Pure and Applied Geophysics, 170(11), 1969–1983. https://doi.org/10.1007/s00024-012-0619-9

Zhang, P., Bounoua, L., Imhoff, M. L., Wolfe, R. E., & Thome, K. (2014). Comparison of MODIS Land Surface Temperature and Air Temperature over the Continental USA Meteorological Stations. Canadian Journal of Remote Sensing, 40(2), 110–122. https://doi.org/10.1080/07038992.2014.935934

Zhang, Y., Balzter, H., & Wu, X. (2012). Spatial–temporal patterns of urban anthropogenic heat discharge in Fuzhou, China, observed from sensible heat flux using Landsat TM/ETM+ data. International Journal of Remote Sensing, 34(4), 1459–1477. https://doi.org/10.1080/01431161.2012.718465

Zhengming Wan, & Dozier, J. (1996). A generalized split-window algorithm for retrieving land-surface temperature from space. IEEE Transactions on Geoscience and Remote Sensing, 34(4), 892–905. https://doi.org/10.1109/36.508406

Zhou, D., Zhao, S., Zhang, L., Sun, G., & Liu, Y. (2015). The footprint of urban heat island effect in China. Scientific Reports, 5(1), 1–11. https://doi.org/10.1038/srep11160

Zhou, X., Matthes, H., Rinke, A., Klehmet, K., Heim, B., Dorn, W., Klaus, D., Dethloff, K., & Rockel, B. (2014). Evaluation of Arctic Land Snow Cover Characteristics, Surface Albedo, and Temperature during the Transition Seasons from Regional Climate Model Simulations and Satellite Data. Advances in Meteorology, 2014. https://doi.org/10.1155/2014/604157

Chapter 3

Urban Heat Island Footprint Effects on Bio-Productive Rural Land Covers Surrounding a Low Density Urban Center

3.1 Abstract

The urban heat island (UHI) is a common effect caused by urbanization and has been studied to evaluate the thermal condition in cities worldwide. However, most previous UHI analyses are performed in major metropolitan cities. This study conducts a spatiotemporal analysis of UHI in a rapidly expanding low-density suburban center and determines how bio-productive land covers react and the extent of the disturbance to each land cover based on time series land surface temperatures extracted from Landsat 7 ETM+ images. Two methods applied and compared are the single exponential decay method, which measures UHI footprint (UHIFP) on vegetation phenology, and the two dimensional Gaussian surface, which quantifies the influence based on distance from the local urban perimeter. Three spectral indices (Normalized Difference Vegetation Index (NDVI), Moisture Index (NDMI), and the Enhanced Vegetation Index (EVI)) were extracted and the residuals from the Gaussian model were compared based on these indices in order to better understand the thermal variations of each land cover within a UHI. The results show that the UHIFP of the studied low-density suburban center is 1.4 times larger than the size of the urban center, marginally smaller than previous analyses performed within high-density metropolises. All vegetated land covers experienced their maximum cooling effects before reaching the UHIFP perimeter while urban surfaces begin to diverge from the Gaussian model outside of the UHIFP. The residuals of sparse vegetation maintained strong correlations with each index throughout the growing season while NDMI retained the strongest relationships with every land cover. This study has helped us better understand the UHI effects of small communities with

varied vegetation phonology based on the distribution of built-up pervious and impervious surfaces within the neighborhood structure. The similar results from both methods indicate a strong urban cover influence overpowering the dominant distribution of agricultural surfaces throughout the growing season.

3.2 Introduction

The urban heat island (UHI) is the product of anthropogenic processes with urbanization which modifies atmospheric and surface properties and alters the energy balance and thermal environment (Yang, Huang, and Tang 2019). It has been studied as far back as early 19th Century (Howard 1818) and is a well-explored phenomenon with urban centers of varying sizes (Oke 1973; Katsoulis and Theoharatos 1985; David R Streutker 2003; Krehbiel, Jackson, and Henebry 2016; Yao et al. 2019).

Thermal infrared (TIR) data quantified from top of atmosphere radiances in satellite imagery is used to derive land surface temperatures (LST) (Tomlinson et al. 2011). UHI research, now commonly measured globally using LST, has accelerated since 2005 with the majority of regional and seasonal focus being in China and summer daylight hours (D. Zhou et al. 2019). Using the UHI intensity measured between urban temperatures and a referenced rural region, the footprint of the UHI effect is a new index quantifying the spatial extent of the rural area affected by the UHI (Qiao et al. 2019).

Two commonly used approaches for determining the spatial influence of the UHI are the urban heat island footprint (UHIFP) and the footprint of surface urban heat island (SUHI) model developed by D. R. Streutker (2002; 2003). The UHIFP, first introduced to measure the anthropogenic effects that urbanization has upon the warming of vegetation phenology (X. Zhang et al. 2004), has been adapted to determine the distance at which the UHI effects decay towards rural areas (D. Zhou et al. 2015). The footprint model of SUHI effect uses a Gaussian planar

surface to fit the UHI effect and has been widely applied to study the UHI in many metropolitan areas (D. R. Streutker 2002; David R Streutker 2003; Martin, Baudouin, and Gachon 2015; Sobrino et al. 2012; Anniballe, Bonafoni, and Pichierri 2014; Anniballe and Bonafoni 2015; Yao et al. 2017; Qiao et al. 2019; D. Zhou et al. 2019). However, the footprints of both approaches have not been compared.

The majority of previous UHI studies using remote sensing are performed with mean annual data from daily products using coarse spatial resolution sensors such as the Moderate Resolution Imaging Spectroradiometer (MODIS) (Yao et al. 2017; Qiao et al. 2019). However, the smoothing effects with high-resolution thermal data are more appropriate for smaller scales despite having higher UHI magnitudes and spatial extents (Anniballe and Bonafoni 2015). Furthermore, the land cover products used in this analysis were also derived from Landsat which will help produce robust residual analyses based on each bio-productive surface.

The application of UHI studies in a cold and urban country such as Canada is increasingly necessary. Climate models indicate greater warming in colder regions, accelerated transformations of nitrogen oxides and volatile organic compounds into ozone, and the population's sensitivity to heat higher than 20˚C (Y. Wang, Berardi, and Akbari 2016). With most of the research focused on major metropolitan cities (Touchaei and Wang 2015; Y. Wang, Berardi, and Akbari 2016; Adamowski and Prokoph 2013), the UHI effect of low-density suburban centers, where the majority of Canadian urban growth occurs (Maoh and Kanaroglou 2007), are often not assessed individually.

This study examines the UHI effect of a low-density suburban center near the Greater Toronto Area (GTA) from 2000 to 2019 using time series images of Landsat 7 Enhanced Thematic Mapper (ETM+). By comparing the footprint produced from both models, this analysis seeks to address three main questions: 1) what is the extent of thermal disturbance of the UHI effect to each bio-productive land cover in the surrounding rural areas?, 2) are the calculated

footprints from UHIFP and SUHI consistent?, and 3) what are primary factors influencing the spatiotemporal pattern that a low-density suburban center has upon differing land covers with varying distance from the urban perimeter?

3.3 Materials

3.3.1 Study Site

The location of this study is in Milton, Ontario, Canada. It is situated within the GTA, the most populous area throughout Canada, and is surrounded by a plethora of agricultural and urban land covers, as well as some forested and wetlands. Milton's population has risen 30.5% to 110,128 between 2011 and 2016 making it the most rapidly growing community in Eastern Canada (Hennessey 2017).

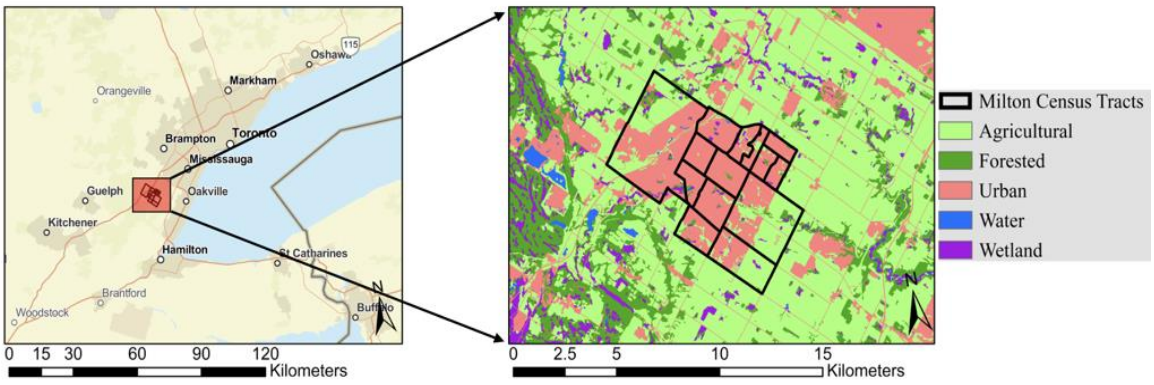

Figure 3.1: The distribution of land covers surrounding Urban Milton, its designated census tracts, and its location within the GTA in the 2015 land cover product.

Urban Milton (UM) and Rural Milton are defined based on population density due to their relatively homogenous neighborhood structures and their stability for time-series analyses (Gordon and Janzen 2013). Figure 3.1 displays in boldened polygons the appropriate census tracts representing UM for which the urban surfaces within are representative of the urban center. Gordon and Janzen (2013) defined urban census tracts as having a population density in excess of 150 people/km^2 and exurban having a low gross population density and heavy reliance upon automobiles where over half of the labor force commutes to central cities for employment. This

explains 13 of the census tracts; however, a fourteenth tract was selected due to its wide distribution of industrial urban surface components.

3.3.2 Land Cover Data

Version 3.0 of the Southern Ontario Land Resource Information System (SOLRIS) includes land cover maps in 2002, 2006, 2011, and 2016 in the Milton area with a pixel resolution as low as 15 m (Science and Research Branch of the Ministry of Natural Resources and Forestry 2019). Landsat imagery is associated with the nearest chronological land cover product (2004 imagery is analyzed with the 2006 land cover product). The SOLRIS dataset employs methodology presented by Lee et al. (1998) to optimize the implementation of the classification techniques. It presents reliable land cover products with overall accuracy of 93% based on an assessment conducted within a polygon encompassing the study area (Sampson 2007).

19 unique classes existing within close proximity to Milton were grouped into five land cover categories. Table 2.1 displays the five merged classes; water, wetlands (any surface where the water table is either seasonally or permanently at, near, or above the substrate surface), forest, agriculture (including undifferentiated land covers in reference to alternative tilled surfaces not included in the 'tilled' class, hydro fields, forest openings, and brownfields), and urban (Science and Research Branch of the Ministry of Natural Resources and Forestry 2019).

3.3.3 Remote Sensing Data Acquisition

In order to maintain data consistency, only LST data acquired solely from Landsat 7 ETM+ from 2000 to 2019 were used in this study. The ETM+ imagery has 7 main bands (along with an additional panchromatic band) with spatial resolutions ranging from 15 to 60 meters, and a 16-day temporal resolution (National Aeronautics and Space Administration 2020). The LST is extracted using the statistical mono-window algorithm (SMW) conceived by Ermida et al. (2020) from atmospherically corrected surface reflectance Landsat 7 ETM+ products in Google Earth Engine (Malakar et al. 2018). Its accuracy meets the threshold proposed by Guillevic et al. (2018)

with overall precision (in RMSE) of 1.0 K determined by Ermida et al. (2020). A 20% local cloud coverage threshold was used to select appropriate LST images for UHI analysis.

3.3.3.1 Seasonality

The annual timeframe used in this study was based around the growing season due to the complexity of environmental variables with the local climate. Soil moisture, snow cover, cloud cover, atmospheric moisture, precipitation, and anthropogenic gases are among the elements widely studied to separate the typical extremes of summer and winter measurements (Bernhardt and Carleton 2019; K. Wang et al. 2017; W. Zhou et al. 2014). Late autumn and winter data present far too many obstructions and interference caused by snow coverage. As a result, the annual calendar days included in the research consists of days 100 (April 9/10) to 290 (October 16/17). These days exhibit minimal frost and snow coverage along with increasing solar radiation and vegetated growth (Ministry of Agriculture, Food and Rural Affairs 2020). In order to differentiate the portions of the growing season for this analysis, April and May (referred to as 'Spring') are combined representing the end of frost coverage and the initial planting phase, June through August is the main summer period, and September and October (referred to as 'Autumn') represent the harvest and end of season.

3.4 Methods

3.4.1 UHIFP

UHIFP uses a single exponential decay model as the following to examine temperature trends from an urban center toward rural areas (D. Zhou et al. 2015).

$$\Delta T = A * e^{-S*D} + T_0 \quad (3.1)$$

Where ΔT represents the mean LST differences between the urban area and rural buffers, A is the maximum temperature difference using the mid-value amongst the three furthest rural

buffers, S is the mean temperature decay rate, D is the distance away from the urban center, and T_0 stands for the asymptotic value.

To determine the spatial properties of the UHI impact on rural surfaces, buffers are implemented as a factor of distance from the urban perimeter. In order to maintain a similar quantity of pixels within each buffer zone, twelve buffers surrounding the urban land cover area within UM census tracts are generated, each consisting of half the urban surface area (Zhou et al., 2015). Transportation surfaces are masked out to avoid the inclusion of roads in the rural parts of UM census tracts. Instead, a 15 m buffer around all other urban surfaces is used to regulate a centralized urban center. As this study uses four land cover products addressing Milton's growth over 20 years, a different set of buffers are generated consistently maintaining a total rural area 6 times larger than the urban center.

Previous research examined annual mean UHIFP based on daily MODIS products (X. Zhang et al. 2004; D. Zhou et al. 2015; C. Meng and Dou 2016). Due to the exchange of a 16 days revisit cycle of ETM+, a 5-years period is implemented with the central year determining the land cover product. With all 16 time periods (period 1 = 2000-2004), each set of results are inputted into the single exponential decay model.

All cloud cover pixels and elevations greater than 50 m from the highest point in UM were removed from the UHIFP model. The footprint determination is based upon the point at which each exponential model reaches 95% of their asymptotic values (X. Zhang et al. 2004). The final product represents the area surrounding UM affected by the local UHI within the proximate exurban buffers.

3.4.2 SUHI Gaussian Fit Model

The planar fit Gaussian surface was developed through the method described by D. R. Streutker (2002; 2003) to quantify the UHI as a continuously varying surface. Its purpose is to present a quick and robust technique for analyzing and parameterizing the spatial distribution of the SUHI

for quantitative inter-city comparisons or single city time scale analyses (Anniballe and Bonafoni 2015). To access the Gaussian surface, the following equation is used:

$$SUHI(x, y) = a_0 * \exp\left[- \frac{((x - x_0)\cos\varphi + (y - y_0)\sin\varphi)}{0.5a_x^2} - \frac{((y - y_0)\cos\varphi + (x - x_0)\sin\varphi)}{0.5a_y^2} \right] \quad 3.2$$

Where (x_0, y_0) represent the central location of the model's UHI, a_0 is the magnitude, (a_x, a_y) is the spatial extent, and φ is the orientation.

All cloud and water pixels must first be masked out from the LST image followed by the temporary removal of urban pixels within UM to produce datasets consisting entirely of rural pixels. After acquiring the mean rural temperature, it is then subtracted from the entire LST image to generate the SUHI Gaussian surface.

Its results produce two elliptical thresholds representing the footprint of the SUHI in each image. One ellipse determines the distance from the central location at which the temperature decreases to a fraction of the magnitude, 61% ($e^{-1/2}$) of the maximum value, and the second ellipse is a constant threshold where the SUHI planar fit surface temperature is greater than 1.0 K (Anniballe and Bonafoni 2015).

3.4.2.1 Residuals Analyses

The SUHI planar fit model does not produce thresholds that align with the shapes of either UM or the rural buffers produced for the UHIFP model. Alternatively, the Gaussian surface produces residuals which can be analyzed with the buffers and a land cover distribution map. Four analyses are made regarding the residuals' relationship with the planar surface; a ratio analysis, a buffer comparison, and a timeframe analysis.

The ratio analysis divided the quantity of positive residuals by the negative and the results with each land cover are displayed in a box-plot separated by months. Its purpose is to quantify the relationship that pixels within each land cover have with the planar fit model depending on whether the residuals are above or below the SUHI surface.

The Gaussian surface's residuals are also analyzed using the buffer areas applied to the UHIFP model. The buffer analysis helps determine the SUHI model's spatiotemporal influence and provides a spatial analysis comparable with the UHIFP. Seasonal divisions are implemented based on vegetation growth and solar radiation separating the beginning, middle, and end of the growing season. The mean seasonal distribution of residuals for land covers within each buffer is compared.

The time frames used for each distribution of land covers are incorporated into a time frames analysis. Using Google Earth Engine, mean imagery for each year associated with a SOLRIS product was calculated and compared. General UHI magnitudes, spatial extents, and Gaussian surface residuals are analyzed for each part of the growing season. Because of the nature of this analysis, a series of complications occur such as the inability to control local cloud coverage and a bias towards the few days with clear skies. These results are taken with caution and only conclusions regarding general UHI trends are made.

3.4.2.2 Vegetation Health and Moisture Correlation Analyses with Residuals

Understanding the variables affecting the residuals of each bio-productive land cover in the SUHI model is achieved through correlation analyses between the residuals and vegetation and moisture indices. The multispectral Landsat 7 bands required from each date are blue, red, near infrared (NIR), and shortwave infrared (SWIR). Amongst the vegetation indices, NDVI is more commonly used due to its cancellation of topographic, cloud cover, atmospheric, and changing sun angle effects with vegetation monitoring (Alademomi et al. 2020).

$$NDVI = \frac{(NIR - Red)}{(NIR + Red)} \quad 3.3$$

Enhanced Vegetation Index (EVI) acts as an enhancement to it with its atmospheric correction, saturation in areas with high biomass, and soil reflectance reduction abilities (Alademomi et al. 2020).

$$EVI = 2.5 * \frac{(NIR - Red)}{(NIR + 6 * Red - 7.5 * Blue + 1)} \quad 3.4$$

Normalized Difference Moisture Index (NDMI) behaves as an index to reflect the moisture content within the soil and vegetation canopy (Zhu et al. 2019).

$$NDMI = \frac{(NIR - SWIR)}{(NIR + SWIR)} \quad 3.5$$

The comparisons made with vegetation indices use Landsat 7 ETM+ Surface Reflectance Tier 1 products on the same dates as the LST acquisition. A cloud mask was installed, the residuals' pixels were converted to points, and all values from each vegetation/moisture index were extracted to the nearest point. The correlation coefficient is calculated with a range of 1.0 (positive correlation) to -1.0 (negative correlation).

3.5 Results and Discussion

3.5.1 UHIFP

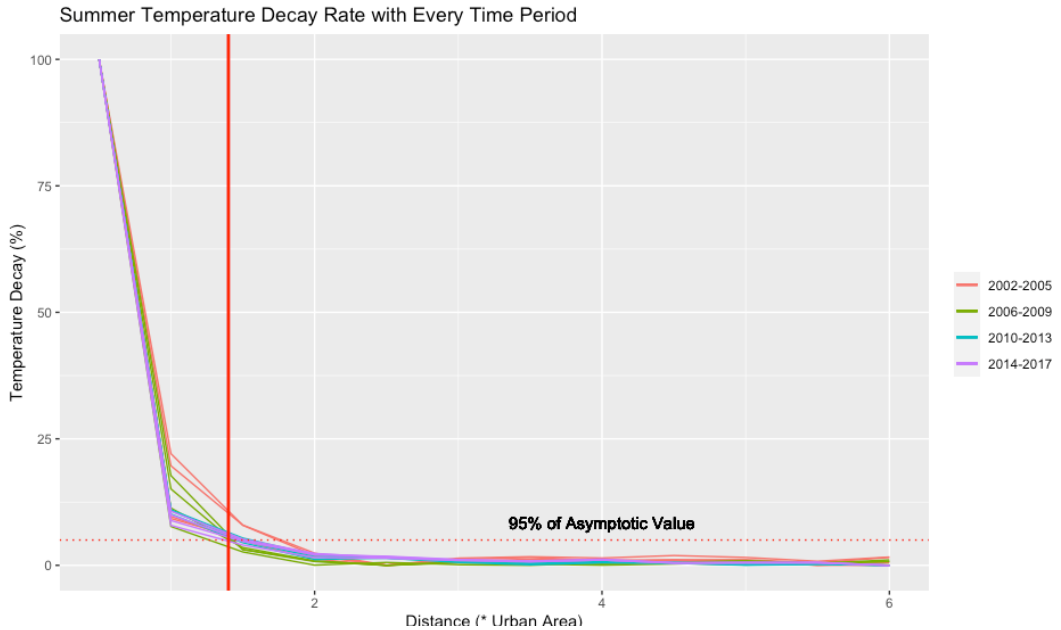

Figure 3.2: The determined size of the UHIFP, where the temperature declines to 95% of the asymptotic value, is 1.4 times the urban area of Milton based on an overall average.

The results from the UHIFP are determined based on the distance at which the exponential model reaches 95% of its asymptotic value. For Milton during the growing season, the mean UHIFP is achieved at 1.4 times the urban area (Figure 3.2). As a result, the first three buffers are

representative of the area within the local average UHIFP. The strongest outliers were the first two time frames (2000-2004 and 2001-2005) with marginally increased footprints (1.8 times the size of the urban center).

The size of the UHIFP within each set of mean sampled imagery was consistent after the first two time frames. The results experienced in Milton are much smaller than the conclusions drawn by X. Zhang et al. (2004), which were 2.4 times the area of an urban center in eastern North America. Such results are related to the local conditions influencing the UHIFP analysis, such as population density, city size, proximity to a larger urban center, and the surrounding vegetation distribution.

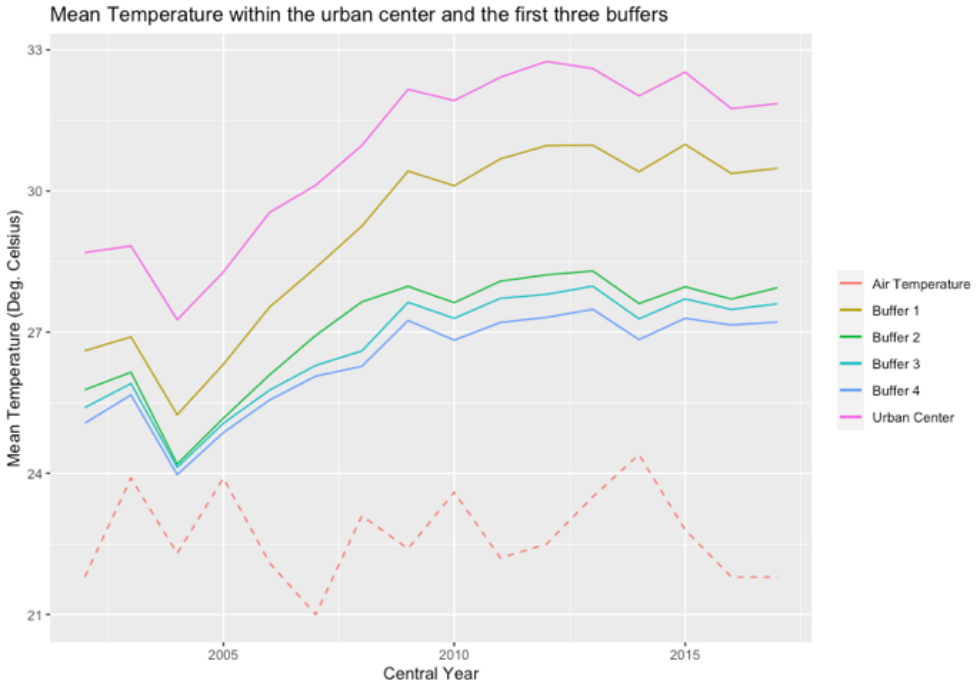

Figure 3.3: The mean LST collected within each time period within the urban center and the first four buffers. Daily air temperature data from the nearest station to Milton, in Georgetown, is applied to separate the local UHI effects from regional climate change.

Figure 3.3 presents the mean LST within the urban center and the adjacent rural area 2 times the urban center's size (first four buffers). The temperature difference between the urban center and the first buffer exhibits minimal change while an increasing difference is evident

between the first and second buffers after 2005. Following the second buffer, the mean temperature differences amongst buffer regions remain consistently small while most UHI effects have decayed. The data in Figure 3.3 presents mean LST increasing at a higher rate within the urban center and the first buffer than the following buffers. As a result, the UHIFP of the very small low-density community, prior to its expansion, is larger relative to the urban center's area.

The proportion of each land cover within the local UHIFP compared to its distribution throughout the area 6 times the size of UM can help determine the urban center's impact on each type of surface. The portion of forested surfaces within the footprint was between 11% and 14% of its total. Wetlands and agricultural land covers contain slightly higher proportions within the UHIFP (19% - 22% and 24% - 27% respectfully). The majority of urban surfaces were contained within the footprint (between 65% and 73%); however, exclusive of the urban center, only between 18% and 27% of the rural urban surfaces were located inside the footprint.

3.5.1.1 UHIFP Size Discussion

The population arrangement and overall size of an urban center are foundational in determining the footprint of a UHI. Population density can have a major effect on temperature differences within a city as it grows (Ramírez-Aguilar and Lucas Souza 2019). An increased distribution of impervious surfaces, coinciding with rising human activity frequency, contribute to the growing intensity of a UHI (F. Meng and Liu 2013). In comparison with previous studies applied to larger municipalities with denser population distributions, Milton's suburban stature is incapable of reproducing the increasing trends of sensible heat flux experienced in larger cities with less vegetated surfaces.

The proximity to much larger urban centers heavily affects the determination of the local UHIFP. All of the surrounding UHI footprints influence the referenced rural temperatures used for Milton's analysis. For example, the first two time periods (2000-2004 and 2001-2005) determined larger footprints due to Milton's smaller urban size and a reduced external influence

from neighbouring UHI footprints. Milton's growth coincides with neighbouring communities' development and their influence on rural temperatures. As a result, an inevitable discrepancy is found between urban and rural temperatures in a suburban setting compared with a larger metropolis, being the primary influence on rural temperatures.

3.5.1.2 Vegetation Distribution within the UHIFP

The vegetation distribution surrounding Milton is another major variable on its ecological impact upon the surrounding temperatures. While urban areas surrounding forested or highly vegetated areas produce a greater discrepancy in UHI, partly due to residential energy consumption for cooling during the summer (Imhoff et al. 2010), Milton's rural land covers consist largely of sparse vegetation. The Niagara Escarpment, a large nearby forested area, was omitted from the rural UHIFP due to the impact of elevation. Additionally, being an inland town with limited open water and wetlands surfaces in close proximity may result in lower evapotranspiration comparisons between urban and rural (D. Zhou et al. 2015; Li, Zhang, and Kainz 2012). As a result, urban centers lacking nearby dense vegetation may experience reduced UHIFP sizes.

The diminutive proportion of the study area's dense vegetation located within the UHIFP, as opposed to its distribution in the outer buffers, can have a major influence on the UHI effect on rural LST. Its cooling effects and spatial distribution have the ability to reduce the footprint encroachment on rural vegetation. Additionally, as the UHIFP contains a quarter of the local agricultural surfaces and the majority of urban surfaces, the spatial variability of vegetated land covers, and concentration of impervious surfaces, is a major contributor to a smaller footprint size.

3.5.1.3 UHIFP Limitations

The limitations within this study for calculating the UHIFP with Landsat 7 ETM+ consists of an optimistic 16 days revisit cycle, only one time of day where imagery acquisition is possible, and the distribution of snow and ice surfaces in the winter. Previous research (D. Zhou et al. 2015)

utilized MODIS products due to their near daily data availability, possibility for comparing daytime and nighttime data, and much larger metropolitan sizes. In comparison, Milton's urban area is dwarfed by the far larger North American and Chinese cities. The resulting 5 years periods applied to determine mean pixel values for a UHIFP is unable to reproduce daily samples possible with MODIS analyses; however, this study's results were consistent with every period. Until a satellite is launched with similar spatial resolutions as Landsat and a major reduction in its revisit cycle, applying a 5 years average may presently be the optimal solution as uniform results were found within each 5 years period. With winter conditions, the model remains sufficient provided the urban area is a large enough size.

3.5.2 SUHI Model

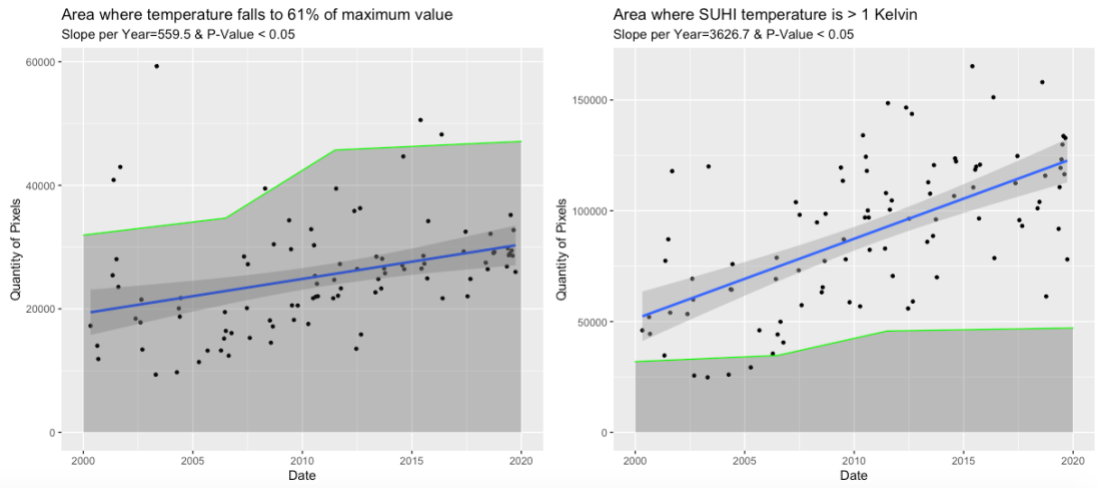

Figure 3.4: The size of both SUHI thresholds from each acquired image. The total quantity of urban pixels within Urban Milton (green) and the line of regression (blue) are presented to compare planar surface SUHI threshold results with actual urban area.

The SUHI model was generated from a limited quantity of image acquisition dates due to a coarse temporal resolution and cloud interference. From the available results, the SUHI magnitude observes a rising trend (0.16 K/year). From Figure 3.4, it can be seen that the area with 1.0 K UHI threshold is increasing at a much more dramatic rate of 3626.7 pixels/year compared with the $e^{-1/2}$ UHI threshold (a slope of 559.5 pixels/year).

The surface thresholds indicated rising trends, and in the case of the 1.0 K temperature ellipse (Figure 3.4), greatly surpassing the area of UM. The rate at which the thresholds grow appears to align with the rate of expansion of the built-up environment. Based on the distribution and quantity of urban pixels within UM for each land cover product, the timeframe between 2006 and 2011 is when UM experienced its greatest degree of urban development. The declining vegetated surfaces along with increasing impervious surface, anthropogenic gases, and population densities are all highly correlated with higher surface temperature, especially during the urbanization process (Lu et al. 2015; Yu et al. 2019). The development of new built-up environments result in increased volume of ozone, faster pollutant production lofted to higher altitudes, and greater transport of the adverse effects on air quality (D. L. Zhang et al. 2011). Further evidence of these effects are displayed in the Table 3.1 time frames comparison where the most dramatic changes in magnitude occurs between 2004-2008 and 2009-2013 (with the exception of autumn where observations were in minimal supply).

Time series results incurred from the overall SUHI data, along with the time frames analysis with residuals data, must be taken with speculation due to the insufficient temporal resolution of the Landsat 7 ETM+ sensors. In order to accurately determine the SUHI effects, a spatial resolution similar to Landsat is required along with a 2 days revisit cycle and the overpass time immediately before sunrise (Sobrino et al. 2012). There are currently no spaceborne thermal sensors which satisfy these requirements. The available products from Landsat 7 meet the spatial resolution requirements; however they are heavily unqualified for the temporal obligation. Although trends are noticeable, conclusions based on magnitudes are incapable of being drawn due to insufficiencies with the products.

3.5.2.1 Residuals Ratio Analysis

Figure 3.5 lists the ratio between quantities of positive and negative residuals in each month for each land cover type. The results from the ratio analysis indicate the distinctive impact of urban cool islands within the forested and wetlands surfaces surrounding UM. April and May data describe residual cooling behavior less intense than in the summer and early autumn.

The most interesting results in this analysis are within the agricultural and urban surfaces. The agricultural residuals, being the dominant land cover throughout the study site, follows the Gaussian planar surface closely with only a marginally greater quantity of negative residuals. Spring and Autumn months exhibit results which better align with the SUHI model as opposed to summer months where a much more definitive distribution of negative residuals exist. The cooling effects climax in August with the average ratio being 0.72, as seen in Figure 3.5. The urban results contrast vegetated surfaces where positive residuals consistently outnumber negative residuals. As summer progresses, the distribution of positive residuals grows to an August peak.

It is well established that vegetated land covers behave as cooling zones within a UHI (Oke 1979; Sun, Wu, and Tan 2012; Li, Zhang, and Kainz 2012; Skelhorn, Levermore, and Lindley 2016; Q. Huang et al. 2019; Alademomi et al. 2020). The ratio analysis results in Figure 3.5 further exemplify that notion with only the urban land cover category obtaining a greater ratio of positive residuals compared to negative residuals. As summer progresses and thermal emissivity and capacity on impervious surfaces increases, the divergence urban land covers' residuals have compared to the vegetated covers increases (H. Huang et al. 2019). The cooling effects from vegetated land due to evapotranspiration are largely removed when replaced with impervious materials (Oke 1979). The result is a surface with a heavily limited ability for evapotranspiration, and cooling properties, culminating in a warmer surface temperature compared to vegetation.

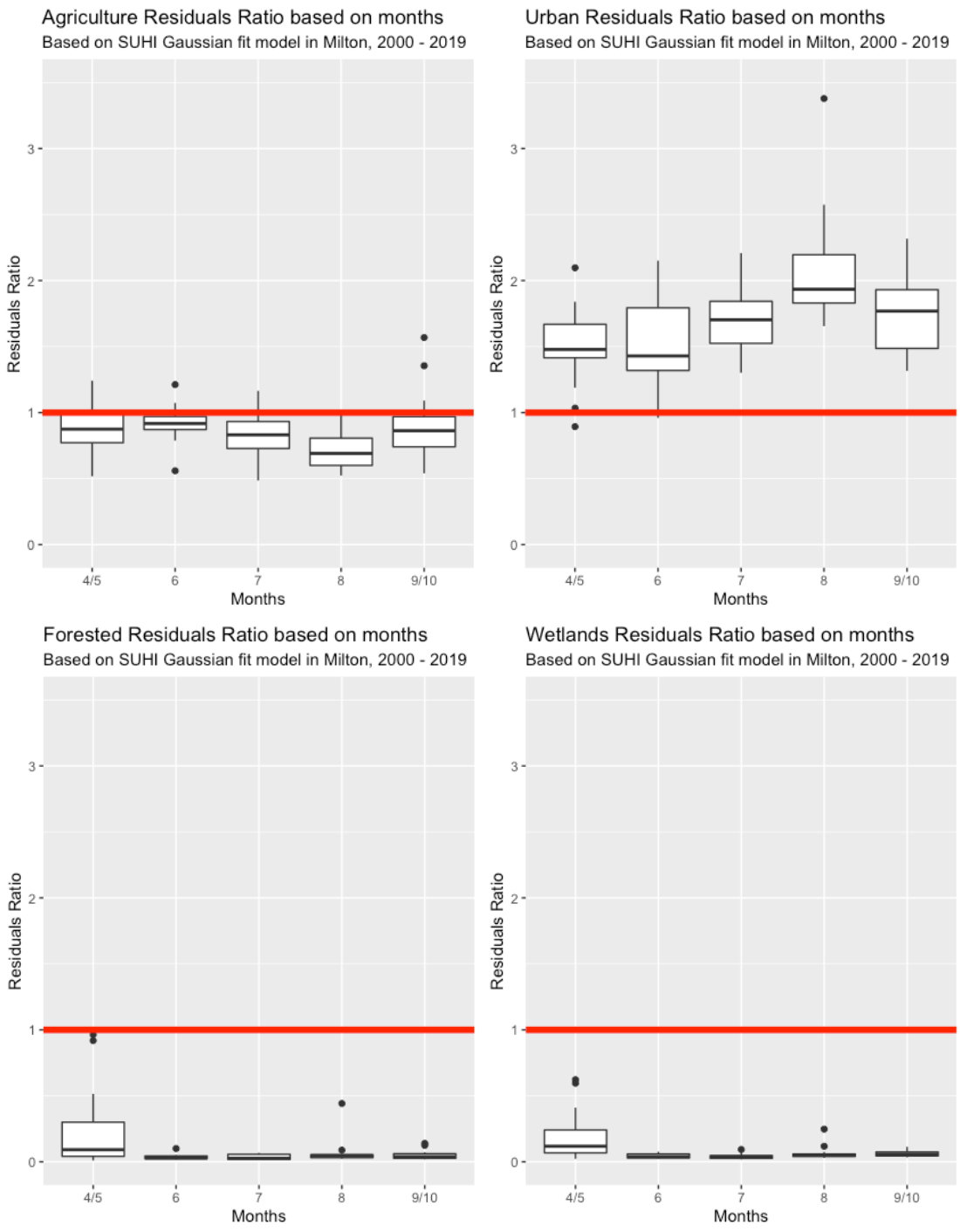

Figure 3.5: The residuals ratio for each land cover determined by dividing the number of positive residuals by negative residuals within each captured Landsat 7 ETM+ product.

The crop surfaces in spring months (April and May) along with the autumn months of September and October (to a lesser degree) exhibit a reduction in its cooling abilities within the UHI. With the possibility of frost as late as May and cultivation occurring in September, the agricultural results in Figure 3.5 display considerable distributions of bare earth at the beginning and end of the growing season. The summer months of July and August, when sparse vegetation growth achieves its peak performance, provide its greatest ability of cooling below the SUHI surface.

Pixels within the other two land cover categories observed a much larger ratio of negative residuals throughout the growing season, especially in summer and autumn. Forests and wetlands, which usually have low LST due to its dense vegetation compared to crop lands which contain more sparse vegetation along with bare soil, are known to behave as cool areas within a UHI (Sun, Wu, and Tan 2012). In the spring, forested land covers deviated the least of any season (-0.27˚C compared to -0.54˚C in the summer) from the UHI temperature mean in Wuhan, China from 2005 to 2015 (Q. Huang et al. 2019). The densely vegetated land covers surrounding Milton behave in a similar manner with its most effective cooling abilities occurring after spring.

3.5.2.2 Residuals Buffer Analysis

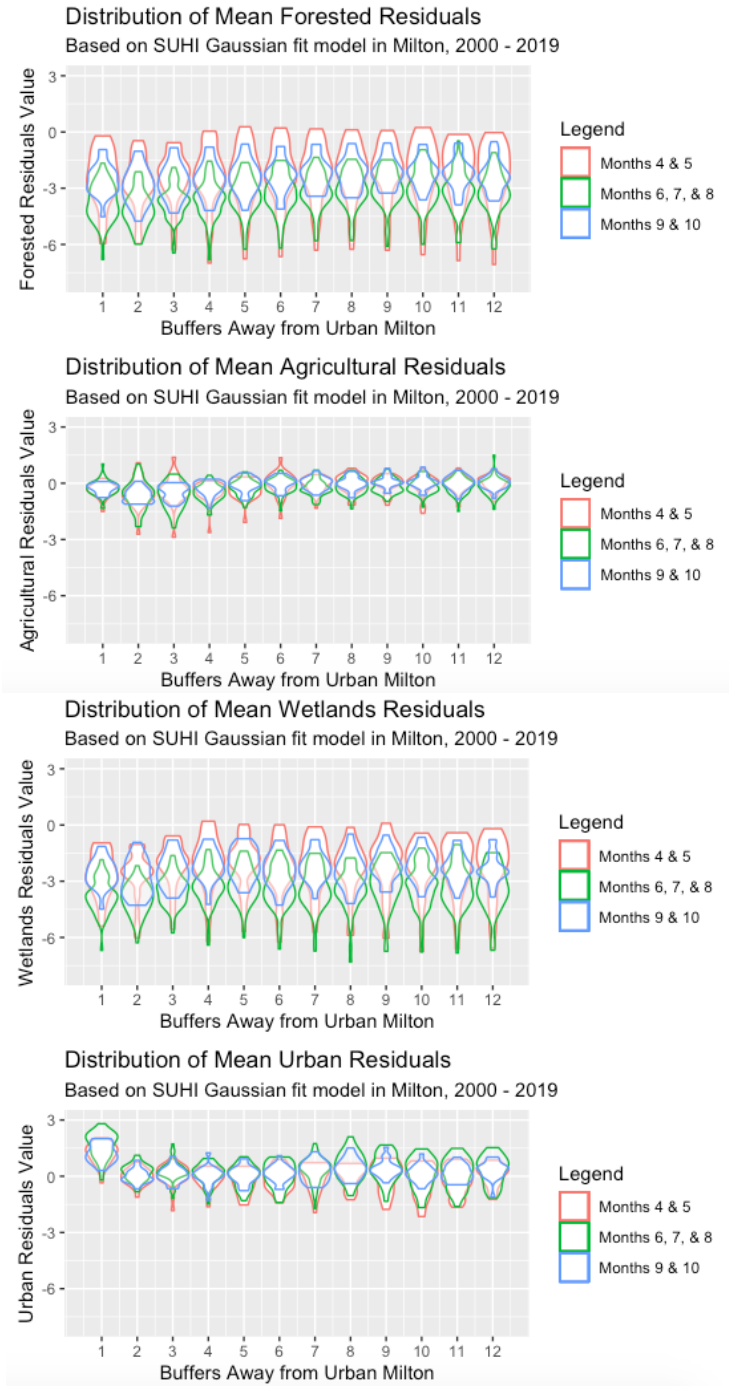

Figure 3.6: Density plot of the results from the buffers analysis with the residuals of each land cover within the SUHI models.

Figure 3.6 shows the density of mean SUHI residual values for each land cover within the buffer regions. The buffer analysis indicates the spatial distribution of residuals from each SUHI image as distance increases from the urban center perimeter. Applying the results from the UHIFP (rural

area 1.4 times the size of the urban area), the first three buffers are within the local footprint of the UHI.

Seasonality plays a major role in determining the cooling and warming abilities within a UHI with dense vegetation and urban lands. Summer is when impervious surfaces are warmest and deviate most from the Gaussian surface. Forests and wetlands, in contrast, provide their greatest cooling effect during summer and deviate most while moderately reducing its cooling abilities in autumn. Agriculture exhibits minimal seasonal effects within Milton's UHI.

The buffer analysis with both forested and wetlands pixels determined a cooling effect which is much more evident within the first three buffers and in the main summer months. Throughout the year, the spatial influence which densely vegetated surfaces have on the UHI in Milton are most intense within the surrounding area 1.5 times the size of the urban center (first 3 buffers), the rural area within the UHIFP. They remain definitive urban cool zones throughout the dataset with the highest mean residual value (-2.02 K) existing within the wetlands category at the fourth buffer zone during Spring. While green spaces within urban environments are known for the ability to improve local air quality, assist in the reduction of energy required for cooling, and optimize the natural ecological system (Ozyavuz 2012), the dense vegetation is most intense within the UHIFP.

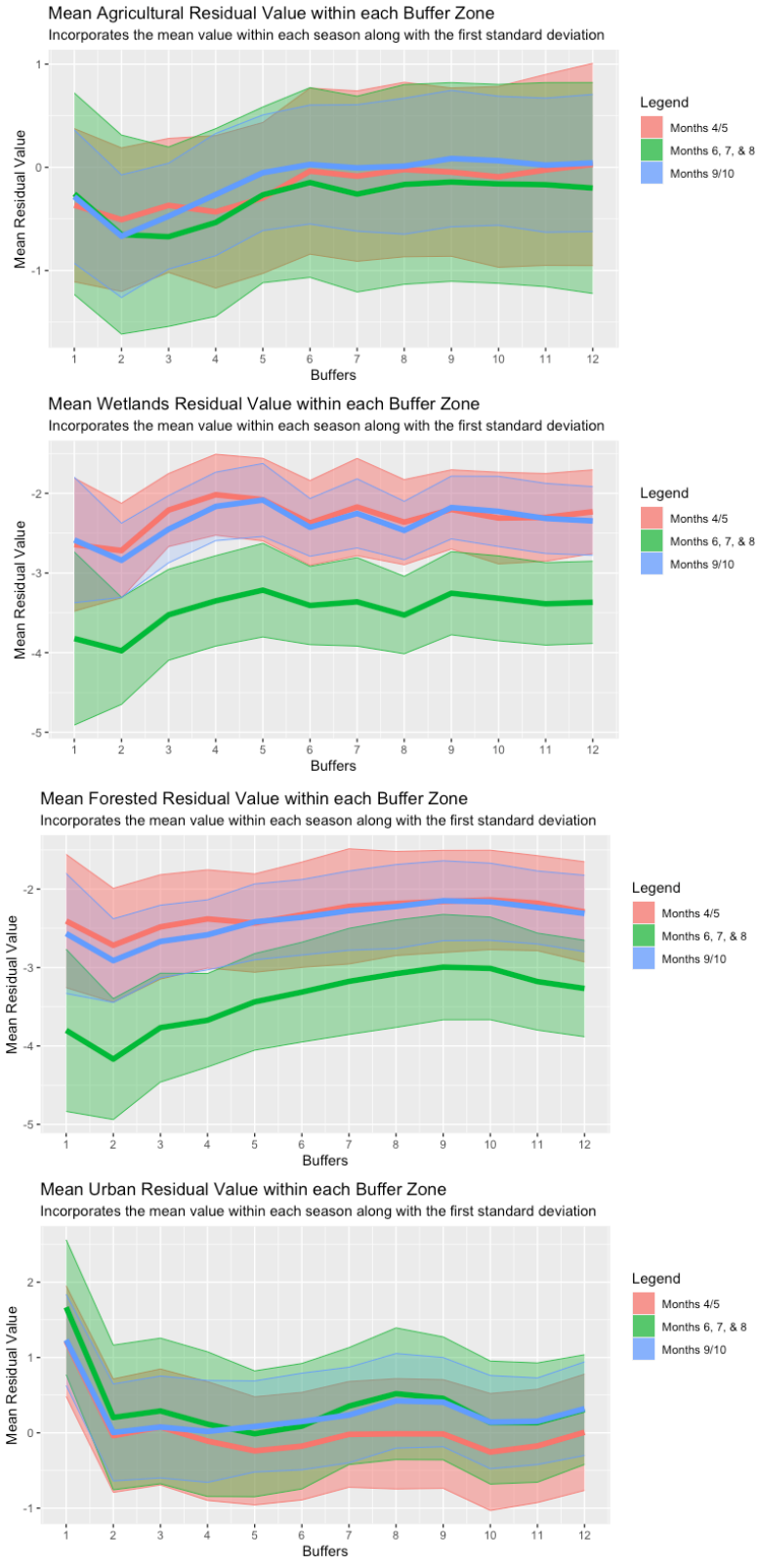

Figure 3.7: The mean and first standard deviation residual value of each land cover within each season for each buffer away from the central urban perimeter.

Agricultural land covers convey similar observations to the more densely vegetated pixels. Their respective cooling effects are limited to the first five buffers within every season and maximized within the first three (the area within the UHIFP). The mean residual values ranged between -0.67 K and -0.26 K within the first 5 (4 for autumn) buffers away from the urban center before stabilizing with the Gaussian surface. Being the dominant land cover of the region, the distribution is more likely to contribute to the SUHI planar fit and produce residuals closest to zero, especially during the time before planting and after cultivation where its consistency is largely bare soil. The summer months contributed slightly more cooling as a result of its peak vegetated state (Figure 3.7), especially within the outer buffers.

The reaction within the first buffer zone for the urban land covers' residuals is due to this paper's methods of obtaining an urban perimeter. The urban center was calculated excluding transportation within UM census tracts and joined with a 15 m buffer to replace the missing roadways and obtain a centralized urban center. As a result, heavy traffic located on the major 401 highway along with the immediate outer roads are the main contributors to the first buffer's urban distribution.

Urban results provide the highest LST and, aside from Spring, reliably positive residuals. For the remaining buffers, the average urban residuals conform closely to the Gaussian planar fit until the final 6 buffers away from the urban center where its positivity increases (especially during the summer and autumn months). The area located outside of Milton's UHIFP (buffers 4 – 12) is representative of where the ecological footprint that Milton has on its surrounding rural vegetation has decayed (X. Zhang et al. 2004). The positive residual values that urban pixels experience outside of the UHIFP indicates a localized warming divergence from the Gaussian surface, which has decayed.

3.5.2.3 Time Frames Analysis

Mean LST for each time frame as each of the land cover datasets were used to determine general trends. Table 3.1 presents the SUHI magnitude, model thresholds, and the total quantity of available images within the region for each section of the growing season.

Results with SUHI magnitudes, thresholds, and measures of fit experience growth between the first and last time frame. An apparent rising SUHI magnitude is displayed within the first three time frames during the spring (3.93 K to 6.67 K) and summer (6.55 K to 8.09 K) of Table 3.1 before exhibiting a slight UHI magnitude reduction in the final time frame. The areas within each SUHI threshold experiences growth, especially in the final three time frames of each season.

Significant portions of the results do not indicate rising trends. The autumn months, with their limited quantities of clear sky pixels, provides uncharacteristically the largest thresholds within its first time frame. Fluctuations are also evident in the autumn's magnitudes throughout the research period.

Table 3.1: The results from the time frames analysis which incorporated acquiring averaged imagery from each time period. It should be noted that the quantity of possible observations is attributed to the number of products available within each tile, thus not every observation is incorporated into the area of the study area.

	2000-2003	**2004-2008**	**2009-2013**	**2014-2019**
Months 4/5 Magnitude (k)	3.93	4.78	6.67	5.14
Months 4/5 Thresholds (Pixels) [$e^{-1/2}$ / 1.0 K]	15,028 / 41,151	15,876 / 49,658	21,656 / 82,202	32,789 / 107,341
Months 4/5 Available Images	11	11	11	15
Months 6/7/8 Magnitude (K)	6.55	6.92	8.09	7.81
Months 6/7/8 Thresholds (Pixels) [$e^{-1/2}$ / 1.0 K]	17,600 / 66,158	17,043 / 65,902	17,761 / 78,457	28,505 / 117,164
Months 6/7/8 Available Images	16	22	22	26
Months 9/10 Magnitude (K)	3.48	5.11	4.09	5.74
Months 9/10 Thresholds (Pixels) [$e^{-1/2}$ / 1.0 K]	48,299 / 120,381	14,393 / 46,960	25,610 / 72,078	29,394 / 102,721
Months 9/10 Available Images	8	9	10	12

The acquisition of mean LST data within each time frame presents complications with the results. A limited quantity of observations are available within each section of the growing season (16 to 26 available images for the summer months compared to 8 to 12 for the autumn months). The insufficiencies with the data results in bias and influence from outliers. With those considerations, even the period with the greatest potential quantity of observations (summer 2014-2019 has 26 observations) remains insufficient for decisive conclusions.

3.5.2.4 Vegetation and Moisture Index Correlations

The results from the correlation analysis between the SUHI model's residuals and the moisture index (Figure 3.8) provide the most consistently positive correlation results with all land cover categories. Wetlands and agriculture provided the strongest relationships throughout the growing season along with significantly positive results with urban pixels in the summer. In spring months, the strongest correlation occurs in the wetlands (0.52) while the weakest ones appears in urban land (0.31). Summer has agriculture being the strongest (0.74) with urban surfaces being second strongest (0.56). In autumn, agriculture and wetlands have stronger relationships (0.62 and 0.58 respectfully) and urban surfaces were the weakest again with moderate results (0.45).

Table 3.2: The results from a correlation analysis with each of the indices. The summary statistics are similar to Figure 3.8 with only the inclusion of mean values from each season.

	Agricultural	**Forested**	**Wetlands**	**Urban**
EVI (Months 4/5)	0.36	0.42	0.44	0.19
EVI (Months 6-8)	0.40	0.38	0.41	0.28
EVI (Months 9/10)	0.27	0.27	0.30	0.18
NDVI (Months 4/5)	0.39	0.36	0.37	0.29
NDVI (Months 6-8)	0.67	0.42	0.46	0.49
NDVI (Months 9/10)	0.53	0.39	0.47	0.40
NDMI (Months 4/5)	0.47	0.44	0.52	0.31
NDMI (Months 6-8)	0.74	0.51	0.54	0.56
NDMI (Months 9/10)	0.62	0.50	0.58	0.45

Figure 3.8: The correlation coefficient each land cover's residuals have with the NDMI product with the same Landsat 7 product. This comparison was determined to have the strongest correlation with the residuals of every land cover.

The results with EVI (Table 3.2) indicate stronger relationships with dense vegetation in the early growing season. Average wetlands and forested results in the spring are 0.44 and 0.42 respectfully compared to 0.36 in agriculture. The mean correlation coefficients for the remainder of the growing season are similar with all three vegetated surfaces (between 0.38 and 0.41 in the summer and 0.27 to 0.30 in the autumn). Urban pixels experienced their weakest correlations with this vegetation index.

The results with NDVI (Table 3.2) describe a strong relationship with agriculture while moderately weaker with dense vegetation and low-density urban surfaces in the summer and autumn months. Sparse vegetation experienced similar correlations to NDVI as dense vegetation in the spring months (mean values between 0.36 and 0.39) before providing significantly stronger results throughout the remainder of the year (0.67 for the summer and 0.53 in autumn). Urban pixels, alternatively, had weak relationships in the early growing season before providing similar results to dense vegetation in the summer and autumn.

Moisture was consistently the strongest variable affecting the SUHI residuals over every land cover. NDMI is considered as a cooling index useful for regulating thermal configuration with strong greening properties (Zhu et al. 2019). With a consistent moisture distribution throughout the study area, NDMI is capable of retaining a strong correlation with every bio-productive land cover throughout every season. Amongst all indices, its correlation with urban pixels was the strongest due to Milton's low-density residential distribution. Built-up pervious land in the form of lawns, parks, and recreational areas increase abilities for moisture retention.

The land cover which obtained the weakest correlation results with both vegetation indices was urban. This is due to the distribution of impervious surfaces, contrasting vegetation land covers and their abilities to retain moisture and reflect more infrared radiation, which are important in all three indices. The inclusion of built-up pervious land covers (in reference to urban recreation areas, such as golf courses or playing fields (Science and Research Branch of the

Ministry of Natural Resources and Forestry 2019)) may be the primary contributor to the positive correlations. Additionally, the low-density structure of the residential neighbourhoods allow for a reduced distribution of impervious surfaces and increased abilities for infrared reflection, sparse vegetation distribution, and moisture retention. As a result, as noted in Table 3.2, urban surfaces correlate relatively well with NDVI in summer and autumn.

Agricultural surfaces dominated the correlations with NDVI and NDMI with mean correlation coefficients as high as 0.64 and 0.74 within the summer months respectfully. With EVI, the forested and wetlands surfaces obtained a marginally higher correlation, with April and May results deviating the most in Table 3.2. Considering that LST generally trends in contrast to NDVI and EVI (Alademomi et al. 2020), the stronger correlation with EVI is due to the denser vegetation and reduced soil reflectance while agriculture is distributed more dominantly and performs better with NDVI.

3.6 Conclusion

The two common methods for analyzing the footprint of a UHI was adapted for a rapidly urbanizing low-density urban area in Canada using LST acquired from Landsat 7 ETM+. Both UHIFP and SUHI models were used for a comparison analysis and to determine the primary factors influencing the results. These techniques allowed for an enhanced comprehension of the effects that the local UHI has upon rural (or exurban) vegetation within differing bio-productive land covers with varying degrees of distance applied.

Milton, a secondary (or suburban) city, was determined to have an average rural UHIFP 1.4 times the size of the urban center. It is smaller than previous research due to the study site's dwarfed size compared to previous studies, reduced population density, its proximity to larger urban centers at its periphery which influence the rural reference LST, and the rural vegetation distribution. Additionally, the use of 5 years mean imagery for Landsat 7 ETM+ provided an effective and consistent method for calculating the UHIFP with a 16-days temporal resolution.

Despite agricultural surfaces being the most dominantly distributed throughout the region, urban land covers dominated influencing the UHIFP and SUHI models. It mainly followed the SUHI Gaussian surface and exhibited increased warming effects outside of the UHIFP. Agricultural surfaces achieved their greatest cooling effects in the area 2.5 times the urban center's area. Alternatively, densely vegetated land covers maximized their cooling abilities within the rural area 1.5 times the size of the urban center.

NDMI provided the strongest correlations with every land cover throughout every part of the growing season. As a result, moisture may be more important to the spatial pattern of the UHI and its footprint than vegetation health.

The results from this analysis describe the impact which small scale urban expansion poses for surrounding rural environments. The plethora of proximate agricultural surfaces and distribution of dense vegetation presents Milton's surroundings as an ideal representation for suburban communities across Canada and abroad. Conclusions made here are very useful for city planners, engineers, and geographers in their abilities to predict the impact of low-density urban expansion and its spatiotemporal influence. The strong correlations urban residuals found with NDMI and NDVI defines how the increased vegetation distributions in low-density neighborhoods and urban centers influences the local UHI and rural vegetation.

3.7 Acknowledgements

The authors are grateful for Dr. Stefania Bonafoni and Roberta Anniballe's contribution of the MATLAB script for determining the SUHI Gaussian planar fit model based on their previous research.

3.8 References

Adamowski, Jan, and Andreas Prokoph. 2013. "Assessing the Impacts of the Urban Heat Island Effect on Streamflow Patterns in Ottawa, Canada." Journal of Hydrology 496 (July): 225–37. https://doi.org/10.1016/j.jhydrol.2013.05.032.

Alademomi, Alfred S., Chukwuma J. Okolie, Olagoke E. Daramola, Raphael O. Agboola, and Tosin J. Salami. 2020. “Assessing the Relationship of LST, NDVI and EVI with Land Cover Changes in the Lagos Lagoon Environment.” Quaestiones Geographicae 39 (3): 87–109. https://doi.org/10.2478/quageo-2020-0025.

Anniballe, Roberta, and Stefania Bonafoni. 2015. “A Stable Gaussian Fitting Procedure for the Parameterization of Remote Sensed Thermal Images.” Algorithms 8 (2): 82–91. https://doi.org/10.3390/a8020082.

Anniballe, Roberta, Stefania Bonafoni, and Manuele Pichierri. 2014. “Spatial and Temporal Trends of the Surface and Air Heat Island over Milan Using MODIS Data.” Remote Sensing of Environment 150 (July): 163–71. https://doi.org/10.1016/j.rse.2014.05.005.

Bernhardt, Jase, and Andrew M. Carleton. 2019. “Comparing Daily Temperature Averaging Methods: The Role of Surface and Atmosphere Variables in Determining Spatial and Seasonal Variability.” Theoretical & Applied Climatology 136 (1/2): 499–512. https://doi.org/10.1007/s00704-018-2504-7.

Ermida, Sofia L., Patricia Soares, Vasco Mantas, Frank-M. Gottsche, and Isabel F. Trigo. 2020. “Google Earth Engine Open-Source Code for Land Surface Temperature Estimation from the Landsat Series.” Journal of Remote Sensing 12 (9). https://doi.org/10.3390/rs12091471.

Gordon, David L. A., and Mark Janzen. 2013. “Suburban Nation? Estimating the Size of Canada’s Suburban Population.” Journal of Architectural and Planning Research 30 (3).

Guillevic, Pierre, Frank Gottsche, Jaime Nickeson, Glynn Hulley, Darren Ghent, Yunyue Yu, Isabel Trigo, et al. 2018. “Land Surface Temperature Product Validation Best Practice Protocol.” Version 1.1. https://lpvs.gsfc.nasa.gov/PDF/CEOS_LST_PROTOCOL_Feb2018_v1.1.0_light.pdf.

Hennessey, Melanie. 2017. “Census: Milton Remains in Top 10 Fastest-Growing Canadian Communities.” Inside Halton, February 8, 2017, sec. Milton Canadian Champion. https://www.insidehalton.com/news-story/7110264-census-milton-remains-in-top-10-fastest-growing-canadian-communities/.

Howard, Luke. 1818. The Climate of London: Deduced from Meteorological Observations, Made at Different Places in the Neighbourhood of the Metropolis. W. Phillips, George Yard, Lombard Street, sold also by J. and A. Arch, Cornhill; Baldwin, Cradock, and Joy, and W. Bent, Paternoster Row; and J. Hatchard, Picadilly.

Huang, Huanchun, Yingxia Yun, Hao Xu, and Ting Liu. 2019. “Influence of the Mega-Urban Heat Island on Spatial Transfer of Summer Thermal Comfort: Evidence from Tianjin, China.” Tehnicki Vjesnik - Technical Gazette 26 (1): 183–93. https://doi.org/10.17559/TV-20181108143831.

Huang, Qiuping, Jiejun Huang, Xining Yang, Chuanglin Fang, and Youjia Liang. 2019. “Quantifying the Seasonal Contribution of Coupling Urban Land Use Types on Urban Heat Island Using Land Contribution Index: A Case Study in Wuhan, China.” Sustainable Cities and Society 44 (January): 666–75. https://doi.org/10.1016/j.scs.2018.10.016.

Imhoff, Marc L., Ping Zhang, Robert E. Wolfe, and Lahouari Bounoua. 2010. “Remote Sensing of the Urban Heat Island Effect across Biomes in the Continental USA.” Remote Sensing of Environment 114 (3): 504–13. https://doi.org/10.1016/j.rse.2009.10.008.

Katsoulis, B. D., and G. A. Theoharatos. 1985. “Indications of the Urban Heat Island in Athens, Greece.” Journal of Climate and Applied Meteorology 24 (12): 1296–1302.

Krehbiel, Cole P., Trisha Jackson, and Geoffrey M. Henebry. 2016. “Web-Enabled Landsat Data Time Series for Monitoring Urban Heat Island Impacts on Land Surface Phenology.” IEEE

Journal of Selected Topics in Applied Earth Observations and Remote Sensing 9 (5): 2043–50. https://doi.org/10.1109/JSTARS.2015.2496951.

Lee, Harold, Wasyf Bakowsky, John Riley, Jane Bowles, Michael Puddister, Peter Uhlig, and Sean McMurray. 1998. “Ecological Land Classification for Southern Ontario.” SCSS Field Guide FG-02. North Bay: Ontario Ministry of Natural Resources.

Li, Ying-ying, Hao Zhang, and Wolfgang Kainz. 2012. “Monitoring Patterns of Urban Heat Islands of the Fast-Growing Shanghai Metropolis, China: Using Time-Series of Landsat TM/ETM+ Data.” International Journal of Applied Earth Observation and Geoinformation 19 (October): 127–38. https://doi.org/10.1016/j.jag.2012.05.001.

Lu, Dongmei, Kaishan Song, Shuying Zang, Mingming Jia, Jia Du, and Chunying Ren. 2015. “The Effect of Urban Expansion on Urban Surface Temperature in Shenyang, China: An Analysis with Landsat Imagery.” Environmental Modeling & Assessment 20 (3): 197–210. https://doi.org/10.1007/s10666-014-9426-2.

Malakar, Nabin K., Glynn C. Hulley, Simon J. Hook, Kelly Laraby, Monica Cook, and John R. Schott. 2018. “An Operational Land Surface Temperature Product for Landsat Thermal Data: Methodology and Validation.” IEEE Transactions on Geoscience and Remote Sensing 56 (10): 5717–35. https://doi.org/10.1109/TGRS.2018.2824828.

Maoh, Hanna, and Pavlos Kanaroglou. 2007. “Geographic Clustering of Firms and Urban Form: A Multivariate Analysis.” Journal of Geographical Systems 9 (1): 29–52. http://dx.doi.org.proxy.queensu.ca/10.1007/s10109-006-0029-6.

Martin, Philippe, Yves Baudouin, and Philippe Gachon. 2015. “An Alternative Method to Characterize the Surface Urban Heat Island.” International Journal of Biometeorology 59 (7): 849–61. https://doi.org/10.1007/s00484-014-0902-9.

Meng, Chunlei, and Youjun Dou. 2016. “Quantifying the Anthropogenic Footprint in Eastern China.” Scientific Reports 6 (1): 24337. https://doi.org/10.1038/srep24337.

Meng, F., and M. Liu. 2013. “Remote-Sensing Image-Based Analysis of the Patterns of Urban Heat Islands in Rapidly Urbanizing Jinan, China.” International Journal of Remote Sensing 34 (24): 8838–53. https://doi.org/10.1080/01431161.2013.853895.

Ministry of Agriculture, Food and Rural Affairs. 2020. “Climate Zones and Planting Dates for Vegetables in Ontario.” Government of Ontario. August 7, 2020. http://www.omafra.gov.on.ca/english/crops/facts/climzoneveg.htm.

National Aeronautics and Space Administration. 2020. “Landsat 7 Science Data Users Handbook.” NASA. https://landsat.gsfc.nasa.gov/wp-content/uploads/2016/08/Landsat7_Handbook.pdf.

Oke, T. R. 1973. “City Size and the Urban Heat Island.” Atmospheric Environment (1967) 7 (8): 769–79. https://doi.org/10.1016/0004-6981(73)90140-6.

Oke, T. R. 1979. “Advectively-Assisted Evapotranspiration from Irrigated Urban Vegetation.” Boundary-Layer Meteorology 17 (2): 167–73. https://doi.org/10.1007/BF00117976.

Ozyavuz, Murat. 2012. Landscape Planning. IntechOpen, pp. 107-122.

Qiao, Zhi, Chen Wu, Dongqi Zhao, Xinliang Xu, Jilin Yang, Li Feng, Zongyao Sun, and Luo Liu. 2019. “Determining the Boundary and Probability of Surface Urban Heat Island Footprint Based on a Logistic Model.” Remote Sensing 11 (11): 1368. https://doi.org/10.3390/rs11111368.

Ramírez-Aguilar, Edwin Alejandro, and Léa Cristina Lucas Souza. 2019. “Urban Form and Population Density: Influences on Urban Heat Island Intensities in Bogotá, Colombia.” Urban Climate 29 (September): 100497. https://doi.org/10.1016/j.uclim.2019.100497.

Sampson, Paul. 2007. “SOLRIS Accuracy Assessment Report 1: Golden Horseshoe Area (SOLRIS Study Area A).” Accuracy Assessment 1 (Version 2.0). Peterborough, ON: Ministry of Natural Resources.

Science and Research Branch of the Ministry of Natural Resources and Forestry. 2019. “Southern Ontario Land Resource Information System (SOLRIS) Version 3.0 : Data Specifications.” Ministry of Natural Resources.

Skelhorn, Cynthia P., Geoff Levermore, and Sarah J. Lindley. 2016. “Impacts on Cooling Energy Consumption Due to the UHI and Vegetation Changes in Manchester, UK.” Energy and Buildings 122 (June): 150–59. https://doi.org/10.1016/j.enbuild.2016.01.035.

Sobrino, J. A., R. Oltra-Carrió, G. Sòria, R. Bianchi, and M. Paganini. 2012. “Impact of Spatial Resolution and Satellite Overpass Time on Evaluation of the Surface Urban Heat Island Effects.” Remote Sensing of Environment, Remote Sensing of Urban Environments, 117 (February): 50–56. https://doi.org/10.1016/j.rse.2011.04.042.

Streutker, D. R. 2002. “A Remote Sensing Study of the Urban Heat Island of Houston, Texas.” International Journal of Remote Sensing 23 (13): 2595–2608. https://doi.org/10.1080/01431160110115023.

Streutker, David R. 2003. “Satellite-Measured Growth of the Urban Heat Island of Houston, Texas.” Remote Sensing of Environment 85 (3): 282–89. https://doi.org/10.1016/S0034-4257(03)00007-5.

Sun, Qinqin, Zhifeng Wu, and Jianjun Tan. 2012. “The Relationship between Land Surface Temperature and Land Use/Land Cover in Guangzhou, China.” Environmental Earth Sciences 65 (6): 1687–94. https://doi.org/10.1007/s12665-011-1145-2.

Tomlinson, Charlie J., Lee Chapman, John E. Thornes, and Christopher Baker. 2011. “Remote Sensing Land Surface Temperature for Meteorology and Climatology: A Review.” Meteorological Applications 18 (3): 296–306. https://doi.org/10.1002/met.287.

Touchaei, A. G., and Y. Wang. 2015. “Characterizing Urban Heat Island in Montreal (Canada)—Effect of Urban Morphology.” Sustainable Cities and Society 19 (December): 395–402. https://doi.org/10.1016/j.scs.2015.03.005.

Wang, Kaicun, Shaojing Jiang, Jiankai Wang, Chunlüe Zhou, Xiaoyan Wang, and Xuhui Lee. 2017. “Comparing the Diurnal and Seasonal Variabilities of Atmospheric and Surface Urban Heat Islands Based on the Beijing Urban Meteorological Network.” Journal of Geophysical Research: Atmospheres 122 (4): 2131–54. https://doi.org/10.1002/2016JD025304.

Wang, Yupeng, Umberto Berardi, and Hashem Akbari. 2016. “Comparing the Effects of Urban Heat Island Mitigation Strategies for Toronto, Canada.” Energy and Buildings, SI: Countermeasures to Urban Heat Island, 114 (February): 2–19. https://doi.org/10.1016/j.enbuild.2015.06.046.

Yang, Qiquan, Xin Huang, and Qiuhong Tang. 2019. “The Footprint of Urban Heat Island Effect in 302 Chinese Cities: Temporal Trends and Associated Factors.” Science of The Total Environment 655 (March): 652–62. https://doi.org/10.1016/j.scitotenv.2018.11.171.

Yao, Rui, Lunche Wang, Xuan Gui, Yukun Zheng, Haoming Zhang, and Xin Huang. 2017. “Urbanization Effects on Vegetation and Surface Urban Heat Islands in China’s Yangtze River Basin.” Remote Sensing 9 (6): 540. https://doi.org/10.3390/rs9060540.

Yao, Rui, Lunche Wang, Xin Huang, Wei Gong, and Xiangao Xia. 2019. “Greening in Rural Areas Increases the Surface Urban Heat Island Intensity.” Geophysical Research Letters 46 (4): 2204–12. https://doi.org/10.1029/2018GL081816.

Yu, Zhaowu, Yawen Yao, Gaoyuan Yang, Xiangrong Wang, and Henrik Vejre. 2019. “Strong Contribution of Rapid Urbanization and Urban Agglomeration Development to Regional Thermal Environment Dynamics and Evolution.” Forest Ecology and Management 446 (August): 214–25. https://doi.org/10.1016/j.foreco.2019.05.046.

Zhang, Da-Lin, Yi-Xuan Shou, Russell R. Dickerson, and Fei Chen. 2011. “Impact of Upstream Urbanization on the Urban Heat Island Effects along the Washington–Baltimore Corridor.” Journal of Applied Meteorology and Climatology 50 (10): 2012–29.

Zhang, Xiaoyang, Mark A. Friedl, Crystal B. Schaaf, Alan H. Strahler, and Annemarie Schneider. 2004. “The Footprint of Urban Climates on Vegetation Phenology.” Geophysical Research Letters 31 (12). https://doi.org/10.1029/2004GL020137.

Zhou, Decheng, Jingfeng Xiao, Stefania Bonafoni, Christian Berger, Kaveh Deilami, Yuyu Zhou, Steve Frolking, Rui Yao, Zhi Qiao, and José A. Sobrino. 2019. “Satellite Remote Sensing of Surface Urban Heat Islands: Progress, Challenges, and Perspectives.” Remote Sensing 11 (1): 48. https://doi.org/10.3390/rs11010048.

Zhou, Decheng, Shuqing Zhao, Liangxia Zhang, Ge Sun, and Yongqiang Liu. 2015. “The Footprint of Urban Heat Island Effect in China.” Scientific Reports 5 (1): 1–11. https://doi.org/10.1038/srep11160.

Zhou, Weiqi, Yuguo Qian, Xiaoma Li, Weifeng Li, and Lijian Han. 2014. “Relationships between Land Cover and the Surface Urban Heat Island: Seasonal Variability and Effects of Spatial and Thematic Resolution of Land Cover Data on Predicting Land Surface Temperatures.” Landscape Ecology 29 (1): 153–67. https://doi.org/10.1007/s10980-013-9950-5.

Zhu, Xinming, Xuhong Wang, Dajiang Yan, Zhuang Liu, and Yongfang Zhou. 2019. “Analysis of Remotely-Sensed Ecological Indexes’ Influence on Urban Thermal Environment Dynamic

Using an Integrated Ecological Index: A Case Study of Xi'an, China." International Journal of Remote Sensing 40 (9): 3421–47. https://doi.org/10.1080/01431161.2018.1547448.

Chapter 4

Conclusion

This thesis presents two manuscripts using temperature as the main variable to examine its influence within an urbanizing low-density region. The results are important in understanding the influence on impervious and bio-productive surfaces based on scale and location within a local urban heat island (UHI) footprint. The first manuscript compares the relationship land surface temperature (LST) products with 1 km and 30 m spatial resolutions have with air temperature (T_{air}) within different land cover surfaces. The second manuscript compares two models commonly applied to define the footprint of an UHI and examines the variables influencing their results.

As finer resolution LST data derived from Landsat 7 Enhanced Thematic Mapper (ETM+) was used throughout this research, existing models required adjustments to be applicable with Landsat 7. In Chapter 2, land covers associated with in situ T_{air} stations were decided based on distributions within a 100 m buffer. Five-years mean imagery was used in Chapter 3 (replacing annual averages with daily data from other satellites) with the UHI footprint (UHIFP) model due to the coarse temporal resolution with Landsat 7. Additionally, the finer resolution LST data provided use of residuals from the surface UHI (SUHI) Gaussian model for a spatial analysis with land cover distributions of a similar scale.

4.1.1 Key Findings

Chapter 2 displayed the significance with how snow coverage in winter has the ability to homogenously transform land surfaces. The variations between a finer scale surface temperature data and coarser scales are reduced after altering every land cover's distribution. When surface temperatures are compared with near-surface measurements, the finer resolution LST always provided the strongest relationship in winter. The only land cover in winter which the relationship

between LST and T_{air} was weaker than in summer was with coarse resolutions and forested stations. Alternatively, coarse resolution satellite data had a stronger relationship with every T_{air} land covers in summer.

Chapter 3 determined that the UHIFP of a low-density suburban center is smaller than the footprint of a major city. Within Milton, dense vegetation maximized its cooling abilities in the adjacent rural area 1.4 times the size of its urban center, and sparse vegetation's cooling area within the UHI is 2.4 times the urban size. Urban surfaces, despite not being the dominantly distributed land cover in the rural area, plays a leading role warming rural temperatures and influencing the footprint size of the UHI. Although moderately strong correlations were found between vegetation health and the SUHI Gaussian surface, moisture presented a stronger influence on a low-density urban center's UHI.

A general agreement was found between the two methods of determining the footprint of an UHI within the rural environment. With the UHIFP determining its threshold within the third buffer, the SUHI model found vegetation to maximize its cooling abilities within the first five buffers. Urban surfaces increase their heating abilities in the outer buffers, outside of the determined footprint from the UHIFP model.

4.2 Limitations

Many studies in the past have used ground station LST data for comparisons with satellite-derived LST and T_{air}. If in situ LST stations were placed within the study area, surface temperature measurements from ground stations could operate as an additional dimension with the satellite derived LST and T_{air}. Its inclusion would have provided an additional scale to compare the variability between coarse and fine satellite data.

A limitation which affected both manuscripts relates to the land cover product used with this research. The SOLRIS dataset which provides accurate land cover distribution data was insufficient in distinctively classifying different agricultural and urban land covers. The

‘undifferentiated’ classification incorporated into the agricultural category presents surfaces that are either tilled, hydro fields, forest openings, or brownfields (Science and Research Branch of the Ministry of Natural Resources and Forestry, 2019). The inability to differentiate crops from other sparsely vegetated surfaces forced open field pixels to be classified as agricultural. Additionally, traffic is a major contributor to urban pollution, and in effect, an UHI (Keeratikasikorn & Bonafoni, 2018). The lack of historical traffic data with associated road surfaces prevented the research in this thesis from examining the role and impact of vehicular exhausts and degrees of congestion.

In addition, Southern Ontario contains an inadequate supply of wetlands with local weather stations. All linear regression analyses performed with in situ wetlands stations and Landsat 7 were inconclusive due to the temporal resolution and insufficient supply of wetlands stations. An alternative site is required to investigate the relationship.

Milton’s proximity to the major metropolitan Toronto, and its adjacent suburban centers (Mississauga, Oakville, Brampton, and Burlington) being located closer, heavily affects the background rural temperatures. As both models in Chapter 3 use surrounding rural temperature values to calculate the UHI and its footprint, Milton’s rural temperatures are already modified from surrounding UHI footprints. This issue is mostly unavoidable due to urban development patterns explored in Chapter 1. Although small independent low-density urban centers exist throughout Canada, the degree of expansion is heavily dwarfed by their suburban counterparts.

In regards to the Landsat 7 sensor, on May 31 2003, the scan line corrector responsible for making adjustments for the curvature of the Earth’s surface failed (Sadiq et al., 2017). After that date, all acquired images contain gaps that widen out from the image’s bottom with a 22% pixilation loss (Lee et al., 2016). Despite the multitude of efforts made to interpolate the lost pixel data with accuracies as high as 94.1% (Asare et al., 2020; Lee et al., 2016; Sadiq et al., 2017), no methods were implemented in this study. This decision retains the consistency and reliability of

the digital numbers with all of the imagery. With the majority of the interpolation techniques focused on the recovery of lost pixels with the visual and near-infrared bands, the thermal infrared (TIR) band, which is heavily used to study UHI, does not get as much attention (Chen et al., 2011). In terms of LST retrieval, the TIR band contains some of the most important data. In order to avoid manipulating meaningful data in this thesis, no interpolation technique was implemented.

4.3 Future Work

New abilities to calculate the UHIFP within smaller urban centers using 5-years averaged products enables similar comparisons to be made with similar sized communities. Since the suburban population accounted for 66% of the Canadian urban population in 2006 (Gordon & Janzen, 2013), more studies will be required to gain a generalized analysis of the impact with low-density urban centers. Milton's results, producing a smaller footprint compared to larger cities in Eastern North America (Zhang et al., 2004), also introduces new concepts to explore. Its rural environment's vegetation has already been influenced by the adjacent centers' UHI. Comparisons with communities at a similar size with no major city dependency can further define the impact with a low-density urban center's UHI.

Improvements in differentiating and diversifying sparse vegetation and urban surfaces will allow for a more complete examination of residuals from the SUHI model. Although 19 unique classes were found in the SOLRIS dataset surrounding Milton, they were categorically grouped due to limited pixel quantities and broad categorizations for some classifications. Robust diversification and further detail is necessary for many land covers, especially with undifferentiated, tilled, built-up, and transportation. Its use will help determine the influence that individual crops, urban densities, urban vegetation distributions, and varied levels of transportation based on traffic density have on the built and rural environment.

The limitations with the Landsat 7 overpass time and temporal resolution prevents a robust time series analysis of the magnitude and spatial extent of the SUHI model. Although the spatial resolution meets the requirements, near daily morning imagery is necessary to adequately understand the UHI development and appropriately model its magnitude (Sobrino et al., 2012). Until a sensor with those qualities is launched, a complete time series analysis with a similar urban size as Milton using the SUHI model is not possible.

4.4 References

Asare, Y. M., Forkuo, E. K., Forkuor, G., & Thiel, M. (2020). Evaluation of gap-filling methods for Landsat 7 ETM+ SLC-off image for LULC classification in a heterogeneous landscape of West Africa. International Journal of Remote Sensing, 41(7), 2544–2564. https://doi.org/10.1080/01431161.2019.1693076

Chen, F., Tang, L., Wang, C., & Qiu, Q. (2011). Recovering of the thermal band of Landsat 7 SLC-off ETM+ image using CBERS as auxiliary data. Advances in Space Research, 48(6), 1086–1093. https://doi.org/10.1016/j.asr.2011.05.012

Gordon, D. L. A., & Janzen, M. (2013). Suburban Nation? Estimating the size of Canada's Suburban Population. Journal of Architectural and Planning Research, 30(3).

Keeratikasikorn, C., & Bonafoni, S. (2018). Satellite Images and Gaussian Parameterization for an Extensive Analysis of Urban Heat Islands in Thailand. Remote Sensing, 10(5), 665. https://doi.org/10.3390/rs10050665

Lee, S., Cho, M., & Lee, C. (2016). An Effective Gap Filtering Method for Landsat ETM+ SLC-Off Data. Terrestrial, Atmospheric, and Oceanic Sciences, 27(6), 921–932. https://doi.org/10.3319/TAO.2016.07.18.02

Sadiq, A., Edwar, L., & Sulong, G. (2017). Recovering the large gaps in Landsat 7 SLC-off imagery using weighted multiple linear regression (WMLR). Arabian Journal of Geosciences, 10(18), 403. https://doi.org/10.1007/s12517-017-3121-y

Science and Research Branch of the Ministry of Natural Resources and Forestry. (2019). Southern Ontario Land Resource Information System (SOLRIS) Version 3.0: Data Specifications. Ministry of Natural Resources.

Sobrino, J. A., Oltra-Carrió, R., Sòria, G., Bianchi, R., & Paganini, M. (2012). Impact of spatial resolution and satellite overpass time on evaluation of the surface urban heat island effects. Remote Sensing of Environment, 117, 50–56. https://doi.org/10.1016/j.rse.2011.04.042

Zhang, X., Friedl, M. A., Schaaf, C. B., Strahler, A. H., & Schneider, A. (2004). The footprint of urban climates on vegetation phenology. Geophysical Research Letters, 31(12). https://doi.org/10.1029/2004GL020137

Appendix A

Software

Table A.1: Description of software used to process, manipulate, and visualize data.

Software	**Application**
Google Earth Engine	Processing of multispectral data (All chapters) - LST calculation - Weather station buffer mean (Chapter 2) - Land cover means (Chapter 2) - UHIFP buffer's mean temperatures (Chapter 3) - Vegetation/Moisture index calculations (Chapter 3)
ArcGIS	Land cover processing and generation (All chapters) Map visualizations Data format conversions Buffer calculation and generation (Chapter 3)
ENVI	Spatial data processing (Chapter 2)
R	Data processing and visualization (All Chapters)
Matrix Laboratory (MATLAB)	SUHI Gaussian model data generation and visualization (Chapter 3)

Appendix B

Location of Randomly Selected Points within each land cover for Chapter 2

Table B.1: Location of all 70 randomly selected points over the area consistently agricultural throughout the study period. Projection is in WGS 1984.

Longitude	Latitude	Longitude	Latitude	Longitude	Latitude	Longitude	Latitude
-80.02	42.91	-80.19	43.84	-79.73	44.29	-79.81	43.02
-79.06	42.92	-79.57	44.37	-79.26	42.95	-80.10	42.82
-80.58	43.02	-79.27	43.91	-80.00	42.94	-79.15	43.94
-80.47	43.61	-79.65	44.11	-79.13	43.98	-80.85	43.55
-80.30	43.64	-80.59	43.43	-79.69	42.99	-81.05	43.64
-80.69	44.14	-80.08	43.18	-80.95	43.50	-80.80	43.53
-79.84	43.16	-81.04	43.43	-80.97	43.54	-79.20	43.92
-80.21	42.94	-80.21	43.94	-79.79	43.01	-80.87	43.01
-80.13	42.82	-80.34	43.53	-80.16	43.14	-81.04	43.74
-80.86	43.45	-80.74	43.26	-79.41	43.01	-80.63	43.02
-79.65	43.14	-80.61	43.98	-80.72	43.30	-80.73	44.11
-80.05	44.25	-80.15	42.87	-80.87	43.29	-80.32	43.71
-79.37	43.07	-80.58	43.82	-80.74	43.58	-79.29	44.06
-78.98	43.96	-80.14	44.26	-79.32	44.08	-80.99	43.91
-81.01	43.59	-79.76	44.36	-79.70	44.22	-81.08	43.70
-79.84	44.20	-80.48	43.57	-78.91	44.00	-80.48	42.74
-80.42	44.22	-79.52	43.06	-79.55	42.95	-79.83	44.18
		-80.38	43.68			-80.85	43.72

Table B.2: Location of all 70 randomly selected points over the area consistently forested throughout the study period. Projection is in WGS 1984.

Longitude	Latitude	Longitude	Latitude	Longitude	Latitude	Longitude	Latitude
-78.90	43.91	-79.21	43.12	-79.32	43.67	-79.54	44.33
-79.61	42.91	-79.63	43.72	-80.24	43.52	-80.62	43.30

-79.80	43.12	-79.36	43.74	-79.51	43.85	-80.74	43.14
-80.31	43.44	-80.22	43.16	-79.48	44.25	-79.50	43.69
-79.63	44.37	-79.05	43.05	-79.02	43.89	-79.69	44.39
-79.36	43.66	-79.57	43.63	-79.68	43.77	-79.45	43.88
-79.23	44.08	-79.48	44.20	-79.22	43.76	-79.61	43.68
-80.74	43.14	-79.57	43.20	-79.28	43.01	-79.41	43.13
-79.68	43.43	-80.49	43.47	-79.17	43.15	-79.63	43.57
-80.31	43.09	-80.24	43.15	-79.54	43.83	-79.79	43.35
-79.47	43.76	-80.26	43.17	-79.83	43.35	-80.42	43.68
-79.72	43.75	-80.32	43.43	-79.01	44.00	-80.31	43.53
-79.42	43.79	-79.11	43.22	-79.64	43.63	-79.74	43.55
-78.96	42.89	-79.21	43.89	-79.42	43.82	-80.28	43.53
-80.45	43.39	-79.77	43.39	-79.69	43.76	-79.70	43.71
-79.45	43.82	-79.51	43.67	-79.41	43.65	-80.12	43.45
-79.76	43.72	-79.44	44.00	-79.56	44.35	-80.52	43.52
		-79.08	43.07			-79.74	43.38

Table B.3: Location of all 70 randomly selected points over the area consistently urban throughout the study period. Projection is in WGS 1984.

Longitude	Latitude	Longitude	Latitude	Longitude	Latitude	Longitude	Latitude
-79.97	44.23	-78.96	43.85	-79.71	43.75	-80.52	43.48
-79.87	43.64	-79.53	43.68	-79.81	44.04	-80.49	43.54
-79.04	43.05	-80.38	43.19	-80.00	43.22	-79.37	43.76
-79.53	43.65	-79.67	43.58	-79.85	43.34	-79.75	43.23
-79.35	43.04	-81.08	43.59	-78.87	43.93	-79.71	43.72
-79.40	43.70	-80.00	43.50	-79.75	43.36	-79.41	43.82
-79.67	43.56	-80.95	43.73	-80.25	43.53	-80.24	43.18
-80.30	43.18	-79.54	43.86	-80.20	42.79	-79.73	44.39
-79.81	43.25	-79.39	44.32	-79.31	43.77	-79.41	43.77
-80.03	43.89	-79.56	43.83	-79.53	43.60	-79.54	43.84
-79.67	43.66	-79.21	43.19	-79.77	43.71	-78.87	43.88
-79.83	43.38	-80.32	43.79	-80.71	42.87	-79.46	44.00

-79.93	43.42	-79.25	42.96	-79.80	43.38	-78.92	42.93
-80.58	43.46	-79.12	43.83	-79.34	43.90	-79.16	43.10
-79.71	43.48	-79.81	43.33	-80.40	43.42	-79.41	44.32
-79.35	43.66	-79.54	43.73	-79.71	43.56	-79.10	43.83
-80.04	43.85	-78.95	44.11	-80.06	43.76	-80.31	43.54
		-79.33	43.84			-79.36	43.83

Table B.4: Location of all 70 randomly selected points over the area consistently open water throughout the study period. Projection is in WGS 1984.

Longitude	Latitude	Longitude	Latitude	Longitude	Latitude	Longitude	Latitude
-78.68	43.74	-79.26	43.66	-79.74	42.80	-79.08	43.52
-78.80	43.83	-79.57	42.83	-78.87	43.82	-79.72	43.30
-79.57	42.64	-78.76	43.84	-78.76	43.79	-79.52	42.70
-79.18	43.70	-79.43	42.72	-79.18	43.66	-79.58	43.41
-79.71	42.68	-79.67	42.82	-78.96	43.77	-79.89	42.79
-80.10	42.70	-79.32	43.54	-79.50	43.59	-79.38	43.48
-79.40	42.85	-80.12	42.68	-78.91	43.61	-79.37	43.19
-79.56	43.45	-78.98	43.80	-79.53	43.58	-79.81	42.78
-78.81	43.72	-79.47	43.27	-79.47	43.21	-78.74	43.66
-78.85	43.76	-79.68	42.64	-79.45	43.43	-79.35	43.28
-79.33	43.36	-78.86	43.68	-79.48	44.38	-79.23	43.36
-78.88	43.63	-79.03	43.56	-79.36	42.83	-79.60	42.71
-79.35	43.30	-79.03	43.80	-79.97	42.67	-80.02	42.74
-78.85	43.83	-79.73	42.62	-79.36	43.65	-79.10	42.83
-79.15	43.52	-79.22	43.50	-79.04	43.75	-79.98	42.64
-79.59	42.66	-80.01	42.64	-79.45	42.86	-78.83	43.76
-80.27	42.68	-79.13	42.83	-79.08	43.54	-78.84	43.72
		-79.92	42.74			-78.80	43.62

Table B.5: Location of all 70 randomly selected points over the area consistently wetlands throughout the study period. Projection is in WGS 1984.

Longitude	Latitude	Longitude	Latitude	Longitude	Latitude	Longitude	Latitude
-80.39	43.57	-80.23	44.33	-80.10	43.32	-80.03	43.43
-79.41	42.93	-79.66	43.02	-80.60	44.05	-80.07	43.74
-80.40	43.57	-80.64	43.05	-80.04	43.46	-80.07	43.62
-80.06	43.49	-79.90	43.36	-79.34	44.14	-80.33	43.47
-80.27	44.17	-80.40	42.72	-79.75	43.92	-79.47	42.94
-80.24	43.40	-80.55	42.88	-80.00	43.59	-79.10	43.86
-80.35	42.68	-80.08	43.40	-79.55	44.06	-79.60	43.11
-80.10	43.37	-80.66	42.86	-79.90	44.21	-79.25	44.15
-80.67	43.23	-80.98	43.73	-79.03	42.88	-80.24	43.41
-80.65	44.19	-80.34	43.70	-80.15	43.59	-80.37	44.23
-80.43	43.30	-80.89	43.44	-80.18	43.99	-79.13	44.18
-80.75	43.77	-80.33	44.26	-80.25	43.37	-79.92	44.38
-79.17	42.88	-80.35	43.41	-79.14	43.82	-79.27	44.26
-80.84	43.09	-80.12	43.88	-79.89	44.39	-80.04	43.96
-80.42	43.37	-79.95	44.09	-79.02	43.97	-80.41	44.12
-79.55	44.33	-79.26	44.27	-80.24	43.46	-79.04	43.00
-79.20	44.19	-80.10	43.82	-80.20	44.31	-79.15	44.22
		-79.88	44.37			-79.32	44.18

Appendix C

Further Detailed Results from LST Comparisons in Chapter 2

Table C.1: Extension of Table 2.2 including detailed results from regression analyses conducted using both MODIS satellites and Landsat 7 for days 1-99 and 291-266 of every year between 2000 and 2019. All p-values are < 0.001.

Regression Variables	R^2 Value	RMSE	Bias
12:00 Air Temperature & Aqua LST	0.7439	4.6365	3.1726
13:00 Air Temperature & Aqua LST	0.7473	4.6061	2.5791
14:00 Air Temperature & Aqua LST	0.7511	4.5724	2.2199
Daily Mean Air Temperature & Aqua LST	0.7196	4.8496	5.5773
Daily Maximum Air Temperature & Aqua LST	0.7376	4.6914	1.2749
10:00 Air Temperature & Terra LST	0.777	4.3805	3.6045
11:00 Air Temperature & Terra LST	0.7854	4.2952	2.5353
12:00 Air Temperature & Terra LST	0.7883	4.2734	1.7427
Daily Mean Air Temperature & Terra LST	0.7614	4.5417	4.1379
Daily Maximum Air Temperature & Terra LST	0.7734	4.4262	-0.1073
16:00 Air Temperature & Landsat 7 NDVI LST	0.8046	4.1612	2.4809
16:00 Air Temperature & Landsat 7 ASTER LST	0.7806	4.4996	1.6836

Table C.2: Extension of Table 2.3 including detailed results from regression analyses conducted using both MODIS satellites and Landsat 7 for days 100-290 of every year between 2000 and 2019. All p-values are < 0.001.

Regression Variables	R^2 Value	RMSE	Bias
12:00 Air Temperature & Aqua LST	0.3813	5.2846	6.0764
13:00 Air Temperature & Aqua LST	0.3805	5.2870	5.4977
14:00 Air Temperature & Aqua LST	0.3861	5.2571	5.1184
Daily Mean Air Temperature & Aqua LST	0.409	5.1585	9.6836
Daily Maximum Air Temperature & Aqua LST	0.4026	5.1863	4.2775
10:00 Air Temperature & Terra LST	0.4423	4.6789	6.1422
11:00 Air Temperature & Terra LST	0.4364	4.7007	5.1803
12:00 Air Temperature & Terra LST	0.4335	4.7143	4.4537
Daily Mean Air Temperature & Terra LST	0.4498	4.6428	8.172
Daily Maximum Air Temperature & Terra LST	0.4508	4.6384	2.7306
16:00 Air Temperature & Landsat 7 NDVI LST	0.3487	6.1143	5.283
16:00 Air Temperature & Landsat 7 ASTER LST	0.3521	6.341	4.5934

Table C.3: Detailed results from regression analyses conducted using both MODIS satellites and Landsat 7 against air temperature based on agricultural in situ stations from days 100 - 290. All p-values are < 0.001.

Regression Variables	Agricultural (Days 100-290)			
	R^2	RMSE	Bias	Observations
12:00 Air Temperature & Aqua LST	0.4207	4.8571	7.3827	6741
13:00 Air Temperature & Aqua LST	0.4199	4.8597	6.7787	6738
14:00 Air Temperature & Aqua LST	0.4273	4.8283	6.3936	6741
Daily Mean Air Temperature & Aqua LST	0.4677	4.6559	11.4638	6782
Daily Maximum Air Temperature & Aqua LST	0.45	4.7326	5.6817	6782
10:00 Air Temperature & Terra LST	0.5016	4.1444	7.405	7663
11:00 Air Temperature & Terra LST	0.4923	4.1861	6.3825	7671
12:00 Air Temperature & Terra LST	0.4845	4.2164	5.6032	7658
Daily Mean Air Temperature & Terra LST	0.5228	4.0596	9.8324	7713
Daily Maximum Air Temperature & Terra LST	0.5079	4.1223	3.9654	7713
16:00 Air Temperature & Landsat 7 NDVI LST	0.3692	5.899	6.8979	193
16:00 Air Temperature & Landsat 7 ASTER LST	0.3583	6.2879	6.0341	232

Table C.4: Detailed results from regression analyses conducted using both MODIS satellites and Landsat 7 against air temperature based on agricultural in situ stations from days 1 – 99 and 291 - 366. All p-values are < 0.001.

Regression Variables	Agricultural (Days 1-99 and 291-366)			
	R^2	RMSE	Bias	Observations
12:00 Air Temperature & Aqua LST	0.7967	4.5553	3.2964	2746
13:00 Air Temperature & Aqua LST	0.8002	4.5132	2.6845	2747
14:00 Air Temperature & Aqua LST	0.8032	4.472	2.2992	2744
Daily Mean Air Temperature & Aqua LST	0.7848	4.6748	5.9186	2773
Daily Maximum Air Temperature & Aqua LST	0.793	4.585	1.4248	2773
10:00 Air Temperature & Terra LST	0.8226	4.2136	3.724	3425
11:00 Air Temperature & Terra LST	0.8294	4.1287	2.5877	3433
12:00 Air Temperature & Terra LST	0.8296	4.137	1.7761	3446
Daily Mean Air Temperature & Terra LST	0.8128	4.3344	4.3844	3471
Daily Maximum Air Temperature & Terra LST	0.8101	4.3658	-0.0853	3472
16:00 Air Temperature & Landsat 7 NDVI LST	0.8548	3.7708	2.6472	96
16:00 Air Temperature & Landsat 7 ASTER LST	0.8249	4.2854	1.8832	130

Table C.5: Detailed results from regression analyses conducted using both MODIS satellites and Landsat 7 against air temperature based on urban in situ stations from days 100 - 290. All p-values are < 0.001.

Regression Variables	Urban (Days 100-290)			
	R^2	RMSE	Bias	Observations
12:00 Air Temperature & Aqua LST	0.5311	4.2716	5.5043	11738
13:00 Air Temperature & Aqua LST	0.5313	4.2705	4.9068	11741
14:00 Air Temperature & Aqua LST	0.5355	4.2388	4.5207	11733
Daily Mean Air Temperature & Aqua LST	0.5564	4.1423	9.352	11982
Daily Maximum Air Temperature & Aqua LST	0.5437	4.2013	3.8243	11982
10:00 Air Temperature & Terra LST	0.5821	3.837	5.8825	13033
11:00 Air Temperature & Terra LST	0.5827	3.8298	4.8369	13058
12:00 Air Temperature & Terra LST	0.5824	3.8328	4.0665	13074
Daily Mean Air Temperature & Terra LST	0.5778	3.8474	8.0562	13343
Daily Maximum Air Temperature & Terra LST	0.5855	3.8118	2.4879	13343
16:00 Air Temperature & Landsat 7 NDVI LST	0.4572	5.2276	5.8093	469
16:00 Air Temperature & Landsat 7 ASTER LST	0.4362	5.642	5.0306	569

Table C.6: Detailed results from regression analyses conducted using both MODIS satellites and Landsat 7 against air temperature based on urban in situ stations from days 1 – 99 and 291 - 366. All p-values are < 0.001.

Regression Variables	Urban (Days 1-99 and 291-366)			
	R^2	RMSE	Bias	Observations
12:00 Air Temperature & Aqua LST	0.7861	4.1093	3.4581	5025
13:00 Air Temperature & Aqua LST	0.7916	4.0575	2.8226	5042
14:00 Air Temperature & Aqua LST	0.7984	4.0019	2.47	5036
Daily Mean Air Temperature & Aqua LST	0.7588	4.3694	6.0023	5166
Daily Maximum Air Temperature & Aqua LST	0.7809	4.1644	1.6144	5166
10:00 Air Temperature & Terra LST	0.8095	3.9851	3.908	5945
11:00 Air Temperature & Terra LST	0.8188	3.8866	2.7811	5958
12:00 Air Temperature & Terra LST	0.8228	3.847	1.9228	5952
Daily Mean Air Temperature & Terra LST	0.7918	4.1818	4.4845	6126
Daily Maximum Air Temperature & Terra LST	0.8099	3.9956	0.151	6126
16:00 Air Temperature & Landsat 7 NDVI LST	0.8366	3.7915	3.096	188
16:00 Air Temperature & Landsat 7 ASTER LST	0.8067	4.1715	2.3733	277

Table C.7: Detailed results from regression analyses conducted using both MODIS satellites and Landsat 7 against air temperature based on lakeside in situ stations from days 100 - 290. All p-values are < 0.001.

Regression Variables	Lakeside (Days 100-290)			
	R^2	RMSE	Bias	Observations
12:00 Air Temperature & Aqua LST	0.3908	4.909	8.5138	4789
13:00 Air Temperature & Aqua LST	0.3872	4.9191	8.0196	4797
14:00 Air Temperature & Aqua LST	0.3862	4.924	7.6035	4792
Daily Mean Air Temperature & Aqua LST	0.3211	5.1799	10.3851	4831
Daily Maximum Air Temperature & Aqua LST	0.3954	4.8882	6.1621	4831
10:00 Air Temperature & Terra LST	0.4457	4.3293	7.6876	5511
11:00 Air Temperature & Terra LST	0.4391	4.3445	7.0554	5517
12:00 Air Temperature & Terra LST	0.4334	4.3715	6.5172	5513
Daily Mean Air Temperature & Terra LST	0.3819	4.5672	8.3848	5572
Daily Maximum Air Temperature & Terra LST	0.4396	4.3491	4.1817	5572
16:00 Air Temperature & Landsat 7 NDVI LST	0.3212	5.2401	6.1964	204
16:00 Air Temperature & Landsat 7 ASTER LST	0.3706	5.3031	5.5546	256

Table C.8: Detailed results from regression analyses conducted using both MODIS satellites and Landsat 7 against air temperature based on lakeside in situ stations from days 1 – 99 and 291 - 366. All p-values are < 0.001.

Regression Variables	Lakeside (Days 1-99 and 291-366)			
	R^2	RMSE	Bias	Observations
12:00 Air Temperature & Aqua LST	0.6791	5.4695	3.3996	1964
13:00 Air Temperature & Aqua LST	0.6785	5.4771	2.9356	1966
14:00 Air Temperature & Aqua LST	0.676	5.4888	2.5873	1962
Daily Mean Air Temperature & Aqua LST	0.6421	5.7743	4.7079	1989
Daily Maximum Air Temperature & Aqua LST	0.6679	5.5622	1.1563	1989
10:00 Air Temperature & Terra LST	0.7209	5.0116	3.274	2474
11:00 Air Temperature & Terra LST	0.7282	4.94	2.5085	2479
12:00 Air Temperature & Terra LST	0.7303	4.9316	1.9167	2477
Daily Mean Air Temperature & Terra LST	0.6975	5.2234	3.247	2504
Daily Maximum Air Temperature & Terra LST	0.7153	5.0676	-0.2602	2504
16:00 Air Temperature & Landsat 7 NDVI LST	0.7532	4.7342	1.6437	90
16:00 Air Temperature & Landsat 7 ASTER LST	0.736	4.9414	0.3831	130

Table C.9: Detailed results from regression analyses conducted using both MODIS satellites and Landsat 7 against air temperature based on forested in situ stations from days 100 - 290. All p-values are < 0.001.

Regression Variables	Forested (Days 100-290)			
	R^2	RMSE	Bias	Observations
12:00 Air Temperature & Aqua LST	0.5327	3.8748	-3.7175	1695
13:00 Air Temperature & Aqua LST	0.5269	3.8987	-4.241	1698
14:00 Air Temperature & Aqua LST	0.519	3.934	-4.4671	1698
Daily Mean Air Temperature & Aqua LST	0.5106	3.9682	0.7678	1708
Daily Maximum Air Temperature & Aqua LST	0.5035	3.9968	-5.2136	1708
10:00 Air Temperature & Terra LST	0.5292	3.8762	-2.9269	1903
11:00 Air Temperature & Terra LST	0.5172	3.926	-3.8971	1908
12:00 Air Temperature & Terra LST	0.5176	3.926	-4.5586	1908
Daily Mean Air Temperature & Terra LST	0.4982	4.0073	0.0655	1920
Daily Maximum Air Temperature & Terra LST	0.4934	4.0263	-5.9624	1920
16:00 Air Temperature & Landsat 7 NDVI LST	0.4678	4.8187	-4.7892	74
16:00 Air Temperature & Landsat 7 ASTER LST	0.3758	5.398	-5.1702	85

Table C.10: Detailed results from regression analyses conducted using both MODIS satellites and Landsat 7 against air temperature based on forested in situ stations from days 1 – 99 and 291 - 366. All p-values are < 0.001.

Regression Variables	Forested (Days 1-99 and 291-366)			
	R^2	RMSE	Bias	Observations
12:00 Air Temperature & Aqua LST	0.4845	3.2372	0.8661	883
13:00 Air Temperature & Aqua LST	0.4812	3.2415	0.3668	882
14:00 Air Temperature & Aqua LST	0.4744	3.2666	0.101	884
Daily Mean Air Temperature & Aqua LST	0.4667	3.301	3.9898	891
Daily Maximum Air Temperature & Aqua LST	0.4628	3.3129	-0.6288	891
10:00 Air Temperature & Terra LST	0.4868	3.3084	2.2958	977
11:00 Air Temperature & Terra LST	0.4982	3.2939	1.1851	980
12:00 Air Temperature & Terra LST	0.5002	3.3002	0.4744	980
Daily Mean Air Temperature & Terra LST	0.4877	3.379	3.6575	990
Daily Maximum Air Temperature & Terra LST	0.483	3.3943	-0.9713	990
16:00 Air Temperature & Landsat 7 NDVI LST	0.5964	3.5986	0.3265	23
16:00 Air Temperature & Landsat 7 ASTER LST	0.6696	3.7692	0.37679	34

Table C.11: Detailed results from regression analyses conducted using both MODIS satellites and Landsat 7 against air temperature based on forested in situ stations from days 100 - 290. All MODIS p-values are < 0.001 (with Landsat 7 it is NA).

Regression Variables	Wetlands (Days 100-290)			
	R^2	RMSE	Bias	Observations
12:00 Air Temperature & Aqua LST	0.6342	3.9862	8.8099	1041
13:00 Air Temperature & Aqua LST	0.6394	3.9608	8.1474	1039
14:00 Air Temperature & Aqua LST	0.6391	3.9589	7.7212	1028
Daily Mean Air Temperature & Aqua LST	0.5932	4.2218	13.2588	1046
Daily Maximum Air Temperature & Aqua LST	0.6476	3.929	7.1574	1046
10:00 Air Temperature & Terra LST	0.6814	3.3877	8.1491	1225
11:00 Air Temperature & Terra LST	0.6839	3.3713	7.0046	1231
12:00 Air Temperature & Terra LST	0.6821	3.3846	6.1529	1228
Daily Mean Air Temperature & Terra LST	0.6342	3.6382	10.6941	1236
Daily Maximum Air Temperature & Terra LST	0.6885	3.3576	4.6071	1236
16:00 Air Temperature & Landsat 7 NDVI LST	NA	NA	5.721	1
16:00 Air Temperature & Landsat 7 ASTER LST	NA	NA	5.461	1

Table C.12: Detailed results from regression analyses conducted using both MODIS satellites and Landsat 7 against air temperature based on forested in situ stations from days 1 – 99 and 291 - 366. All p-values are < 0.001 except with Landsat 7 NDVI where it is NA.

Regression Variables	Wetlands (Days 1-99 and 291-366)			
	R^2	RMSE	Bias	Observations
12:00 Air Temperature & Aqua LST	0.8832	3.4508	2.7788	458
13:00 Air Temperature & Aqua LST	0.8844	3.4324	2.0054	458
14:00 Air Temperature & Aqua LST	0.8846	3.4256	1.5209	459
Daily Mean Air Temperature & Aqua LST	0.8471	3.944	5.5815	461
Daily Maximum Air Temperature & Aqua LST	0.8651	3.7044	0.7589	461
10:00 Air Temperature & Terra LST	0.9064	3.1937	3.4188	621
11:00 Air Temperature & Terra LST	0.9172	3.0049	2.1289	620
12:00 Air Temperature & Terra LST	0.9168	3.0148	1.1445	622
Daily Mean Air Temperature & Terra LST	0.8954	3.3771	3.7007	625
Daily Maximum Air Temperature & Terra LST	0.8935	3.4073	-0.7811	625
16:00 Air Temperature & Landsat 7 NDVI LST	NA	NA	-0.8715	2
16:00 Air Temperature & Landsat 7 ASTER LST	0.9721	1.4713	0.9844	5

Appendix D

Additional Detail to the Results from the SUHI Gaussian Model in Chapter 3

Table D.1: Detailed time frames analysis results

	2000-2003	2004-2008	2009-2013	2014-2019
Months 4/5 Magnitude	3.93	4.78	6.67	5.14
Months 4/5 $e^{-1/2}$ Threshold	15,027.9 px	15,876.3 px	21,655.6 px	32,789.1 px
Months 4/5 1 K Threshold	41,151.3 px	49,658.4 px	82,201.6 px	107,340.9 px
Months 4/5 Correlation Coef.	0.42	0.57	0.57	0.58
Months 4/5 R^2 Value	0.17	0.31	0.30	0.31
Months 4/5 Possible Observations	11	11	11	15
Months 6/7/8 Magnitude	6.55	6.92	8.09	7.81
Months 6/7/8 $e^{-1/2}$ Threshold	17,599.5 px	17,043.0 px	18,761.1 px	28,505.4 px
Months 6/7/8 1 K Threshold	66,158.2 px	65,902.0 px	78,456.8 px	117,164.4 px
Months 6/7/8 Correlation Coef.	0.55	0.62	0.63	0.64
Months 6/7/8 R^2 Value	0.28	0.38	0.38	0.39
Months 6/7/8 Possible Observations	16	22	22	26
Months 9/10 Magnitude	3.48	5.11	4.09	5.74
Months 9/10 $e^{-1/2}$ Threshold	48,298.6 px	14,392.5 px	25,609.5 px	29,393.6 px
Months 9/10 1 K Threshold	120,380.8 px	46,960.4 px	72,078.0 px	102,721.0 px
Months 9/10 Correlation Coef.	0.52	0.47	0.49	0.63
Months 9/10 R^2 Value	0.21	0.22	0.21	0.38
Months 9/10 Possible Observations	8	9	10	12

Figure D.1: The correlation coefficient each land cover's SUHI residuals have with NDVI.

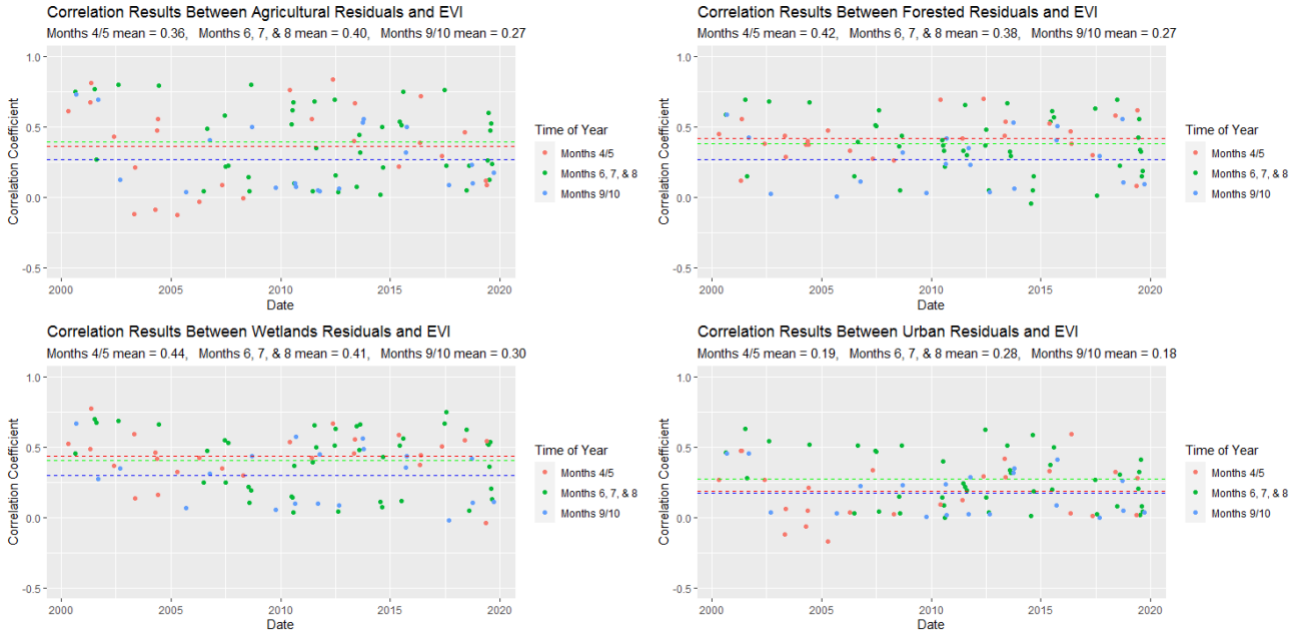

Figure D.2: The correlation coefficient each land cover's SUHI residuals have with EVI.

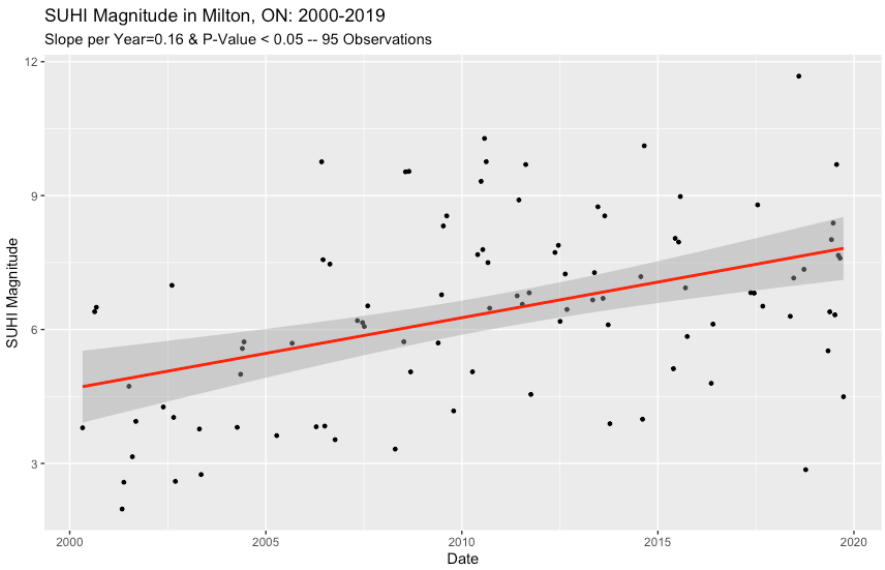

Figure D.3: The SUHI magnitude obtained from all 95 individual dates.

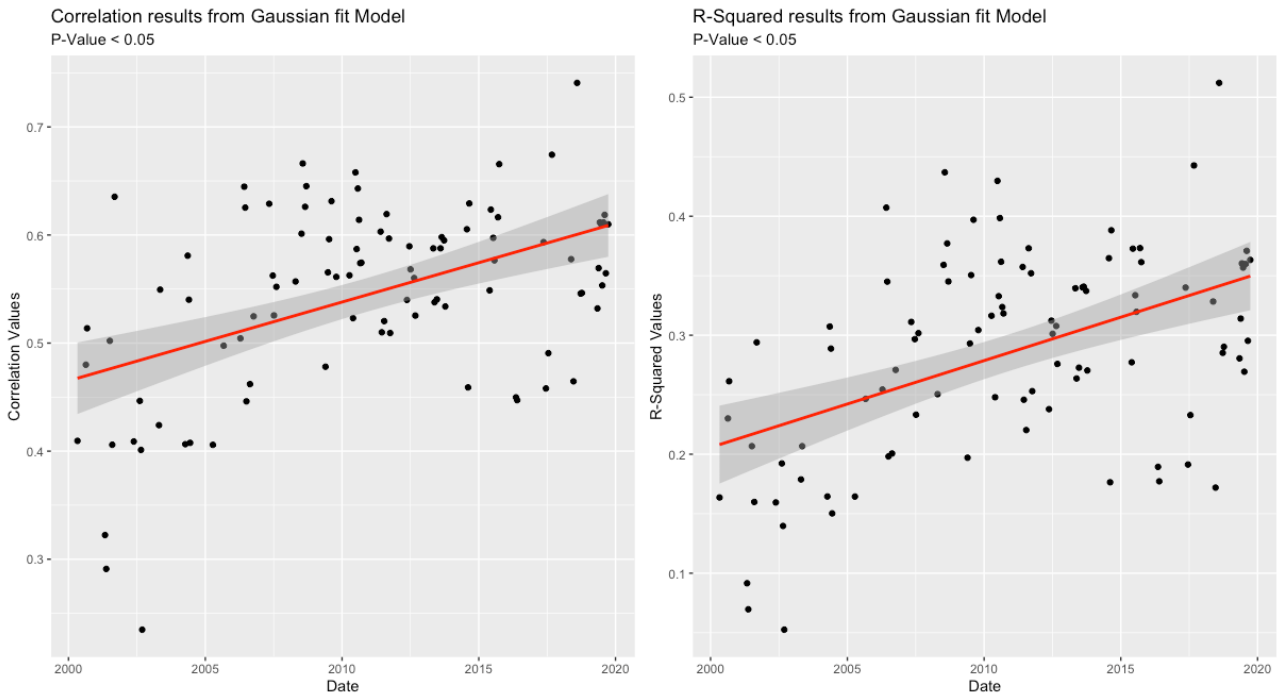

Figure D.4: The SUHI correlation coefficient and R^2 results from each individual dates with the observed trends.

Appendix E

MATLAB Script for SUHI Model

The script used for this thesis is a modification of the MATLAB script produced by Roberta Anniballe and Stefania Bonafoni.

Produce grid

```
xCenter = 591281;
yCenter = 4819112;

% Set the size of the frame
longestlength = 745; % Size varies based on land cover product

% Get new area
t = (longestlength - 1) ./ 2;

% Pixel Size
ps = 22;

%%%%%%%%%%%
Lon_MIN_s= xCenter - (t.*ps);
Lon_MAX_s= xCenter + (t.*ps);
Lat_MIN_s= yCenter - (t.*ps);
Lat_MAX_s= yCenter + (t.*ps);



yy=[Lat_MIN_s:ps:Lat_MAX_s];
xx=[Lon_MIN_s:ps:Lon_MAX_s];
yy=fliplr(yy);

xdata_ex=ones(length(xx),1)*xx;

ydata_ex=(ones(length(yy),1)*yy)';

save ydata_ex
save xdata_ex
```

Introduce UHI layers with mask and land cover differentiation

```
i='2011_06_16';

rur='rural.tif';
```

```
rural=geotiffread(append('s',i,rur));
rural=rural(:,:,3);
rural(rural==rural(1,1))=nan;
minusValue=mean(mean(rural,'omitnan'),'omitnan');

tif='.tif';
[uhi_map,Ref]=geotiffread(append('s',i,tif));
uhi_map=uhi_map(:,:,3);
uhi_map(uhi_map== uhi_map(1,1))=nan;

% Access row and column data
[R,C]=size(uhi_map);
dit=(C-R)/2;

uhi_map=[nan(dit,C);uhi_map;nan(dit,C)];
uhi_map=uhi_map-minusValue;
save uhi_map


% Save masks of each land cover
ag='agr.tif';
fo='for.tif';
we='wet.tif';
ur='urb.tif';

agr=geotiffread(append('s',i,ag));
agr=agr(:,:,3);
agr(agr==agr(1,1))=nan;
agr=[nan(dit,C);agr;nan(dit,C)];
agrlogic=~isnan(agr);

fores=geotiffread(append('s',i,fo));
fores=fores(:,:,3);
fores(fores==fores(1,1))=nan;
fores=[nan(dit,C);fores;nan(dit,C)];
foreslogic=~isnan(fores);

wet=geotiffread(append('s',i,we));
wet=wet(:,:,3);
wet(wet==wet(1,1))=nan;
wet=[nan(dit,C);wet;nan(dit,C)];
wetlogic=~isnan(wet);

urb=geotiffread(append('s',i,ur));
urb=urb(:,:,3);
urb(urb==urb(1,1))=nan;
urb=[nan(dit,C);urb;nan(dit,C)];
```

```
urblogic=~isnan(urb);

save agrlogic
save foreslogic
save wetlogic
save urblogic
```

Create mask for each buffer

```
for i = (1:1:12)
    e=num2str(i)
    buffer=['2002B',e,'.tif']
    B= readgeoraster(buffer);
    B(B==B(1,1))=nan;
    B=[nan(dit,C);B;nan(dit,C)];
    Blog=~isnan(B);
    save(['Y2015B' num2str(i) '.mat'],'Blog');
end
```

Gaussian Fitting

```
% %This script perform the fitting of a UHI map to an elliptical Gaussian surface by
using the Matlab function lsqcurvefit

% % INPUT
% % uhi_map - The NxN array of the data to fit.
% % xdata - The NxN array of the x coordinates in meters(centers of pixels).
% % ydata - The NxN array of the y coordinates in meters(centers of pixels).
% % pixel_size - the pixel size in meters
% % OUTPUT
% % gaussuhi - A structure composed by two elements:
% %   par - a structure which contains the Gaussian fit parameters:
% %       a0- is the UHI magnitude
% %       Xc- is the x coordinate of the UHI central location, defined as
% %       shift in km from the center of the map
% %       Yc- is the x coordinate of the UHI central location, defined as
% %       shift in km from the center of the map
% %       orientation - is the rotation of the elliptical footprint from the X axis in
degrees
% %       A_61- is the area at which the temperature falls to the 61% of its maximum
value, in km^2 (inner ellipse)
% %       A_1K- is the area for which the UHI temperature is greater than 1 K, in km^2
(outer ellipse).
% %   gof - a structure which contains information on the goodness of the fit
% %       corr- is the correlation coefficient between the Gaussian model and the UHI
image
% %       Rsquare- is the coefficient of determination
```

```
%%
%clear all
%close all
%clc
%% Input data
load('xdata_ex');
load('ydata_ex');
load('uhi_map');
xdata=xdata_ex;
ydata=ydata_ex;
uhi_map= uhi_map;
pixel_size=30;
%%
center_px_idx=ceil(size(ydata,2)/2);
fn=ydata(center_px_idx,center_px_idx);
fe=xdata(center_px_idx,center_px_idx);
x=(xdata-fe)/pixel_size;
y=(ydata-fn)/pixel_size;

%% Initial guess parameters estimation
zz=uhi_map(1:end)';
ind=find(zz>0 & ~isnan(zz));
xx=x(1:end)';
xx=xx(ind);
yy=y(1:end)';
yy=yy(ind);
zzlog=log(zz(ind));
q=[xx.^2, xx.*yy, yy.^2, xx, yy, ones(size(xx))];
qtq=q'*q;
qtz=q'*zzlog;
c=qtq\qtz
clear zz xx yy  zzlog q qtq qtz ind
%%

%% Gaussian fitting
Fun=@(p,x_data)exp(p(1).*x_data(:,:,1).^2+p(2).*x_data(:,:,1).*x_data(:,:,2)+p(3).*x_data
(:,:,2).^2+p(4).*x_data(:,:,1)+p(5).*x_data(:,:,2)+p(6));
uhi_notisnan=find(~isnan(uhi_map));
x_d1(:,:,1)=x(uhi_notisnan);
x_d1(:,:,2)=y(uhi_notisnan);
[par,resnorm,residual,exitflag,output] = lsqcurvefit(Fun,c,x_d1,uhi_map(uhi_notisnan));
p1=par(1);p2=par(2);p3=par(3);p4=par(4);p5=par(5);p6=par(6);
%%
% Create a residuals matrix
uhi_nan=~isnan(uhi_map);
uhi_residual1=nan(size(uhi_nan));
uhi_residual1(uhi_nan)=residual;
```

```
%% Gaussian fit parameters computation
% %UHI central location (Xc, Yc)defined as shift in km from the center of the
% %map
Xc= ((2*p3*p4 - p2*p5)/(p2*p2 - 4*p1*p3)) * pixel_size/22;
Yc= ((2*p1*p5 - p2*p4)/(p2*p2 - 4*p1*p3))* pixel_size/22;
% %UHI magnitude
A0=exp(p6-p1*Xc^2-p2*Xc*Yc-p3*Yc^2);
% %Major and minor axes of the inner elliptical footprint
invax2=-((p1+p3)+ sqrt((p1-p3)^2+p2^2))/4;%1/ax^2
ax=sqrt(invax2^(-1));
invay2=-((p1+p3)- sqrt((p1-p3)^2+p2^2))/4;%1/ay^2
ay=sqrt(invay2^(-1));
clear invax2 invay2
% %UHI area A_61% (inner ellipse)
sax=ax/2*pixel_size/22;
say=ay/2*pixel_size/22;
uhi_area_gauss=sax*say*pi;
% %UHI area A_1K% (outer ellipse)
sax1K=2*sax*sqrt(log(A0)/2);
say1K=2*say*sqrt(log(A0)/2);
uhi_area1K=sax1K*say1K*pi;
% %Rotation of the elliptical footprint from the X axis in degrees, counter-clockwise
due_theta_rad=atan(p2/(p1-p3));
if(due_theta_rad<0)
   due_theta_rad=pi-abs(due_theta_rad);
   if (p1>p3)
       theta_Rad=pi/2+due_theta_rad/2;
   else
       theta_Rad=due_theta_rad/2;
   end
else
    if (p1>p3)
        theta_Rad=due_theta_rad/2;

   else
       theta_Rad=pi/2+due_theta_rad/2;
   end
end
theta_deg=theta_Rad*180/pi;

x_data1(:,:,1) = x;
x_data1(:,:,2) = y;
f=Fun(par,x_data1);
corr=corrcoef(f(uhi_notisnan),uhi_map(uhi_notisnan));
SSE=sum((f(uhi_notisnan)-uhi_map(uhi_notisnan)).^2);
Rsquare=1-SSE/sum((uhi_map(uhi_notisnan)-mean(uhi_map(uhi_notisnan))).^2);
```

```
gaussuhi1.a0=A0;
gaussuhi1.Xc=Xc;
gaussuhi1.Yc=Yc;
if theta_deg<90
    gaussuhi1.orientation=theta_deg;
else
    gaussuhi1.orientation=theta_deg-180;
end

gaussuhi1.A_61=uhi_area_gauss;
gaussuhi1.A_1K=uhi_area1K;
gaussuhi1.M_sax=sax;
gaussuhi1.m_sax=say;
gaussuhi1.M_sax_1K=sax1K;
gaussuhi1.m_sax_1K=say1K;
gaussuhi1.corr=corr(1,2);
gaussuhi1.Rsquare=Rsquare;
```

Appendix F

SUHI Gaussian Model Result Examples

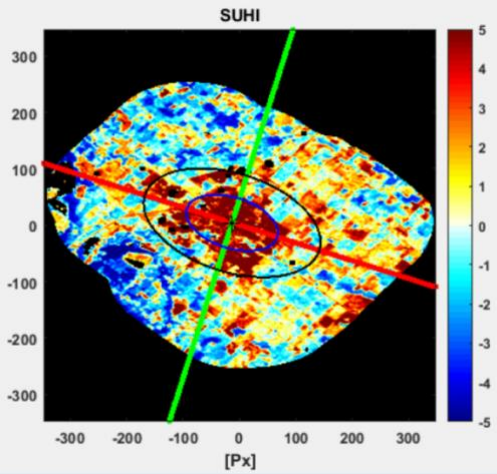

A_0	6.50
X_c	-13.16
Y_c	4.30
φ	-17.52
A_61	11,875 pixels
A_1K	44,447 pixels
correlation	0.51

Figure F.1: The SUHI model results for September 5, 2000.

Gaussian fit parameters: A0 is magnitude (K), Xc and Yc are the central location of the UHI, φ is the orientation. The blue ellipse (inner) is the area at which the temperature falls to the 61% of its maximum value (A_61) and the black ellipse (outer) is the area for which the SUHI temperature is greater than 1 K (A_1K).

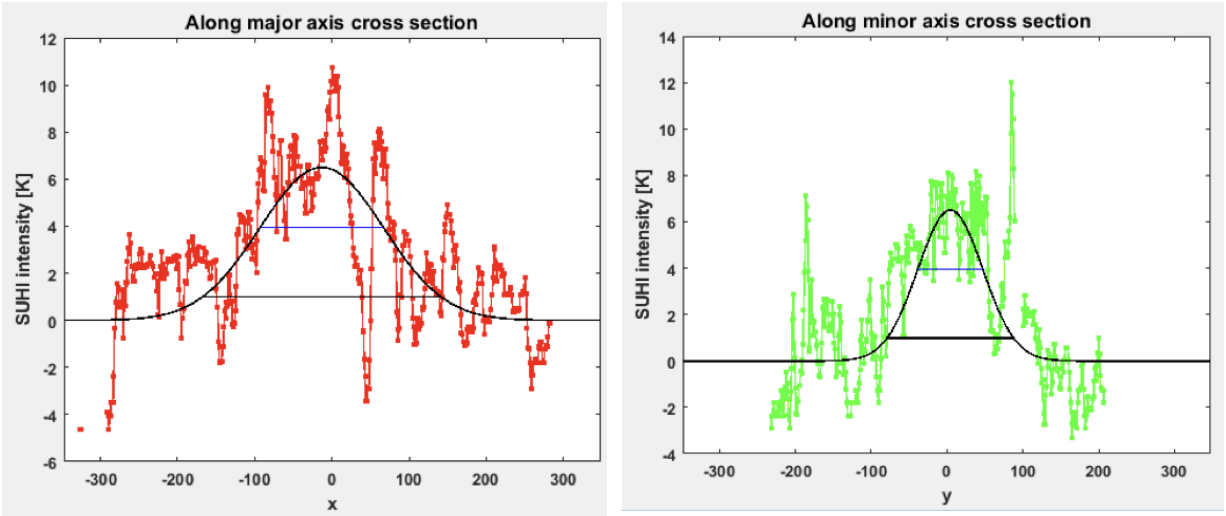

Figure F.2: SUHI correspondent to the vertical cross-section of the Gaussian surface presented in Figure F1 along the major axis (left) and minor axis (right).

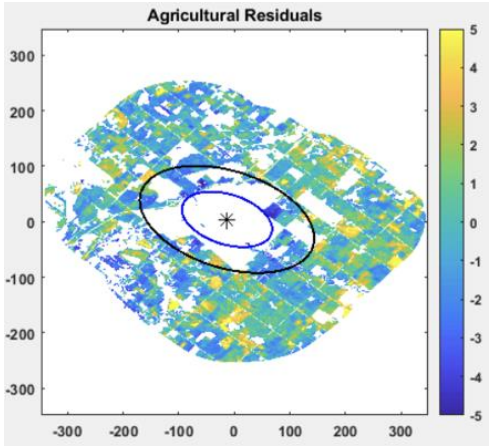

	Agriculture	Urban
Mean	0.09	1.16
Stand. Dev.	0.32	0.73
Median	0.03	1.09
Quantity > 0	71,831	34,841
Quantity < 0	77,751	15,034
Maximum	11.05	22.15
Minimum	-6.95	-7.03

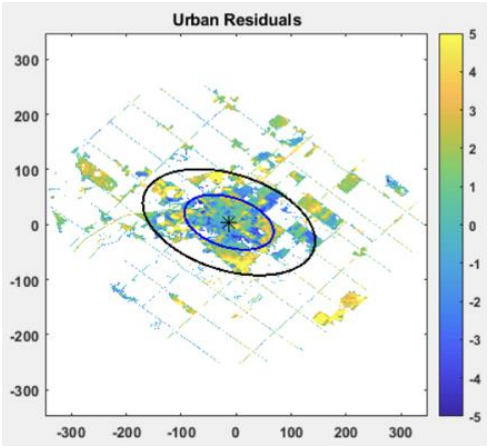

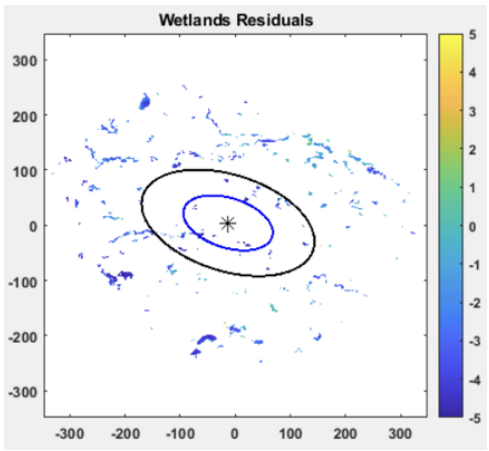

	Wetlands	Forested
Mean	-2.55	-2.84
Stand. Dev.	0.55	0.46
Median	-2.76	-2.93
Quantity > 0	459	719
Quantity < 0	7,570	21,423
Maximum	3.95	6.78
Minimum	-8.15	-8.48

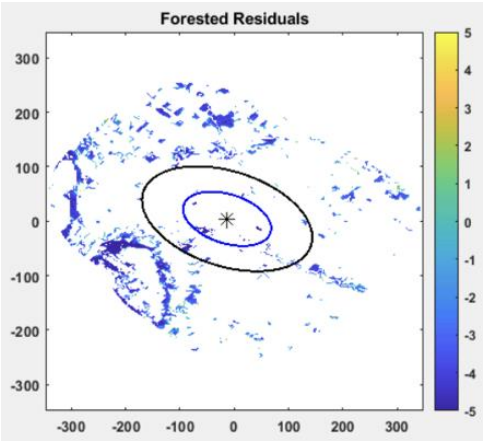

Figure F.3: Residuals within each land cover from the SUHI Gaussian surface presented in Figure F1

Included in the center are the statistics used for residuals analyses in Chapter 3. The blue ellipse represents the A_61% area and the black ellipse represents the A_1K area.

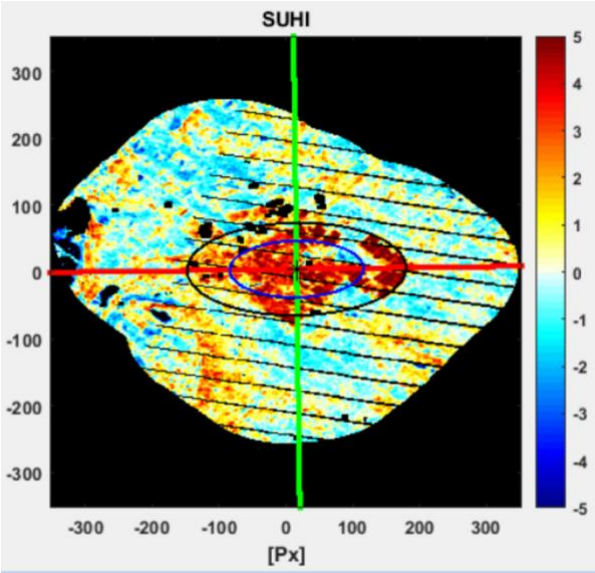

A_0	3.82
X_c	16.09
Y_c	4.32
φ	-0.76
A_61	13,259 pixels
A_1K	35,550 pixels
correlation	0.50

Figure F.4: The SUHI results for April 15, 2006.

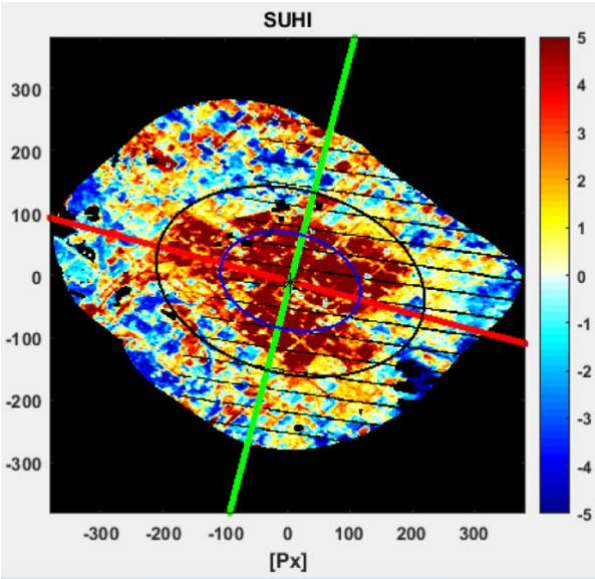

A_0	6.30
X_c	4.58
Y_c	-10.06
φ	-14.79
A_61	27,475 pixels
A_1K	101,115 pixels
correlation	0.58

Figure F.5: The SUHI results for May 18, 2018.

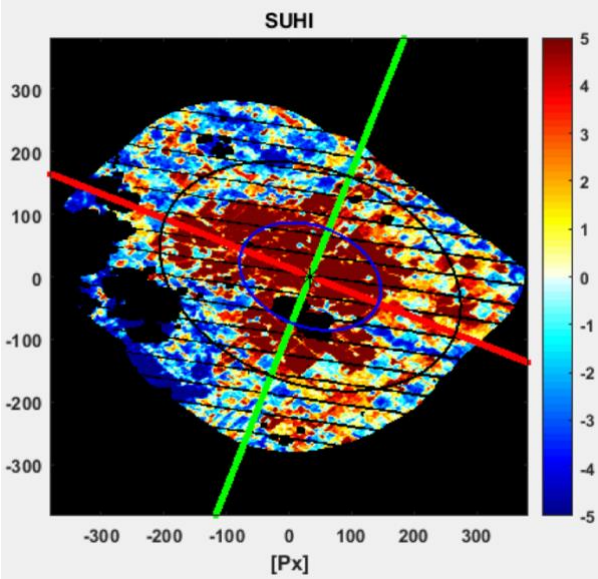

A_0	9.70
X_c	33.73
Y_c	0.68
φ	-21.56
A_61	29,434 pixels
A_1K	133,735 pixels
correlation	0.61

Figure F.6: The SUHI results for July 24, 2019.

Appendix G

Additional UHIFP Results

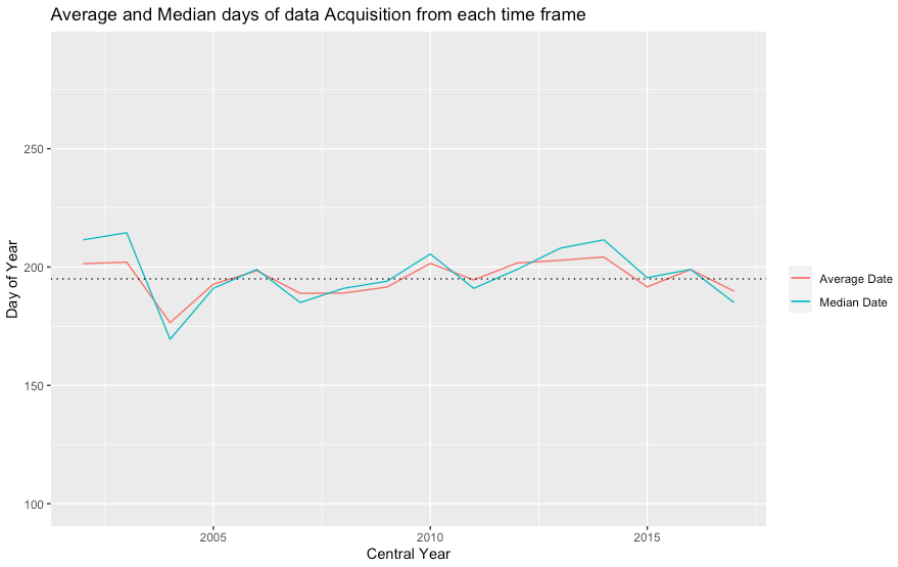

Figure G.1: Average and median days of data acquisition from each time frame for the UHIFP

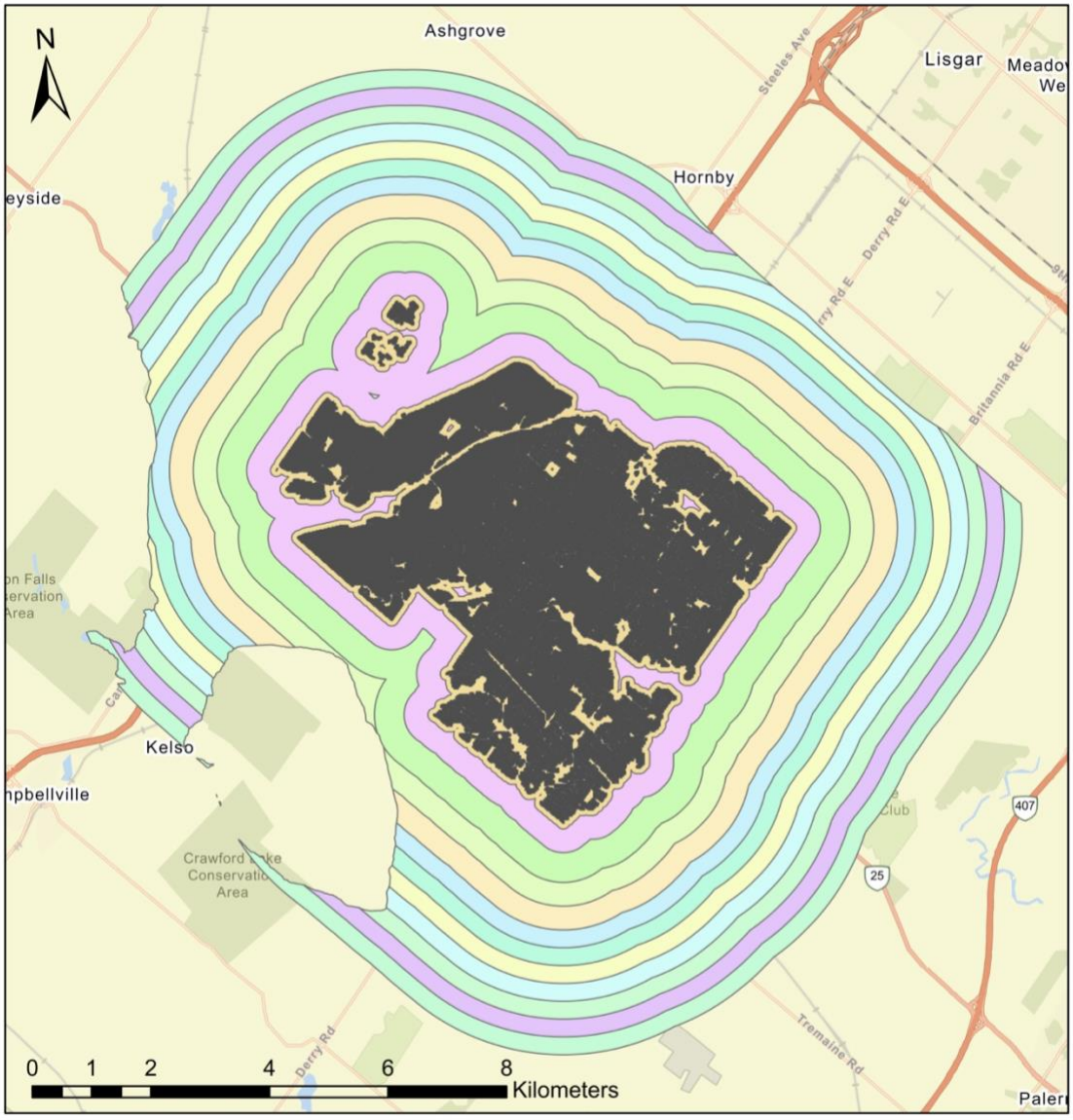

Figure G.2: Distribution of rural buffers around Milton's urban centre with the 2015 land cover product used in UHIFP model.

Appendix H

Additional Milton Data

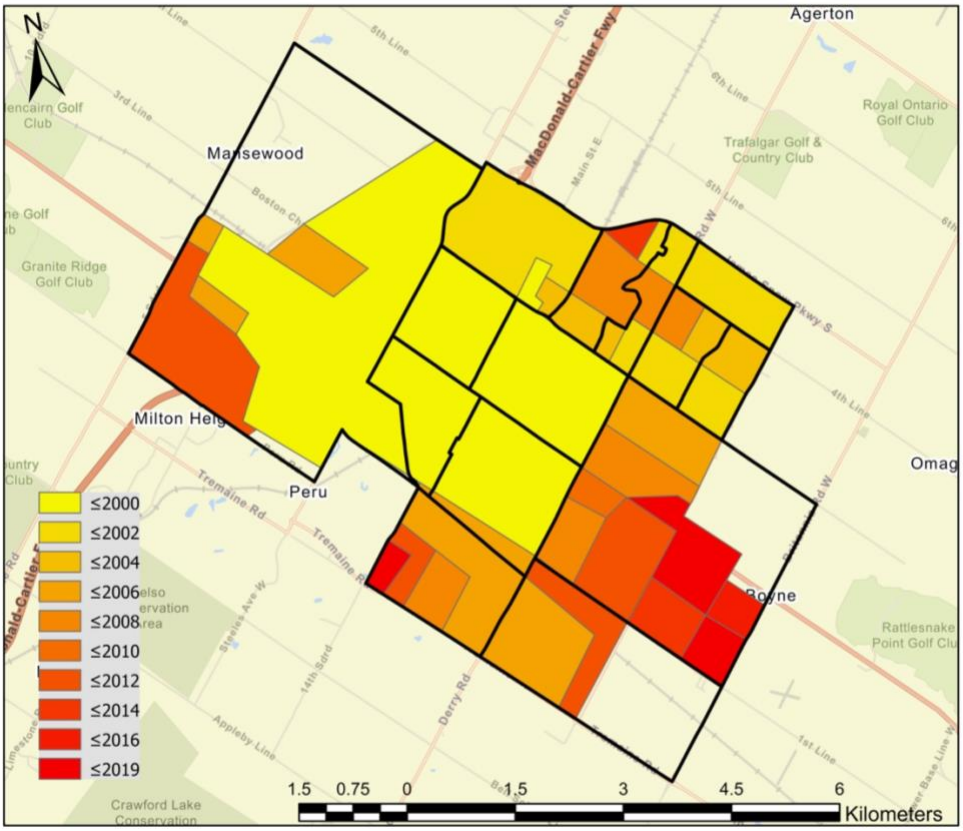

Figure H.1 : Visual representation of Urban Milton's urban extent from satellite imagery acquired every two years.

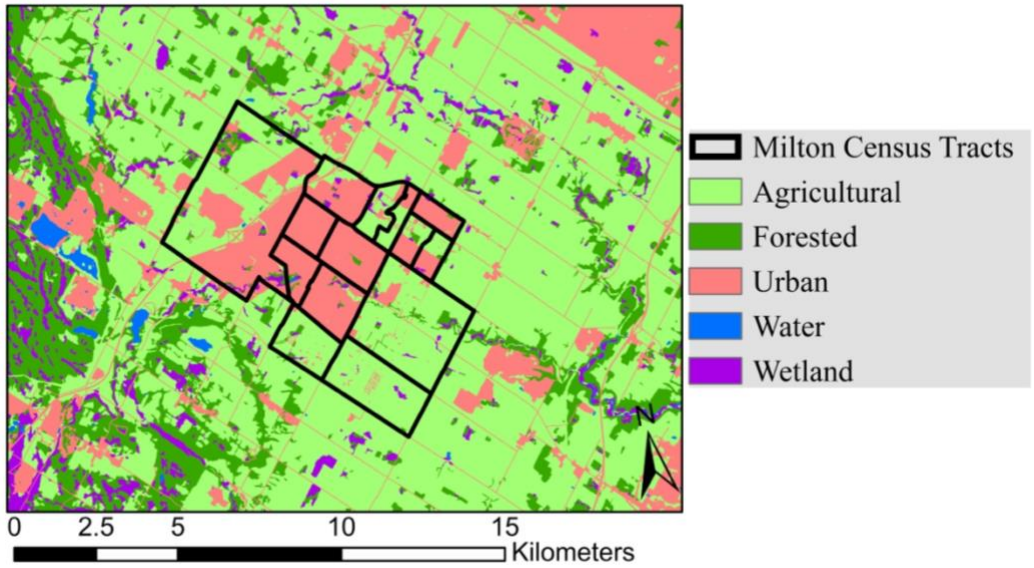

Figure H.2 : The distribution of land covers surrounding Urban Milton in the 2002 land cover product.

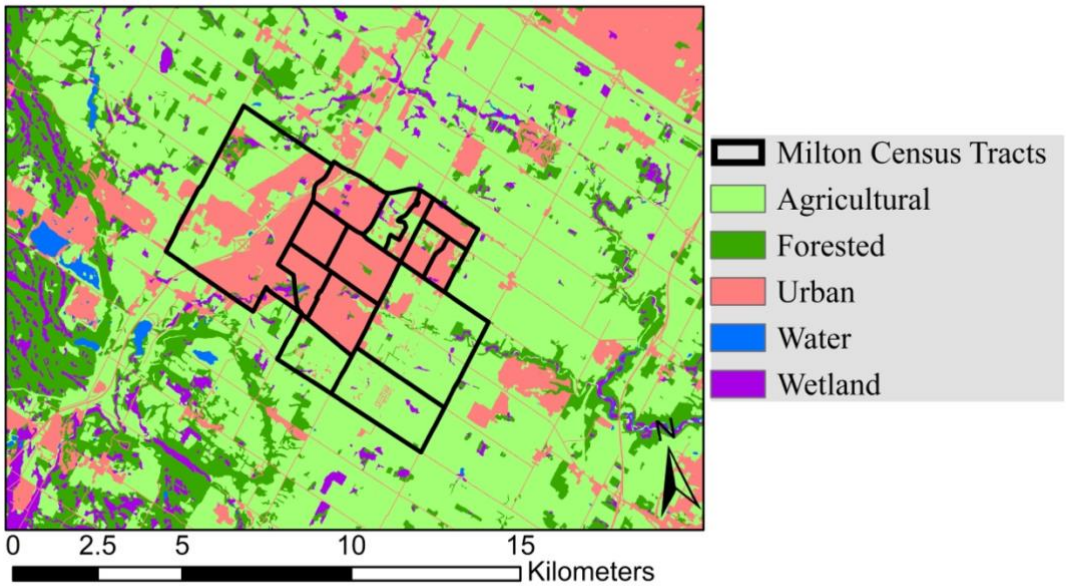

Figure H.3 : The distribution of land covers surrounding Urban Milton in the 2006 land cover product.

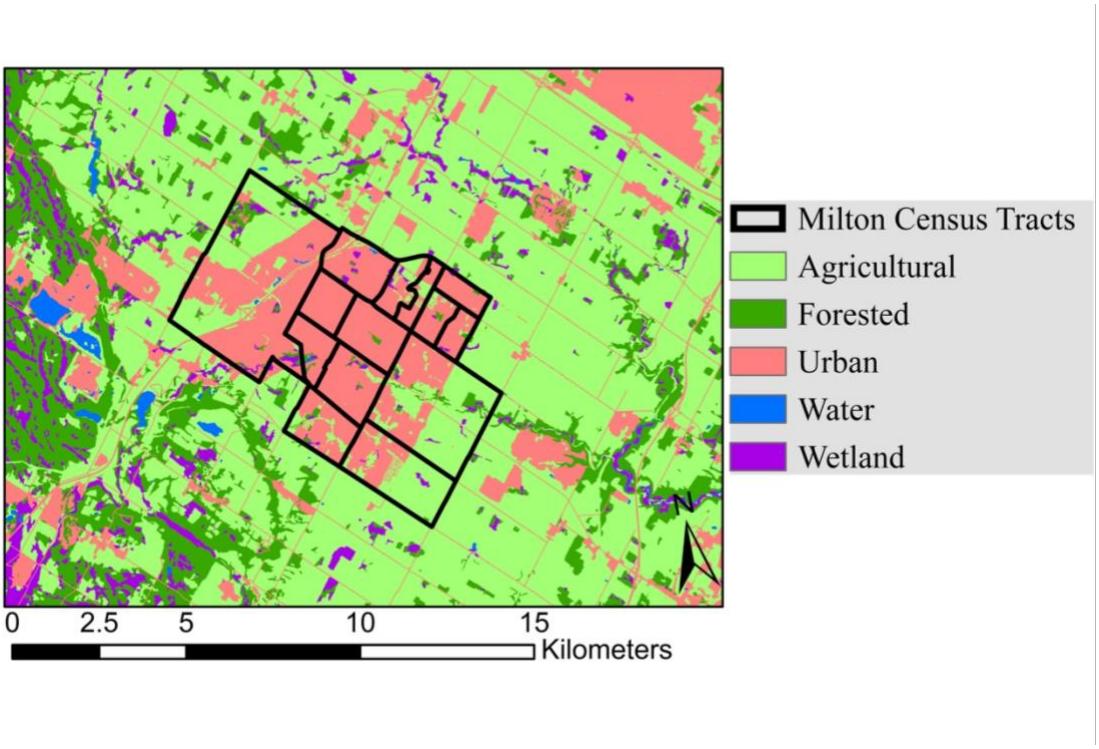

Figure H.4 : The distribution of land covers surrounding Urban Milton in the 2011 land cover product.

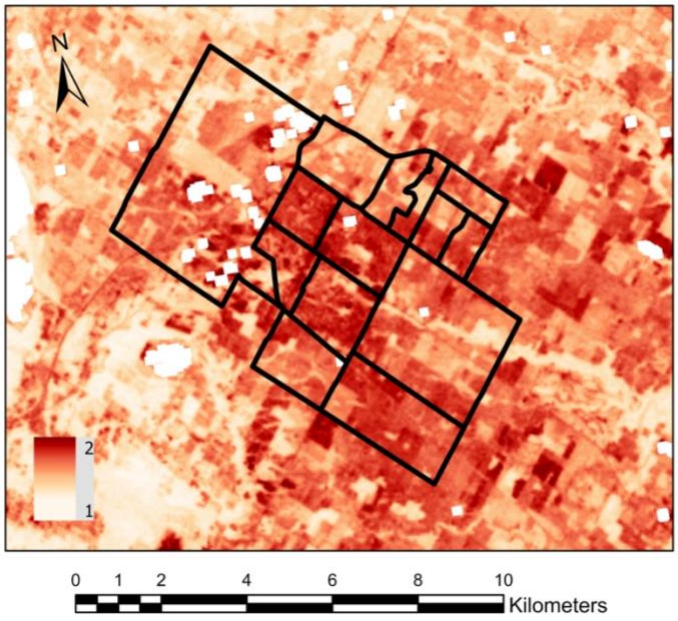

Figure H.5 : The LST in the Milton area on July 6, 2001 after dividing by the 16:00 Hamilton A air temperature measurement for normalization.

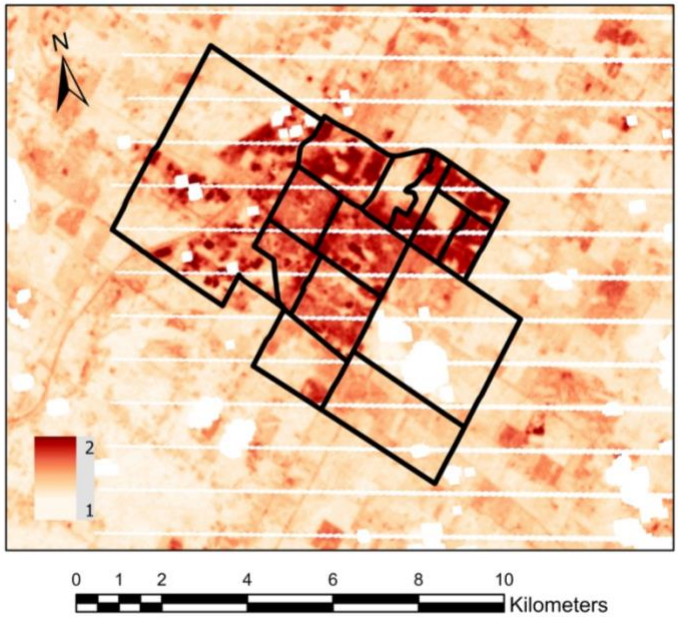

Figure H.6 : The LST in the Milton area on August 5, 2006 after dividing by the 16:00 Hamilton A air temperature measurement for normalization

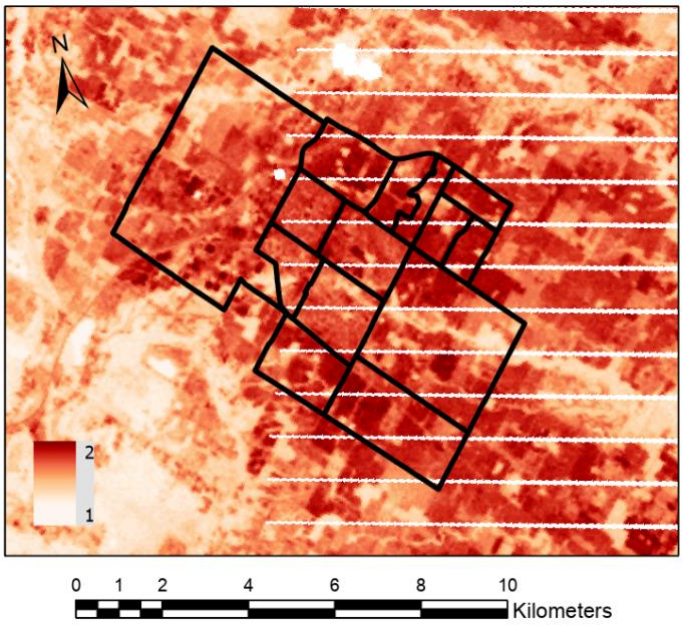

Figure H.7 : The LST in the Milton area on July 18, 2011 after dividing by the 16:00 Hamilton A air temperature measurement for normalization.

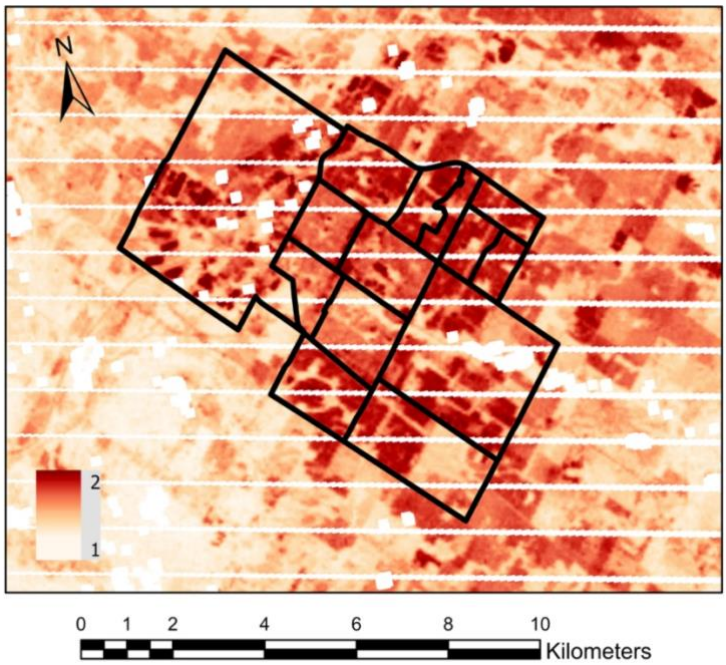

Figure H.8 : The LST in the Milton area on July 8, 2019 after dividing by the 16:00 Hamilton A air temperature measurement for normalization.